

Universidade de São Paulo
Instituto de Astronomia, Geofísica e Ciências Atmosféricas
Departamento de Astronomia

Amanda Caveagna Rubio

**Eyes on Phact:
unraveling a Be star and its disk**

São Paulo

2019

Amanda Caveagna Rubio

**Eyes on Phact:
unraveling a Be star and its disk**

Dissertação apresentada ao Departamento de
Astronomia do Instituto de Astronomia, Geofísica
e Ciências Atmosféricas da Universidade de
São Paulo como requisito parcial para a ob-
tenção do título de Mestre em Ciências.

Área de Concentração: Astronomia

Orientador(a): Prof. Dr. Alex Cavaliéri Car-
ciofi

Versão Corrigida. O original encontra-se disponível na Unidade.

São Paulo

2019

To Mum and Dad, and Miguel and Dimitri

Acknowledgements

À minha família, que sempre me apoiou em tudo;

Aos meus amigos, especialmente meus colegas de sala Fernanda e André, pela ajuda e pelas risadas;

Ao Ge, por ser o melhor amigo do mundo e me forçar a fazer exercícios e me lembrar de almoçar;

Ao meu orientador Alex e colegas do grupo Beacon, especialmente Bruno e Rodrigo, por toda a ajuda durante minha IC e mestrado, e por serem pessoas maravilhosas e pesquisadores incríveis;

A todos os meus quatro bichos de estimação, que eu vi muito pouco nos últimos meses: Monet, Otto, Juni e Lilibet;

À FAPESP, pelo apoio financeiro, sob os projetos n^o: 2017/08001-7 e 2018/13285-7;

À CAPES e CNPq, ao IAG, ao Prof. Leister pelos dados fornecidos;

To my advisor on Canada, Carol, and to all the friends I made during my 5 months living there, specially Keegan, who taught me to ice skate, Isabelle, who made my work possible and got me a whole lot of coffee. Thank you all.

“You twenty-first century humans with your science, your beliefs and your poetry and... oh, yeah, you’re pretty great. You never stop searching for answers. Sometimes I don’t think you know what the questions are, but you never stop searching. Somewhere out there in that chaos of darkness and light, of science and protons, of gods and stars and death... somewhere there’s an answer. And sometimes I think that just asking the question is the answer. And sometimes I think I just... need a coffee.”

Capt. Jack Harkness (Torchwood - *Lost Souls*)

Resumo

Discos são comuns em sistemas astrofísicos. Eles estão presentes em objetos estelares jovens, variáveis cataclísmicas, e até em núcleos ativos de galáxias. Vários desses discos podem ser bem descritos pela formulação de discos α , que assume que o disco é regulado pela viscosidade do material, descrita por um parâmetro chamado simplesmente de α . Todos os discos nos sistemas citados são discos de acreção: a matéria do disco está espiralando em direção ao objeto central, seja ele uma estrela ou um objeto compacto como um buraco negro. Porém, existe um caso particular em que o disco é de *decreção*, formado de matéria expelida pelo objeto central: as estrelas Be.

Estrelas Be são estrelas de tipo espectral B de alta rotação que, pelo elusivo fenômeno Be, ejetam matéria para órbita formando um disco Kepleriano viscoso. O modelo teórico que melhor descreve esses objetos é uma modificação do disco α , o modelo do disco de decréscimo viscoso (VDD), onde a viscosidade é a principal força agindo no disco uma vez que a matéria entra em órbita. O VDD foi testado com sucesso por diversos estudos multi-técnicas de estrelas Be, e é atualmente considerado o paradigma para esses objetos. Com a robusta estrutura do VDD como fundamento, podemos atacar o problema de como determinar os parâmetros fundamentais dessas estrelas com novos métodos e utilizando técnicas modernas como a inferência Bayesiana-Monte Carlo com cadeias de Markov (MCMC).

Nesse trabalho, combinamos técnicas MCMC com a grade de modelos de transferência radiativa BeAtlas para inferir os parâmetros fundamentais da estrela Be α Columbae (Phact), para a qual determinamos parâmetros estelares, geométricos e de disco utilizando fotometria, polarimetria e espectroscopia no ultravioleta. Encontramos que α Col é uma estrela de $\sim 4.66 M_{\odot}$, bastante evoluída, com uma taxa de rotação linear de 0.74. O sistema é visto à uma inclinação de aproximadamente 40° . O disco é tênue e tem um

expoente de densidade de 2.5, menos íngreme do que o esperado teoricamente para uma estrela Be estável como α Col, um resultado que concorda com a tendência de $n < 3.5$ para estrelas Be encontrada em estudos recentes. O disco também é truncado em $20 R_{eq}$, indicando a presença de uma companheira binária próxima.

Abstract

Disks are a common feature in astrophysical systems. They are present in young stellar objects, cataclysmic variables, and even active galactic nuclei. Many of these disks can be well described by the α -disk formulation, that assumes the build up of the disk is regulated by the viscosity of the material, described by the a parameter called simply α . All disks in the systems cited are accretion disks: the matter on the disk is spiralling towards the central object, be it a star or a compact object such as a black hole. There is, however, a very particular case where the disk is actually decreting, built from matter expelled from the central object: Be stars.

Be stars are fast rotating B type stars that, through the elusive Be phenomenon, eject mass into orbit, forming a viscous Keplerian disk. The model that best describes these objects is an α -disk modification, the Viscous Decretion Disk model (VDD), where viscosity is the main force acting on the disk once matter enters orbit. The VDD has been successfully tested by several multi-technique studies of Be stars, and is now cemented as the paradigm for these objects. With the robust framework of the VDD as bedrock, we are now able to tackle the issue of determining the fundamental parameters of these stars in novel ways using modern techniques, such as Bayesian-Monte Carlo Markov chain inference.

In this work, we combine Bayesian-MCMC techniques with the state-of-the-art radiative transfer model grid BeAtlas to infer the fundamental parameters of the Be stars α Col, for which we were able to determine stellar, geometric and disk parameters using photometry, polarimetry and UV spectroscopy data. We find that α Col is a $\sim 4.66 M_{\odot}$ star, very evolved, with a linear rotation rate of 0.74. The system is seen at an inclination of approximately 40° . The disk is tenuous and has a density exponent of 2.5, less steep

than what is expected by VDD theory for a stable Be star such as α Col, a result that agrees with a trend of $n < 3.5$ for Be stars in recent studies. The disk is also truncated at $20 R_{eq}$, indicating the presence of a previous unseen, close binary companion.

List of Figures

1.1	Figure showing the equipotentials $\Phi_R = const$ for a binary system with mass ratio of $q = 0.25$ (lines). The L markers indicate the Lagrangian points, M_1 and M_2 the stars, and CM the centre of mass of the system. The thick 8 shaped line around the two stars represent their respective Roche lobes. Image from Benacquista and Downing (2013).	5
1.2	Protoplanetary disks resolved by the Atacama Large Millimeter/submillimeter Array (ALMA). Results of the Disk Substructures at High Angular Resolution Project (DSHARP).	7
1.3	Figure 11 of Vieira et al. (2017). Their caption reads: “Evolution of the disc parameters between different epochs. The arrow tails correspond to values derived from AKARI observations, while the arrow heads correspond to determinations from ALLWISE data. The arrows were superimposed on the probability distribution of the fitted parameters (see Figure 7), and their colors correspond to the effective temperature determined by Frémat et al. (2005)”	15
1.4	Figure 13 of Vieira et al. (2017). Their caption reads: “Typical regions for distinct disc dynamical states in the n vs $\log\rho_0$ diagram, according to VDD hydrodynamical simulations. The defined regions were superimposed on the combined EMCEE posterior distributions for our sample (see Figure 7)”. Most of the stars in their sample fall in the “dissipating” region.	15
1.5	Visual representation of a Be star with a newly formed disk and its corresponding light curve, for different inclination angles and for BVRI filters, as indicated. Figure by L. Rímulo	16
1.6	Angular momentum loss versus stellar mass diagram calculated by Rímulo et al. (2018) compared to Granada et al. (2013) predictions in blue for the SMC and in green for the Galaxy. The red star represents 28 CMa.	17

1.7	Effects of the secondary on the Be disk for a close binary system. Panel (a) shows the accumulation effect while panel (b) shows the two-armed structures and truncation. . .	19
1.8	Emission line profiles for different inclination angles of Be stars, as per Struve’s model (Rivinius et al. 2013, Fig. 1).	23
1.9	Figure 5.2 from Mota (2019). Top: UV disk effect function of a typical late-type Be star ($M = 4 M_{\odot}$) at different orientations. Left: $i = 30^{\circ}$. Right: $i = 90^{\circ}$. Bottom: the same, but for a Be star of $9 M_{\odot}$	25
1.10	Figure showing the contribution of different Be star components to the flux as we increase the effective radius of the pseudo-photosphere. Figure from Vieira et al. (2015)	26
2.1	OPD polarization data for U, B, V, R and I filters, by date of observation. The orange region indicates $\pm 1\sigma$ from the mean value of the data for each filter.	33
2.2	Top: dynamic $H\alpha$ spectra from ESPaDOnS, BeSS, the MUSICOS and ECASS OPD spectrographs, FEROS, UVES, and the BeSOS database. Bottom: average line profile. . .	34
2.3	Flowchart of HDUST’s sampling process, for an envelope of many cells.	37
3.1	X_c relation with stellar age t/t_{MS} , for many spectral types.	43
3.2	The difference of using KDE or histogram for the same data. The line represents the KDE calculated a Gaussian kernel for the histogram of the mass of the star.	47
3.3	Effects on the flux caused by changing the stellar parameters while maintaining the same disk, from the UV to $1 \mu m$	50
3.4	Effects on the flux caused by changing the disk parameters while maintaining the same central star, from the near-infrared ($0.7 \mu m$) to $6.3 \mu m$	51
3.5	Example of a corner plot. Image from www.corner.readthedocs.io/en/latest/pages/quickstart.html	52
4.1	Corner plot for the UV region of the SED, with 300 walkers and 20000 steps, $af = 0.24$. . .	54
4.2	Corner plot for the UV+VIS region of the SED, with 300 walkers and 20000 steps, $af = 0.26$. . .	55
4.3	Corner plot for the UV+VIS+NIR region of the SED, with 300 walkers and 20000 steps, $af = 0.26$	56
4.4	Corner plot for the UV+VIS+NIR+MIR region of the SED, with 300 walkers and 20000 steps, $af = 0.21$	57

4.5	Corner plot for the UV+VIS+NIR+MIR+FIR region of the SED, with 300 walkers and 20000 steps, $af = 0.22$	58
4.6	Corner plot for the VIS+NIR+MIR+FIR+MICROW+RADIO region of the SED, with 300 walkers and 20000 steps, $af = 0.22$	59
4.7	Corner plot for the NIR+MIR+FIR+MICROW+RADIO region of the SED, with 300 walkers and 20000 steps, $af = 0.22$	60
4.8	Corner plot for the MIR+FIR+MICROW+RADIO region of the SED, with 300 walkers and 20000 steps, $af = 0.22$	61
4.9	Corner plot for the FIR+MICROW+RADIO region of the SED, with 300 walkers and 20000 steps, $af = 0.22$	62
4.10	Corner plot for the entire SED, with 300 walkers and 20000 steps, $af = 0.22$	63
4.11	Behaviour of the models when we vary mass and inclination in the UV region. In black is our IUE spectra, binned, for reference.	65
4.12	Boxplot for the PDFs derived in each SED cut BEMCEE run for the mass of the star.	67
4.13	Boxplot for the PDFs derived in each SED cut BEMCEE run for the oblateness of the star.	67
4.14	Boxplot for the PDFs derived in each SED cut BEMCEE run for the fraction of Hydrogen in the stellar core.	68
4.15	Boxplot for the PDFs derived in each SED cut BEMCEE run for the log of the base density of the disk.	68
4.16	Boxplot for the PDFs derived in each SED cut BEMCEE run for the radius of the disk.	69
4.17	Boxplot for the PDFs derived in each SED cut BEMCEE run for the radial density exponent of the disk.	69
4.18	Boxplot for the PDFs derived in each SED cut BEMCEE run for the inclination of the system.	70
4.19	Boxplot for the PDFs derived in each SED cut BEMCEE run for the distance of the star.	70
4.20	Boxplot for the PDFs derived in each SED cut BEMCEE run for the extinction.	71
4.21	Corner plot for the polarization (U, B, V, R, and I), with 600 walkers and 2000 steps, $af = 0.32$. This run only included the priors on distance and $v \sin(i)$	72
4.22	Corner plot for the polarization (U, B, V, R, and I), with 600 walkers and 2000 steps, $af = 0.37$. This run included the KDE priors on the mass, W and age of the star as determined in the run shown in Fig. 4.10.	74

4.23	Combined corner plot for the full SED result (Fig. 4.10) in purple and the polarimetry result (Fig. 4.22) in green, with the combined PDFs in black.	75
4.24	Chord diagram for the correlations seen in Fig. 4.10	77
4.25	Chord diagram for the correlations seen in Fig. 4.22	78
4.26	Top: Best fit SED (model of Fig. 4.10). Bottom: squared residue plot.	81
4.27	Same as Fig. 4.26, now limiting the minimum error for a SED point at 1%	82
4.28	Comparison of 3 BeAtlas models with the same parameters except for the truncation radius R_D , plotted with the photometric data of α Col.	83
4.29	Collected H α spectra for the Be star α Col. Our goal was to look for detectable periods in the radial velocity shifts of the line, and on violet/red peaks intensity. The upper left panel is our spectra corrected for the RV shift. The middle left panel is the Lomb Scargle intensity plot; the best period is not, however, significant enough to be actually considered a detection. The bottom left panel is the data folded in phase with the “best” period found on the Lomb Scargle plot. The panels on the right are the same, but for the V/R variation. Again, no clear period was detected. The results are therefore inconclusive, likely due to the inhomogeneity of the data.	84
5.1	Histogram of the values of n from Vieira et al. (2017) (in purple) and Klement et al. (2019) (in orange)	91
5.2	Comparing the mean values of n derived by the surveys of Vieira et al. (2017) and Klement et al. (2019).	92
5.3	Comparison of the values of n and $\log \rho_0$ found by Vieira et al. (2017) for all 14 stars in our sample.	92
A.1	Measurements for the equivalent width (EW - panel 1), emission over continuum (EC - panel 2), separation between the two emission peaks (PS - panel 3), and violet on red emission (V/R) for our collection of H α spectra summarised in Table 2.3.	117
A.2	Effects on the flux caused by changing the rotation rate parameter while maintaining the same central star and disk, on the mid-infrared 5 to 40 μm	118
A.3	1st panel: the 27 days TESS lightcurve for α Col. 2nd and 3rd panels: the first half and second half of the data. A zoom-in from the 1st panel. Courtesy of J. Labadie-Bartz.	119
B.1	Trace plot for the BEMCEE result in Fig. 4.1, the red line represents the burn-in phase.	122

B.2	Trace plot for the BEMCEE result in Fig. 4.2, the red line represents the burn-in phase. .	123
B.3	Trace plot for the BEMCEE result in Fig. 4.3, the red line represents the burn-in phase. .	124
B.4	Trace plot for the BEMCEE result in Fig. 4.4, the red line represents the burn-in phase. .	125
B.5	Trace plot for the BEMCEE result in Fig. 4.5, the red line represents the burn-in phase. .	126
B.6	Trace plot for the BEMCEE result in Fig. 4.7, the red line represents the burn-in phase. .	127
B.7	Trace plot for the BEMCEE result in Fig. 4.8, the red line represents the burn-in phase. .	128
B.8	Trace plot for the BEMCEE result in Fig. 4.9, the red line represents the burn-in phase. .	129
B.9	Trace plot for the BEMCEE result in Fig. 4.10, the red line represents the burn-in phase.	130
B.10	Chord diagram for the correlations seen in Fig. 4.2	131
B.11	Chord diagram for the correlations seen in Fig. 4.3	132
B.12	Chord diagram for the correlations seen in Fig. 4.4	133
B.13	Chord diagram for the correlations seen in Fig. 4.5	134
B.14	Chord diagram for the correlations seen in Fig. 4.6	135
B.15	Chord diagram for the correlations seen in Fig. 4.7	136
B.16	Chord diagram for the correlations seen in Fig. 4.8	137
B.17	Chord diagram for the correlations seen in Fig. 4.9	138

List of Tables

2.1	Spectral types in literature for α Col, from the Catalogue of Stellar Spectral Classifications (Skiff, 2014)	30
2.2	SED fluxes from $0.3 \mu\text{m}$ to 6.3 cm . References are given in the text.	31
2.3	H α spectra of α Col collected from various sources and online databases. In total, we had access to 112 spectra.	32
3.1	Parameters used to create the grid. The fraction of H in the core of the star X_c corresponds to the time of life of the star in the Main Sequence, t/t_{MS} . Parameter n_0 is the actual input value required by HDUST, but its more physically interesting counterpart ρ_0 is the one used to discuss the results.	44
3.2	Band definitions for the grid.	44
3.3	“Cut” regions defined in our analysis.	51
4.1	Parameter results from BEMCEE for the complete SED of α Col.	66
4.2	Parameter results from BEMCEE for the combination of the results for the SED and polarimetry of α Col. Distance and extinction are the same as the SED result, as these parameters are not included in the polarimetry run.	76
5.1	Parameter results from BEMCEE for the combination of the results for the SED and polarimetry of α Col. Distance and extinction are the same as the SED result, as these parameters are not included in the polarimetry run.	88
5.2	Crossmatch of stable Be star radial density exponent derived by Vieira et al. (2017) and Klement et al. (2019). The bold stars are α Col, β CMi and α Ara.	90
A.1	Literature determinations of the stellar parameters of the Be star α Col.	116

Contents

1. <i>Introduction</i>	1
1.1 Disks in Astrophysical Systems	1
1.2 α -Disks	3
1.3 Applications	4
1.4 Classical Be Stars	8
1.4.1 Viscous Decretion Disk	9
1.4.1.1 Steady State Isothermal VDD	11
1.4.1.2 Variations	13
1.4.2 Central Star	20
1.4.3 Observational Characteristics	22
1.4.3.1 Spectral Lines	23
1.4.3.2 Continuum Emission	24
1.4.3.3 Linear Polarization	26
1.5 Objective of this dissertation	26
2. <i>Data and Tools</i>	29
2.1 α Columbae	29
2.1.1 Ultraviolet spectra	30
2.1.2 Visible - Radio observations	31
2.1.3 Polarimetry	32
2.1.4 $H\alpha$ spectroscopy	32
2.2 HDUST	36
2.3 Bayesian Statistics and Monte Carlo Markov Chain Methods	38

3. <i>Methodology</i>	41
3.1 BeAtlas Grid	41
3.2 BEMCEE Package	43
3.2.1 Posterior sampling	45
3.2.2 Structure	48
4. <i>Results</i>	53
4.1 SED	53
4.2 Polarimetry	71
4.3 Correlations	76
4.4 Uncertainties and BEMCEE	80
4.5 Disk Truncation and Binarity	81
5. <i>Analysis and Discussion</i>	87
6. <i>Conclusions and Future Perspectives</i>	95
<i>Bibliography</i>	99
 <i>Appendix</i>	113
A. <i>Additional Data and Plots</i>	115
B. <i>Trace Plots and Chord Diagrams</i>	121

Introduction

1.1 Disks in Astrophysical Systems

We owe our existence to an astrophysical disk. Billions of years ago, there was no Sun and no solar system, just a thick molecular cloud, like many others in the arms of the Galaxy. This initial molecular cloud then gravitationally collapsed: its dense core became the young Sun, while the rest of the material organized itself in a circumstellar disk around it due to the conservation of angular momentum, that prevents material from falling directly onto the central star. From this so called protoplanetary disk, the planets and other bodies of the solar system were formed. Our Galaxy itself has a disk: an enormous mass of gas, dust, and stars rotating around the unwieldy bulge of the Milky Way. Sagittarius A*, the supermassive black hole at the centre of our galaxy also has a disk, as matter falls into its gravitational pull and forms what is known as an accretion disk. Compact objects in binary systems with regular stars can also have accretion disks, as the star evolves and fills the Roche lobe or as it loses mass through stellar winds and this discarded material is accreted by its dense companion. Disk structures are, therefore, very common in the universe.

Disk theory was developed in the 1960's, mostly in the context of black hole accretion disks (e.g. Shklovsky 1967 and Pringle and Rees 1972 for stellar BH and Lynden-Bell 1969 for galactic BH). The classic review of Pringle (1981) provides a more general overview on the subject of accretion disks, but still focusing mostly on BH. Here we attempt to review the subject in the broader sense of astrophysical disks in general.

To form the disk, a source of matter is required. In protoplanetary disks, matter enters the system from the molecular cloud surrounding it, while in accretion disks it is given by

the secondary. In active galactic nuclei (AGN), all sorts of astrophysical objects can fall into the black hole's gravitational well and become food for the accretion disk. Regardless of how material was deposited in the disk, as it circles around the orbit with an azimuthal velocity v_ϕ and radial velocity v_r , it is spread out into a ring of matter by the combined action of the gravity of the central object and the centrifugal force. The matter is a gas: a fluid, not a solid, so its rotation is differential. Having layers of the gas with different velocities leads to shear strain, a force that disrupts and deforms the fluid. How affected the gas is by this force depends on the viscosity of the fluid, as it allows for the dissipation of the energy of the shearing motion. This motion leads to transfer of mass and angular momentum (AM) between fluid layers.

The exchange of mass and AM is what causes the disk to grow. As viscosity dampens the shear force, the inner layer will lose energy, and AM will be transferred to the neighbouring layer. Since it now has lost energy, the inner layer must fall to a lower orbit. In this manner, mass is transported inwards while AM goes outwards. As this continues to happen over an extended time, matter extends to very low orbits, with decreasing AM, and to larger orbits, with high AM. We then end up with a disk that has a surface density Σ , variable with radius and time. Given this formation mechanism, the velocity field of the disk is usually approximated well by a Keplerian law, meaning that the closer to the centre of mass the material is, the faster it rotates.

While the disk obviously has a non-zero net motion in the azimuthal and radial directions, it can usually be considered to be in hydrostatic equilibrium in the vertical direction. Considering the simple case where the disk is isothermal at a radius R , the vertical scale of the disk is dominated by gas pressure $p = \rho \frac{kT}{m_H \mu}$ (where T is the disk temperature, k is the Boltzmann constant, m_H is the proton mass, and μ the mean molecular weight) and by the gravitational component from the central object. As we go to larger and larger radii, the disk will flare as this component diminishes. Even so, disks in general do not have a large opening angle and are quite thin, so another common approximation to use is that $z \ll r$. We find the volume density equation for the disk to be

$$\rho(r, z) = \rho_0(r) \exp\left(\frac{-z^2}{2H^2}\right), \quad (1.1)$$

where the scale height $H = \frac{c_s R_\star}{v_{orb}}$, since the sound speed in the disk is given by $c_s = \sqrt{\frac{kT}{m_H \mu}}$, and $v_{orb} = \sqrt{\frac{GM}{r}}$, and ρ_0 expresses the radial density.

1.2 α -Disks

Effectively, what drives a disk is viscosity, by controlling the transport of mass and AM. Viscosity can arise from various types of matter interaction. In gases, the chaotic motion and collision of the molecules is the one source of viscosity, and is very dependent on the temperature, as higher temperatures lead to more chaotic motions. Can this molecular viscosity be driving force of accretion disks? The kinematic viscosity coefficient in this case is $\nu \sim a_T \lambda$, where $a_T = (kT/m)^{1/2}$ is the thermal velocity on the gas, and λ is the mean free path length. The time scale of the viscous accretion (t_{acc}) depends on ν and the radius of the disk. Using typical values for a BH accretion disk ($R \sim 10^{10}$ cm, $T \sim 10^4$ K and $n \sim 10^{16} \text{cm}^{-3}$), the kinematic viscosity is of the order of $10^3 \text{cm}^2 \text{s}^{-1}$. The time scale for a disk with a radius of 10^{10} cm is $t_{acc} \sim 10^9$ yr. The velocity of the flow would then be much too slow: that is of the order of the age we believe the Universe to be. How could planetary systems form if the timescale of the disk formation is so long? Thus, simple molecular viscosity is not enough to explain the known timescales of the disk.

Another type of viscosity is turbulent or eddy viscosity. The addition of turbulent viscosity would make the combined kinematic viscosity large enough that it can explain a viscous accretion disk as we observe in astrophysics. The fact that this viscosity exists in disks has been confirmed, but its origin is still uncertain.

There are two main possibilities: it can arise from fluid instability or from magnetic instability (Montesinos 2012 for a review). If the disk is mostly subject to simple molecular viscosity, the ratio of the gas motions to the kinematic viscosity (referred to as the Reynolds number) $\Re \propto 1/\nu$ is large, as ν is a small number. Interestingly, large Reynolds numbers lead to instability in the fluid: their previously laminar structure becomes disrupted by eddies, which in turn leads to turbulent viscosity (Lynden-Bell and Pringle 1974, see also de Freitas Pacheco and Steiner 1976). There is, however, controversy on whether or not this instability would be enough to create significant turbulent viscosity to drive a disk.

The most favoured theory is that a turbulent viscosity arises from magneto-rotational instability (MRI). Balbus and Hawley (1991) show in their work that, as long as the disk has a radial angular velocity gradient that decreases with radius, any small seed magnetic field is capable of creating instability. The field tries to keep the material together, fighting against the differential rotation and the outwards motion of the fluid as it gains AM. So

the fluid is forced to rotate faster than it should given its new radial position, which causes it to spread out even further. This tug-o-war mechanism leads to instability, and finally to turbulent viscosity.

In 1973, Shakura & Sunyaev proposed a viscous disk model that can be parametrized in such a way that the specific origin of the viscosity is not necessary to describe the physics of the disk, just that it exists. The kinematic coefficient for turbulent viscosity can be expressed as $\nu_t = v_t L$, where v_t is the turbulent viscosity and L is the size of the largest eddies. In a thin disk, the size of the eddies cannot exceed the thickness of the disk, so $L \leq H$. The velocity of the turbulence does not exceed the sound speed, so $v_t \leq c_s$. Therefore, the kinematic viscosity has to be proportional to $H \cdot c_s$. Shakura and Sunyaev (1973) characterize ν in terms of a dimensionless parameter α

$$\nu = \alpha H c_s, \quad (1.2)$$

where $\alpha \leq 1$.

Such disks are known as α disks, and are widely used in the literature to describe many astrophysical systems.

1.3 Applications

The α -disk model was first created with accreting black holes in mind, the formulation is also used to describe, for example, accretion in binary systems in general. These systems are quite common: about 70% of massive stars are, at some point of their lives, in a mass exchange binary system (Sana et al., 2012).

As the two components of an close binary system evolve, mass loss from one of the stars (called the donor) can lead to the formation of a disk around the gainer star, usually a compact object such as a white dwarf, neutron star or black hole. There are two main possibilities for the mass transfer stage: the donor can grow in size to the point where the separation between the two stars becomes small enough so the gainer's gravitational pull rips off its outer layers (Roche lobe overflow); or the donor can reach a stage of extreme mass loss through stellar winds, that are captured by the gainer's gravitational well.

We can draw a map of the Roche potential (Φ_R), that accounts for the gravitational effects of the stars acting on one another and the centrifugal force: close to the stars, the gas is subject to its gravitational pull, but as it moves out the centrifugal and tidal forces

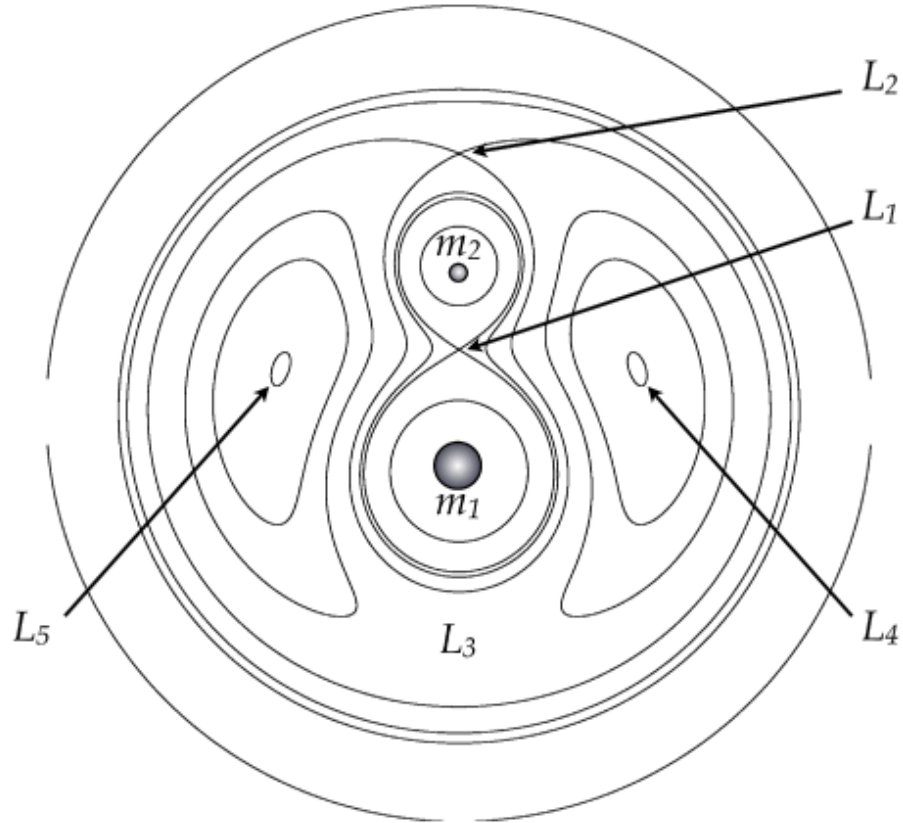


Figure 1.1: Figure showing the equipotentials $\Phi_R = const$ for a binary system with mass ratio of $q = 0.25$ (lines). The L markers indicate the Lagrangian points, M_1 and M_2 the stars, and CM the centre of mass of the system. The thick 8 shaped line around the two stars represent their respective Roche lobes. Image from Benacquista and Downing (2013).

begin to interfere and change the shape of the potential, as shown in Fig. 1.1. The lines in the figure represent the gravitational equipotentials $\Phi_R = const$. The thick lines in an 8 shape around the two stars represent their Roche lobes, which connects the potential valleys of the stars. In simple terms, if one of the stars (now called the primary) grows to fill their Roche lobe during its evolution, the additional matter will funnel through the Lagrangian point L_1 onto the secondary, forming, finally, an accretion disk. The resulting disk can be described by the α -disk formulation.

When the companion is a white dwarf, the mass transfer binary system can fall into the cataclysmic variable (CV) category. In this scenario, the white dwarf companion accretes mass from the primary (usually a red dwarf star) via Roche lobe overflow. White dwarfs (WD) can have significant magnetic fields: if strong enough, the matter will be forced to follow the field lines and accrete on the poles. Otherwise, a disk as previously discussed will be formed.

The CV class encompasses classical and dwarf Novae events. White dwarfs are evolved stars, and therefore have very little hydrogen, being composed mostly of helium or carbon and oxygen depending on the mass of the progenitor. The companion, however, is a relatively unevolved star, and so most of the material accreted by the WD is hydrogen, that forms a layer on the surface of the white dwarf. As the density of the H layers grows, the material becomes degenerate. At the inner part of the layer, temperature becomes high enough to allow H burning. The combination of these two factors lead to an explosion in the surface of the star, the event known as classical Nova.

Dwarf nova have a different powering mechanism that is closely connected to the disk. In temperatures of $\sim 10^4 K$, the hydrogen on the disk is only partially ionized, which leads to an accretion rate that can change drastically with small variations in temperature. As such, the system goes through phases where the accretion rate is very small, leading to matter accumulation in the disk, and suddenly, as the temperature increases, dumps this accumulated mass into the WD. This cycle repeats continuously over the lifetime of the system, another characteristic that sets it apart from classical nova. For more information on cataclysmic variables as a class, see recent reviews such as Cannon Smith (2007).

α -disk formulation is by no means restricted to binary systems. Disks can also be present when there is no companion in sight. The disks of young stellar objects (YSO) are of obvious interest, as they are the early stage of protoplanetary disks that evolve into planetary systems (see Fig. 1.2¹ for resolved images of YSO disks). The solar system was born from such a disk, when the Sun was still a young star. As a molecular cloud gravitationally collapses to form a protostar, the rest of the material organizes itself around it in a disk shape due to the conservation of AM. Accretion of this disk material into the protostar allows it to build up mass and ignite hydrogen, so it becomes a star. This process takes up only a minor fraction of the disk lifetime. Protoplanetary disks have a distinction from the disks described so far in that dust is also present, not just gas. Although they take up less than 1% of the total disk mass, the dust grains are actually the building blocks of planets. While the gas motion is controlled by the viscosity, these solid particles collide and merge, gaining mass and settling in the centre of the disk, decoupled from the gas. Protected from the stellar radiation by the disk, these grains grow into rocks and eventually into planets, forming planetary systems like ours. See recent review Williams

¹ Image from www.almaobservatory.org/en/press-release/\alma-campaign-provides-unprecedented-views-of-t.

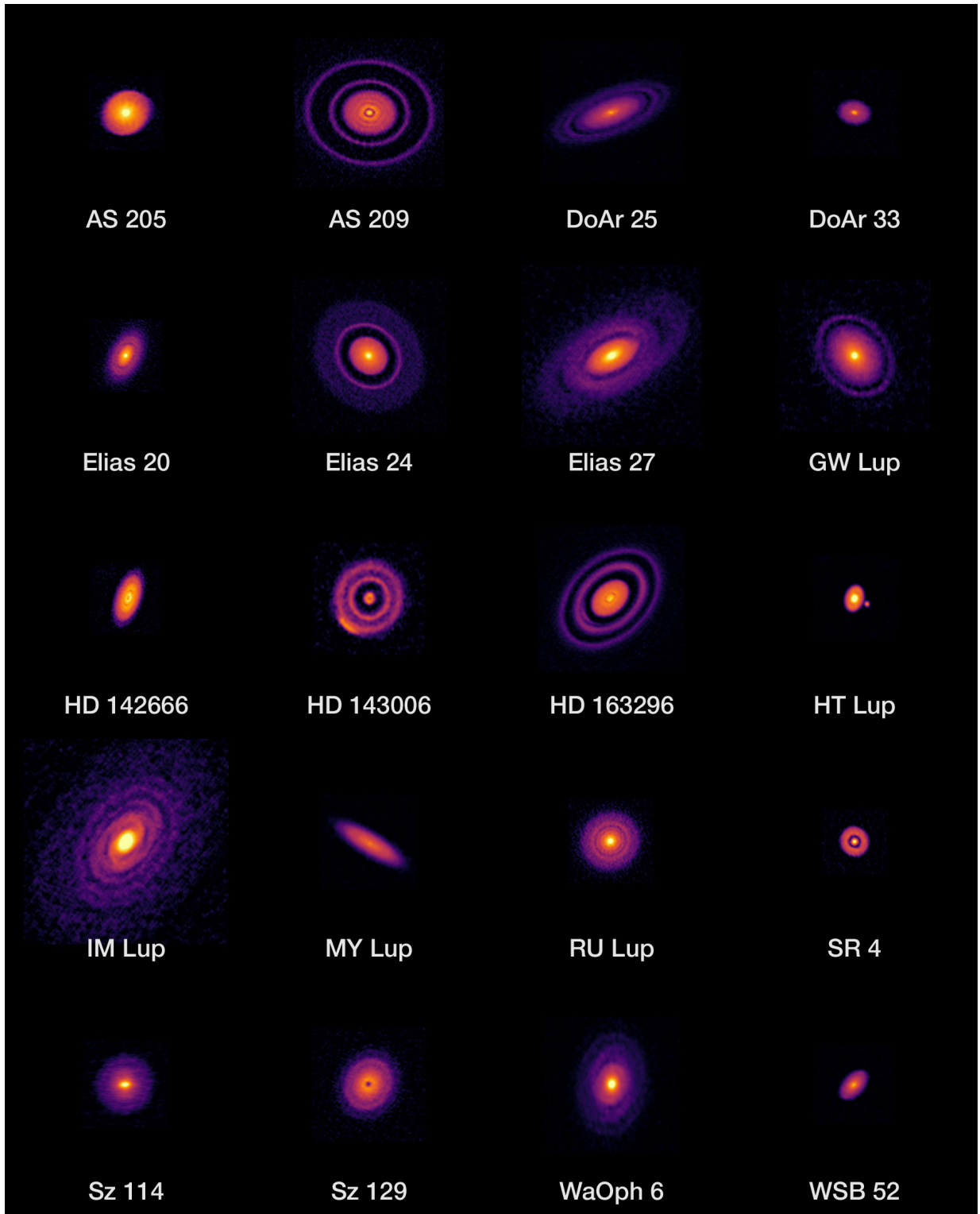


Figure 1.2: Protoplanetary disks resolved by the Atacama Large Millimeter/submillimeter Array (ALMA). Results of the Disk Substructures at High Angular Resolution Project (DSHARP).

and Cieza (2011) for more details.

All these types of disks follow the α prescription in simple terms, but of course they all have different factors to consider. Effects such as the magnetic field of the secondary and presence of dust in the disk affect the accretion. The disks around BHs, be they stellar mass or the supermassive ones in the centre of galaxies, are subject to relativistic effects once matter gets close to the event horizon. The disk may not be thin as we assumed in the previous section, leading to thick disk theory. It may also be unsteady, varying greatly with time, or subject to a viscosity that changes with the radius and time. The origin of the viscosity, which we downplayed by adopting the α formulation, can also lead to big changes in the disk physics.

However, it remains true that all the disks mentioned are accretion disks, where the final destination of the material is the accreting object. But there is the particular case where the disk is not accreting, but rather *decreting*, as in leaving a central object. These are the curious decretion disks of Be stars.

1.4 Classical Be Stars

Be stars are a subclass of B spectral type stars, and as such share all their main characteristics. They range from about 10000 to 30000 K in effective temperature, and have masses from 2.9 to 18 M_{\odot} (Cox, 2000). The spectrum of B stars is dominated by strong He I and Balmer hydrogen absorption lines (specially $H\alpha$ and $H\beta$), Si I and Si II, O I and Mg I. Stars classified as Be also show these features, but with the distinction that some of their lines, notably their Balmer hydrogen lines, are in emission rather than absorption. Be stars also show linear polarization and excess flux in the IR, and are known for their significant variability in time-scales from days to decades.

The first discovered Be star was γ Cas in 1866 by Italian priest and astronomer Angelo Secchi. He reported in his logs that the spectrum of the star showed a very strong line in emission, something he found odd, as stellar spectra usually show them in absorption. The line in question was later discovered to be $H\beta$. As more H lines in emission were detected in B stars it became interesting to round up this objects so they could be studied as a class. γ Cas and similar stars were then assigned the denomination of B emission, or Be, stars.

At this point, the definition of Be star was simply that their spectra was that of a B type star, but the H lines were in emission. Struve (1931) refined it by excluding stars with P Cygni profiles from the Be class, as he attributes them to different formation mechanisms. Struve noticed that Be stars are fast rotators, so much so that the star would be oblate and could become rotationally unstable. It would then shed excess angular momentum through the equator, forming what he called a ring-shaped “nebula” around the star, that would lead to the formation of recombination lines. Struve’s model, in its essence, is nowadays firmly set as the correct description of these objects, as confirmed by interferometric observation of Be stars (Quirrenbach et al. 1994, Quirrenbach et al. 1997).

The present-day definition of the Be class was finally given by Jaschek et al. (1981)

“A non-supergiant B star whose spectrum has, or had at some time, one or more Balmer lines in emission.”

This is still quite a broad definition, as it encompasses any B star with circumstellar material significantly dense, such as Herbig and B[e] stars, even though the physical process responsible for the presence of the material is different. It is therefore useful to also define the class from a theoretical perspective: classical Be stars are very fast rotating B type stars that consistently possess a Keplerian gaseous viscous decretion disk, whose presence lead to linear polarization, IR excess, and Balmer lines in emission. This theoretical definition has only recently been put forth by Rivinius et al. (2013). We expand on these objects and their traits and attributes in the following sections.

1.4.1 Viscous Decretion Disk

The origin and shape of Be circumstellar material were greatly debated in the 80’s and 90’s. The optical long baseline observations of Quirrenbach in 1994 dug the grave for models with a spherical geometry, but the remaining disk and oblate envelope models were still in play. Quirrenbach et al. (1997)’s interferometric observations of Be star ζ Tau indicated an upper limit for the disk opening angle of $\sim 20^\circ$, while spectropolarimetry data (Wood et al., 1997) implied either a very thick envelope with an opening angle of 52° , or a very thin one with 2.5° . Combining the two pieces of information, the disk must thin. Via FeII lines, Hanuschik (1996) also came to the conclusion that the envelope of Be stars had to be thin and axissymmetric, and likely rotationally supported. Therefore, the thin

disk structure of the circumstellar material of the Be stars is confirmed.

There were many disk models proposed in the 90's to explain the physics of the formation and build up of the decretion disk, and were gradually refuted by observations. The wind compressed disk (WCD) model (Bjorkman and Cassinelli, 1993) was the first dynamical model for Be disks, describing the disk formation and growth. In their theory, the polar winds from the central star would follow streamlines and coalesce at the equator, and their ram pressure would confine the material and condense it into a thin disk. It was successful in explaining lines in emission and polarization, but found difficulty regarding the IR excess and violet on red (V/R) variations in double peaked spectral lines (Porter, 1997). Be star line profiles can be double peaked due to the Doppler effect of the motion of the disk. V/R variations are often cyclic and have long periods, of the order of years, which appear to depend only on the disk, not the central star, as difference in spectral type was not shown to affect the cycles. Okazaki (1991) suggested that the variations came from global disk oscillations. That lead to the formation of a one-armed density wave that travels through the disk. As it spirals around, the receding and approaching sides of the disk have a periodic increase in density, leading to the observed V/R variations. A spiral wave such as this can only be stable if the radial motions on the disk are small, otherwise they would hinder the oscillation modes and the wave would not form. The disk has therefore to rotate in a Keplerian fashion.

Around the same time, another disk model was proposed that in the following decades proved to satisfactorily explain the linear polarization, IR excess and emission line formation, while also effectively distributing angular momentum and arriving at a Keplerian velocity law: the Viscous Decretion Disk (VDD) model.

First proposed by Lee et al. (1991), the VDD is the disk model that best describes the observational characteristics of Be stars, having yet to be discredited by any observations. It was further developed by Bjorkman (1997), Okazaki (2001), Bjorkman and Carciofi (2005), among others, and is currently the model adopted by nearly all studies involving Be stars. At its core, the VDD is an α -disk modification. It is very similar to the disks of YSOs, but, as a decretion disk, works backwards, building from inside out. The material is ejected from the central star through a still unknown mechanism, which several studies believe to be connected with non-radial pulsations observed in a great number of Be stars (Rivinius et al. 2003, Baade et al. 2016 and following series of papers). The majority of

the mass ejected actually falls back into the central star (99% according to Okazaki et al. 2002), but the rest of the material and angular momentum are spread out into higher orbits due to the viscosity, thus building up the circumstellar disk. This theory and its subsequent confirmation via spectropolarimetric observations was the demise of the WCD model, since radially driven winds exert no torque and cannot transfer angular momentum outwards to reach a Keplerian velocity law.

1.4.1.1 Steady State Isothermal VDD

Since the VDD follows the α prescription, we know that the kinematic viscosity is given by Eq. 1.2. The main characteristics described in the previous sections remain: the disk is axisymmetric and in vertical hydrostatic equilibrium ($v_z = 0$), it is considered thin, and Keplerian in rotation, and the outflow from the central star that implies a $v_r \neq 0$. Following Bjorkman and Carciofi (2005) we can find the fluid equations for the case of a viscous decretion disk. The continuity equation in the case of a viscous disk is

$$\frac{1}{r} \frac{\partial(r\rho v_r)}{\partial r} + \frac{1}{r} \frac{\partial(\rho v_\phi)}{\partial \phi} + \frac{\partial(\rho v_z)}{\partial z} = 0. \quad (1.3)$$

Therefore, assuming Keplerian rotation ($v_\phi \approx \sqrt{r}$) and no vertical motions ($v_z = 0$), the equation above takes the form

$$\frac{\partial(2\pi r \Sigma v_r)}{\partial r} = 0, \quad (1.4)$$

which gives us the rate of the matter flowing out of the central star as $\dot{M} = 2\pi r \Sigma v_r$.

The viscosity greatly affects the circular flow of the material, as it counters the shearing forces that arise from differential rotation. In a simple Keplerian disk with no viscosity, the momentum in the ϕ direction is written as

$$v_r \frac{\partial v_\phi}{\partial r} + \frac{v_\phi}{r} \frac{\partial v_\phi}{\partial \phi} + v_z \frac{\partial v_\phi}{\partial z} + \frac{v_r v_\phi}{r} = \frac{1}{\rho r} \frac{\partial P}{\partial \phi} + f_\phi, \quad (1.5)$$

where f_ϕ are the external forces acting on the system. The equation becomes more complicated when we include viscosity as it exerts a torque. The equation becomes, assuming $dv_\phi/d\phi$ and dv_ϕ/dz are zero and that the disk is thin,

$$v_r \frac{\partial v_\phi}{\partial r} + \frac{v_r v_\phi}{r} = \frac{1}{\rho r^2} \frac{\partial(r^2 \nu \rho A)}{\partial r}, \quad (1.6)$$

where the shear strain A and the kinematic viscosity ν relate as

$$\nu \rho A = (\alpha c_s H) \rho r \frac{\partial(v_\phi r)}{\partial r}. \quad (1.7)$$

Taking the momentum equation Eq. 1.6 and integrating once more in ϕ and z , we can find the torque \mathcal{T} for a viscous α decretion disk

$$\dot{M} \frac{\partial (rv_\phi)}{\partial r} = \frac{\partial \mathcal{T}}{\partial r}, \quad (1.8)$$

where the viscous torque is

$$\mathcal{T} = \int_{-\infty}^{\infty} \pi r^2 2\pi_r \phi dz = -3c_s^2 r^2 \alpha \Sigma. \quad (1.9)$$

Assuming \dot{M} is constant, we can integrate the above equation to find the analytical solution for the surface density

$$\Sigma(r) = \frac{\dot{M} v_{orb} R_\star^{1/2}}{3\pi \alpha c_s^2 r^{3/2}} \left[\left(\frac{R_0}{r} \right)^{1/2} - 1 \right], \quad (1.10)$$

where R_\star is the radius of the central star, v_{orb} is the Keplerian circular orbital velocity at the equator and R_0 is an integration constant.

To find the structure of the volume density of the disk, it is interesting to make an assumption on its temperature structure. If it is a simple power law as

$$T = T_0 \left(\frac{R}{r} \right)^s, \quad (1.11)$$

with T_0 a temperature scale, the scale height, which depends on the temperature via the sound speed c_s becomes

$$H = H_0 \left(\frac{r}{R} \right)^\beta, \quad (1.12)$$

where $H_0 = c_s(T_0)R/v_{orb}$. The scale height exponent β relates to the temperature exponent s as $\beta = (3 - s)/2$. We can plug this new scale height into the volume density equation Eq. 1.1, and obtain

$$\rho(r, z) = \rho_0 \left(\frac{R}{r} \right)^n \exp \left(\frac{-z^2}{2H^2} \right), \quad (1.13)$$

where $n = (7 - 3s)/2$ and ρ_0 is the density at the base of the disk. In the case of an isothermal disk ($s = 0$), $\beta = 1.5$ and $n = 3.5$. This steady-state power-law approximation is incredibly useful, as the complex structure of the disk can be approximated by such a simple equation and facilitate the efforts of modelling these objects.

Although Be stars are known for their variability (see Sec. 1.4.1.2), and a true steady-state can never be reached (Okazaki, 2007), if their disk is formed subject to a roughly constant mass injection rate, the density structure reaches a quasi-steady state (Haubois et al., 2012). Whether the density profile at this stage is a power-law or not is still

not firmly established (see, for instance, the study Carciofi and Bjorkman 2008 on non-isothermal viscous diffusion). As such, these stable Be stars proved to be the perfect stage to test the validity of the VDD model, even if in its simpler form.

Works such as Tycner et al. (2008), Jones et al. (2008), Carciofi et al. (2006), Carciofi et al. (2009) and Silaj et al. (2016) focus on the effort of creating realistic physical models for Be stars in the VDD framework using non-local thermodynamic equilibrium (non-LTE) radiative transfer codes such as BEDISK (Sigut and Jones, 2007) (for the first two works) and HDUST (Carciofi and Bjorkman, 2006) (for the latter 3 - more on this particular code in Sec. 2.2). They exploit the power-law approximation to directly compare the model with different types of data of particular Be stars. Klement et al. (2015) work with β CMi was particularly thorough, combining in their multi-technique analysis spectral energy distribution (SED), polarimetric, interferometric and spectroscopic data. These results all prove the success of the VDD in describing Be disks.

1.4.1.2 Variations

Be stars are, however, far from steady, and famous for it. Both the central star and the circumstellar disk are subject to changes that result in variability in many timescales. As per the VDD model, the disk depends on a constant input of angular momentum to exist and should this mechanism stop, the disk will dissipate, partially re-accreting onto the star and partially merging with the interstellar medium. Just as easily it stops, it can restart and form a new disk, then stop the mechanism again and dissipate it. When the Be star has a disk, it is said to be in their active phase. When it does not, it is inactive, and acts and presents itself as a regular B star, albeit a fast-rotating one. Two well-known examples of this are δ Sco, that always was classified as a B star and then formed a disk in 2000 (Miroshnichenko et al., 2001) and π Aqr, that went through well-documented phases of disk formation and dissipation (Bjorkman et al., 2002). This on and off nature of Be stars is of great interest, as disk build-up and dissipation can happen in a matter of months, making them a relevant laboratory to study viscous disk dynamics in human timescales.

The variable nature of Be star disks have been the focus of many works, even before the paradigm of the VDD was established. Spectroscopic surveys keeping track of H α and H β line variations date back to the 60's (Jaschek et al., 1964), and polarimetric surveys to the 70's (Coyne, 1976), both of which are intrinsically connected with disk variability.

With the VDD as bedrock, more recent works attempted to parametrize the time changing disk structure of Be stars, although they are still few in number. Jones et al. (2008) combines a radiative transfer code with a hydrodynamic code in order to create dynamic Be star models, feeding one code's results into the other as to observe the changes in the density and temperature structure, and the H α line profile. Haubois et al. (2012) goes further still, combining the radiative transfer code HDUST (Carciofi and Bjorkman 2006, Carciofi and Bjorkman 2008) with the hydrodynamic code SINGLEBE (Okazaki et al. 2002, Okazaki 2007) to recover the density structure variation in build-up and dissipation for different α (see their Fig. 1) and mass injection rates (their Fig. 7). With the intent of studying how disk build-up and dissipation would present in photometric data, they built model lightcurves for their models, showing that this observable can be very telling when it comes to disk variability. Carciofi et al. (2012) does similar work with lightcurves, but model the disk build-up and dissipation events of a real Be star, 28 CMa, for the first time deriving the value of α for a Be disk. At the time, the value found was of 1.0 ± 0.2 .

Another accomplishment for the VDD in terms of Be disk variability comes from Vieira et al. (2015) and Vieira et al. (2017). Vieira et al. (2015) developed the pseudo-photosphere model, another formulation capable of calculating the disk flux emission and spectral slope in a faster and simpler fashion than the computationally expensive HDUST. In this model, the disk is split in two parts: the inner optically thick region (the pseudophotosphere) and the outer optically thin region. The followup work Vieira et al. (2017) revisits Waters et al. (1987), which determined the disk structure of 54 Be stars using their (now outdated) outflowing disk model and IR SED data, with the VDD model, considering also Be star physics discovered subsequent to Waters et al.'s work. They analysed a total of 80 Be stars, and found that, in general, the disk density exponent (n from Eq. 1.13) lies between 1.5 and 3.5, and the most common value for the base density is $\rho_0 \simeq 10^{-12} \text{ g/cm}^3$, going as high as 10^{-10} (see Fig. 7 of Vieira et al. 2017 for a ρ_0 vs n plot for their targets).

Vieira et al. takes advantage of the time period between their IR datasets² to draw the path their target Be stars travelled on the ρ_0 vs n plot during that period, as shown in Fig. 1.3. The authors then computed what the evolutionary tracks of the disks of different types of Be stars would look like in their ρ_0 vs n plot (their Fig. 12), and were able to divide the plot in regions according to the state of the disk: forming, steady-state, or dissipating

² AKARI ran from May 2006 to August 2007, and ALLWISE from January to November 2010.

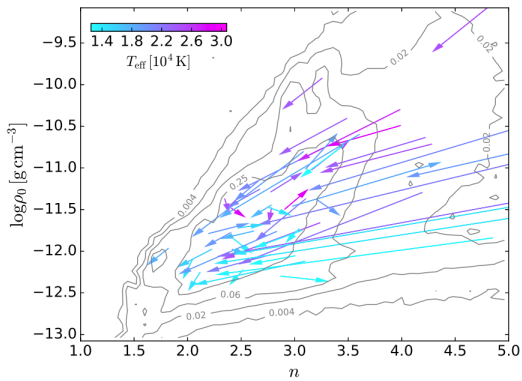


Figure 1.3: Figure 11 of Vieira et al. (2017). Their caption reads: “Evolution of the disc parameters between different epochs. The arrow tails correspond to values derived from AKARI observations, while the arrow heads correspond to determinations from AllWISE data. The arrows were superimposed on the probability distribution of the fitted parameters (see Figure 7), and their colors correspond to the effective temperature determined by Frémat et al. (2005)”

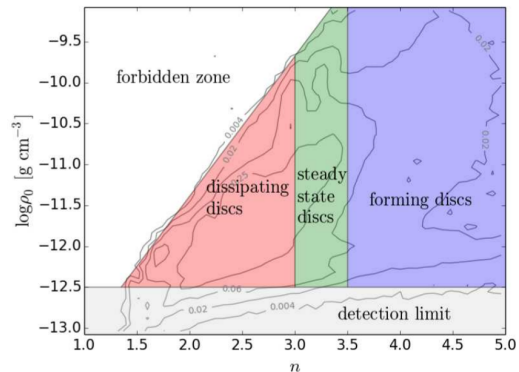


Figure 1.4: Figure 13 of Vieira et al. (2017). Their caption reads: “Typical regions for distinct disc dynamical states in the n vs $\log \rho_0$ diagram, according to VDD hydrodynamical simulations. The defined regions were superimposed on the combined EMCEE posterior distributions for our sample (see Figure 7)”. Most of the stars in their sample fall in the “dissipating” region.

(their Fig. 13, reproduced here in Fig. 1.4). As such, most of the stars analysed are shown to be in the “dissipating” region, which agree with the fact that disk dissipation takes longer than build-up. It is also worth noting that the region classified as “steady-state” corresponds not only to the canonical value of $n = 3.5$, but extends downwards to $n = 3.0$. This discrepancy is likely due to effects not considered in the steady-state VDD solution, such as variable α and non-isothermal effects.

The recent works of Rímulo et al. (2018), and A. Figueiredo (MSc disseration) go deeper into the subject matter of Be disk variability in the VDD framework. They study the light curves of 54 Be stars in the SMC and 83 in the LMC looking for disk build-up and dissipation events. These events appear in light curves as photometric bumps or dips (Fig. 1.5). When seen at a pole-on orientation, the formation of a disk results in a net brightening of the system in the visible (bump), while at edge-on the same even appears as a fading (dip), as the disk now lies between the star and the observer, partially obscuring the view.

Rímulo et al. (2018) proved that, in order to correctly analyse disk events, the history of the build-up must be taken into account, since the longer a disk spends in a mass ejection stage, the more matter will be present in the disk in what the authors call a “mass

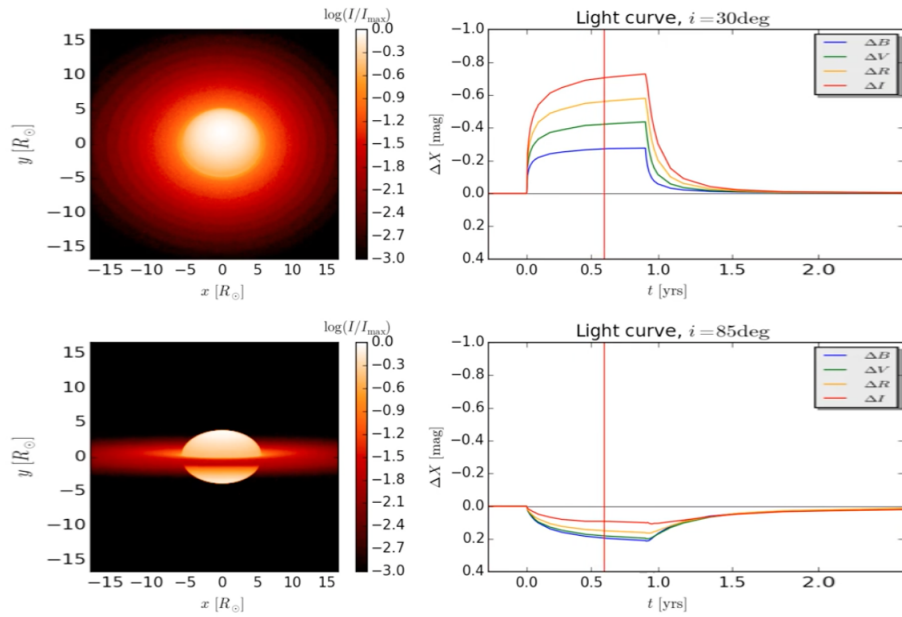


Figure 1.5: Visual representation of a Be star with a newly formed disk and its corresponding light curve, for different inclination angles and for BVRI filters, as indicated. Figure by L. Rímulo

reservoir”. The accumulation of mass at large radii is very difficult to detect via observation and can be overlooked, which leads to incorrect estimates of the disk dissipation time and viscosity. This was dubbed “mass reservoir effect”. With this in mind, Ghoreyshi et al. (2018) revisited the work of Carciofi et al. (2012) with 28 CMa, now with lightcurves covering a longer time period, and multiple disk events, and found $\alpha = 0.21 \pm 0.05$ for the dissipation event of the disk in 2003. It is clear, therefore, that modeling these light curves provides information on the viscosity of the disk, as well as the rate of angular and mass loss rates from the star during the event.

Rímulo et al. and Ghoreyshi et al. find α values are typically of the order of a few tenths in accordance with studies of dwarf novae light curve variations (King et al., 2007), but much larger than theoretical models (e.g. Balbus and Hawley 1991) predict. In addition to the discrepancy in values, their results indicate that viscosity is variable in time. As shown in Ghoreyshi et al.’s Fig. 11, for instance, viscosity in 28 CMa’s disk varies not only from disk event to disk event, but also within a single given event. Recent results (Ghoreyshi, priv. comm.) indicate that α may also vary radially. This leads to a situation where α changes with both time and radius of the disk, which would immediately contradict the steady-state results of Eqs. 1.10 and 1.13.

An intriguing result that also arose from these works is that the angular momentum and

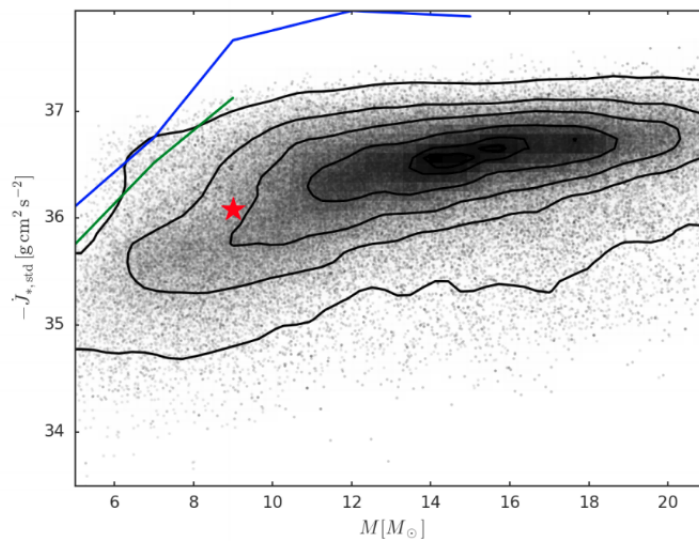


Figure 1.6: Angular momentum loss versus stellar mass diagram calculated by Rímulo et al. (2018) compared to Granada et al. (2013) predictions in blue for the SMC and in green for the Galaxy. The red star represents 28 CMa.

mass loss rates derived by their lightcurve method do not match the ones expected from Be star evolution models of Granada et al. (2013) by one order of magnitude, as shown in Fig. 1.6. Since the method itself is quite reliable, it is likely that adjustments to the constraints of these evolutionary models are required, once more proving the importance studying Be stars in the context of stellar evolution.

One more source of variability for Be stars comes from interactions with close binary companions. For early B stars, as massive stars, it is common to be in a binary system. According to Sana et al. (2012), 70% of all massive stars have, at some point of their lives, a binary companion, and suffered mass exchange. Oudmaijer and Parr (2010) finds a binary percentage of $30 \pm 8\%$ for Be stars specifically, while Chini et al. (2012)'s values range from $46 \pm 3\%$ for early-type³ B stars and $19 \pm 2\%$ for late-type⁴.

The most rambunctious members of the Be binary group are the Be X-ray binaries (BeXRB), Be stars with compact objects as companions in eccentric orbits. In these systems, the compact object passes through or close to the disk during its orbit around the Be star, and accretes matter onto itself. The kinetic energy of the in-falling matter is high enough that it converts into X-rays as it falls into the gravitational well of the

³ Spectral classes B0-B3

⁴ Spectral classes B4-B9

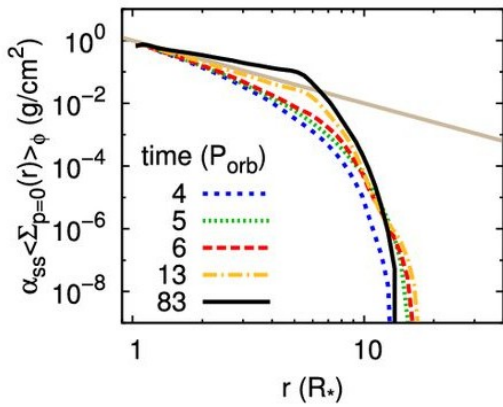
compact object. A recent review on the subject is given by Reig (2011). They put the number of confirmed BeXRB systems in the Galaxy at 28, while the online catalogue of Raguzova and Popov (2005)⁵ points to 72 confirmed and candidate BeXRB. Interestingly, although they are assumed to exist, no BeXRB with a white dwarf companion has been detected yet, and only one with a black hole companion (Casares et al., 2014). All others are Be+NS systems. Be stars with sub-dwarf companions are also assumed to be numerous (5 confirmed and several candidates - Wang et al. 2018), but hard to detect given their relative brightness to the Be star. These are all interesting as they are the outcome of binary evolution through Roche lobe overflow, where the Be star stole mass from its more evolved companion until it lost its outer envelope and became a sub-dwarf or a compact object.

Whatever its nature, a companion passing close to the disk will disrupt it in some way or another. Okazaki et al. (2002) simulated a BeXRB system using a 3D smoothed particle hydrodynamic (SPH) code modified for Be disks in the context of the VDD model. The companion acts on the disk mainly through tidal interaction, and, depending on the orbital parameters, can lead to the creation of complex density structures in the disk such as two-armed density waves. This truncation is the result of the resonant torque of the companion on the Be disk. Although the term “truncation” suggests a rather blunt cut in the density, disk truncation represents a gradual diminishing the density over an extended region dubbed truncation region, beyond which it falls to nearly zero (Fig. 1.7b). It is, however, usually approximated by a truncation radius. Another characteristic of Be binaries is the accumulation of matter in the disk caused by the perimeter set by the companion in orbit (Fig. 1.7a).

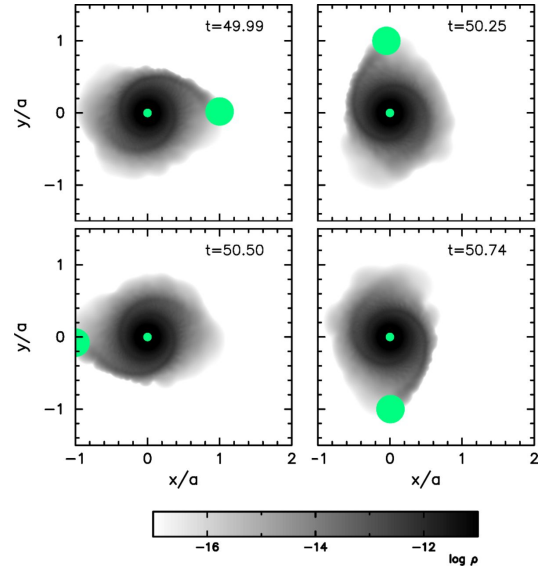
The work of Panoglou et al. (2016) studies the effect of binarity on coplanar orbits, while Cyr et al. (2017) focuses on tilted orbits using the SPH code from Okazaki et al. (2002). Evidence of disk truncation and two-armed density waves are confirmed. In particular, Panoglou et al. (2016) find the truncation radius R_D , if we assume a coplanar, circular orbit of the secondary, relates to the orbital separation of the system as $R_{orb} \approx R_D/0.8$.

Thus, it is abundantly clear that the disks of Be stars are subject to many physical processes that can lead to variability, in time scales of days (in the case of density structures causes by close companions) to years (the longest disk build-up events). This by no means

⁵ <http://xray.sai.msu.ru/~raguzova/BeXcat/node3.html>



(a) Figure 2 of Panoglou et al. (2016). Averaged surface density for a system with mass ratio $q = 1$. Each lines represents the surface density at the periastron passage at five different points in time; from bottom up more evolved, $t = 4, 5, 6, 13, 83$ months. The solid straight line shows the density profile for an infinite disk. We can see the accumulation effect clearly in the solid black line.



(b) Figure 4 of Panoglou et al. (2016). Snapshots of the reference binary system at quasi-steady state. The distances are given in semi-major axis units. The two-armed structures can be easily seen, as well as the fact that the disk is not present beyond the companion.

Figure 1.7: Effects of the secondary on the Be disk for a close binary system. Panel (a) shows the accumulation effect while panel (b) shows the two-armed structures and truncation.

undermines the usefulness of the power-law solution, as its directness is still a powerful tool in the matter of non-time variant studies, and even in quantized (snapshots) approach to time variability (as in Vieira et al. 2017).

1.4.2 Central Star

The central star is also astrophysically interesting on its own. Be stars are the fastest rotating non-degenerate stars, with some thought to be rotating nearly at the critical limit (e.g. α Eri - Domiciano de Souza et al. 2012). This makes them a valuable study for how rotation affects stellar evolution along the main sequence.

One of the most dramatic effects of their rotation is stellar oblateness: given the velocity at the equator, the gravity diminishes to the point where the equator grows, creating an oblate shape. In order to quantify the rotation of the star, it is useful to define the rotation rate W ,

$$W = \frac{v_{rot}}{v_{orb}}, \quad (1.14)$$

where v_{rot} is the rotational velocity at the equator. When $W = 1$, the star is said to be rotating critically. Using the Roche approximation (Cranmer, 1996), the rotation rate relates to oblateness as

$$\frac{R_{eq}}{R_{pole}} = \frac{W^2}{2} + 1. \quad (1.15)$$

Due to rotation, Be stars evolve as if they were less massive than they actually are, spending more time on the main sequence. This is a result of the rotational mixing bringing fresh H-fuel into the convective core, keeping it burning for a longer time. Furthermore, the rotation partially sustains the core against the gravitational force, leading to lower pressure and consequently a lower burning rate (Meynet and Maeder, 2000).

Rapid rotation also leads to gravity darkening (GD), where the equator of the star is darkened in relation to the poles. The effect is due to the fact that, if the star is in radiative equilibrium (as we assume), the emitted flux will be proportional to the local gravity. In the case of Be stars, the gravity at the equator is smaller than at the poles. Therefore, the brightest and hottest region of these stars is the pole, while the equator is colder and dimmer. GD was first suggested by von Zeipel (1924), and is parametrized as

$$T_{eff} \propto g_{eff}^{\beta_s}, \quad (1.16)$$

with the exponent once suggested to be fixed at 0.25, but nowadays it is used as a parameter variable with W (Espinosa Lara and Rieutord, 2011). Townsend et al. (2004) notes that not considering the effects of GD on line formation (see Sec. 1.4.3.1 for more details) leads to underestimated values of the projected velocity of Be stars, $v \sin(i)$, by tens of percent, as the slowly rotating hot regions would outshine the fast rotating cold equator. Frémat et al. (2005) expands on how GD affects the inference of stellar parameters, recalculating T_{eff} , $v \sin(i)$, $\log(g)$ and inclination for 130 Be stars.

Whether or not Be stars are critical rotators has been debated for a long time in the Be field. Zorec et al. (2016) in their survey of 233 Be stars comes to the conclusion that the Be phenomenon happens in a wide range of rotational velocities, strongly implying that Be stars are not critical, although they are still very rapid rotators.

But how do Be stars acquire such high rotational velocities in the first place? This is still an open question in the field, with three likely solutions. The first is that these stars are simply born this way, and being a Be star is an innate characteristic (Zorec and Briot, 1997). The second suggests that the star spins up is a consequence of the stellar evolution along the main sequence. One prediction of stellar evolution models is the acceleration of the outer layers of the star as a result of the contraction of the core. Core contraction would cause AM to be redistributed in the star and so the angular rotation of its outer layers would increase, even reaching critical value (Ekström et al. 2008, Granada et al. 2013). This scenario requires the star to have already been born a quite fast rotator. It also requires quite efficient transport mechanisms within the star, which may not be the case, as recent results suggest (Rímulo et al., 2018). Also, the Be phenomenon would be terminated after the star leaves the MS, due to the expansion of its outer layers.

The third is binarity. Pols et al. (1991) considers in their work the possibility that Be stars are formed through the evolution of mass-transfer close binaries. This scenario involves a system with two intermediate mass interactive binaries, with the donor about to enter the red giant phase. The B star receives mass and AM from its companion, that evolves to become either a He star (or sub-dwarf O) or a compact star. Their results suggest that up to half of the Be star population might have been formed this way. To better test this hypothesis, however, these companions must be detected, which is a difficult task (see Sec. 1.4.1.2). Pols et al. came to the conclusion that no more than 60% of the total number of Be stars would be formed this way. More recent works diverge, with van Bever

and Vanbeveren (1997) finding a maximum of 20% and Zorec and Briot (1997) with an upper limit of 30%. Klement et al. (2017), however, finds indication that, from a sample of 9 Be stars, all show strong signs of presently having a binary companion. The author’s more recent work (Klement et al., 2019) increases the sample, and find the impressive indication that, for all the 23 stars they acquired reliable data on, the percentage may be close to 100%.

In all scenarios, rapid rotation is believed to be an integral part of what makes a Be star a Be star, a piece of the so called *Be phenomenon*, the elusive matter ejecting mechanism and its activation. And if they are not critical, but rather rotate with $W \sim 0.7$ (Rivinius et al. 2006, Huang et al. 2010, among others), then an additional physical mechanism is necessary to catapult matter into orbit. Nowadays, the most likely culprit is believed to be non-radial pulsations (NRP).

The possibility exists that all Be stars are pulsators, as every Be star observed with good enough sensitivity has found indication of multi-mode NPR. The main theory is that beat patterns of NPR modes would provide enough energy to strip the matter from the already weakly gravitationally connected equator (Rivinius et al. 1998, Kurtz et al. 2015). Another possibility is that the difference between two parent signals can form a composed mode of nearly sinusoidal variability with a frequency close to the difference of its parent frequencies. In both cases, the resulting pulsation can have an amplitude that exceeds the sum of its parent modes and could kickstart ejection. The most complete works on the subject are the series of papers “Short-term variability and mass loss in Be stars” (Baade et al. 2016, Rivinius et al. 2016, Baade et al. 2018 and Baade et al. 2018b), which analyse photometric data from the BRITe Constellation nanosatellite mission (Pablo et al., 2016) in search for these patterns and (hopefully) their connected mass loss events.

1.4.3 Observational Characteristics

Although complex and variable systems, Be stars have several observational characteristics that are present in their whole class, when in active phase. The most well known are the Balmer lines in emission from which they get their name, the excess in the visible IR region, and radio regions of their SED, and the linear polarization, all caused by the presence of the circumstellar material. We go further into those aspects and more in the following subsections.

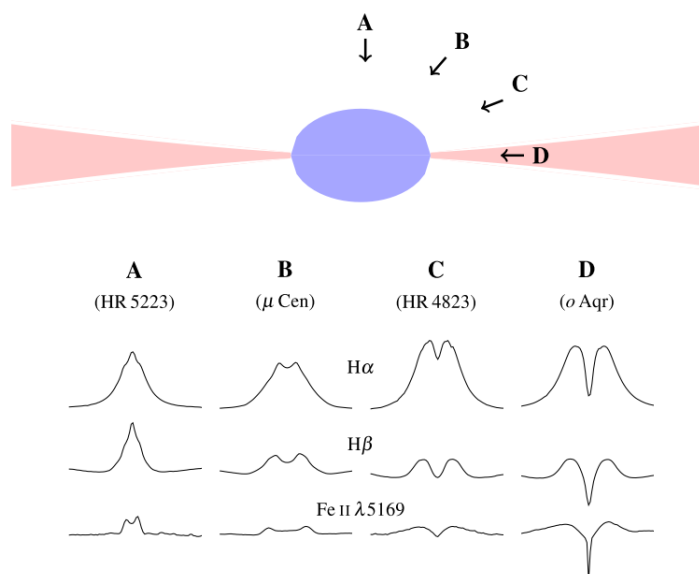


Figure 1.8: Emission line profiles for different inclination angles of Be stars, as per Struve’s model (Rivinius et al. 2013, Fig. 1).

1.4.3.1 Spectral Lines

Since Secchi (1866) discovered the first Be star from its unusual emission H β line, Balmer lines (H α , β , γ , etc.) in emission became the most discerning attribute of the class. The central star excites and partially ionizes the colder gaseous disk. These lines are called recombination lines because they usually are formed when an electron is captured by a proton, forming a neutral H atom in an excited state that later de-excites, leading to emission lines. We also see emission lines in HeI, and metal lines such as FeII, SiII, and MgII. Struve (1931) noted in his work that due to the circumstellar and rotating nature of the disk, the inclination at which the system was observed would lead to different line profiles, as shown in Fig. 1.8.

When the system is seen at a completely edge-on orientation, with the disk obscuring the star and reabsorbing its own emission along the line of sight, a strong absorption line is also formed along with the two-peaked emission, becoming a “Shell” profile (Fig. 1.8, column D). At pole on, the Doppler effect of the disk rotation on the line is non-existing, but non-coherent scattering broadening (Hummel and Dachs, 1992) shifts the two peaks slightly, leading to a “wine bottle” profile (Fig. 1.8, column A). As the inclination increases, the central reversal become more and more prominent, and the violet and red peaks are very distinguishable. As the peaks arise due to the Doppler of the rotation of the disk,

variation of these peaks relative strengths (V/R variations) indicate different densities of the part of the disk moving towards us and the part moving away. As previously mentioned (Sec 1.4.1), this was studied in Okazaki (1991)'s work on global disk oscillations.

Photospheric lines are, of course, also present in Be star spectra. The star's high rotation leads to rotational broadening of these absorption lines, making them shallow. Gravity darkening and oblateness also modify these lines, as the shape and temperature of the stellar surface is greatly affected. Some lines will be controlled by the hot polar region, while others will form in the cold equator. As the star in question is a B type, which emits strongly in the UV, lines in this spectral region are the most affected by its peculiarities (Rivinius et al., 2013).

1.4.3.2 Continuum Emission

The continuum emission of Be stars is also very dependent on the inclination angle at which we see the system, and presents itself differently depending on the emission wavelength. The star is obviously a source of continuum emission, and so is the disk as it absorbs, reprocesses and scatters radiation. The two main sources of continuum radiation are electron recombination with neutral H atoms and free-free emission, both of which depend strongly on the density, temperature and general geometry of the disk.

The UV flux is mainly controlled by the star, but also affected by the disk: for a pole-on case, the scattering off the disk will increase the flux, while on edge-on cases it will absorb part of the flux coming from the colder equator and re-emit the rest in IR wavelengths (see Fig. 1.9).

In other wavelengths, the concept of pseudo-photosphere (Vieira et al., 2015) is useful. The size of the pseudo-photosphere also has a wavelength dependency. The final flux will be a combination of the emission of the optically thick pseudo-photosphere and the optically thin outer disk. At wavelengths larger than visible, the size of the pseudo-photosphere grows, meaning that larger and larger areas of the disk contribute more to the emission. From mid-infrared onward, the disk dominates as the emitting area grows. When the inclination goes to more edge-on cases, self-absorption on the disk and the obstruction of the central star become more relevant. For wavelengths where the pseudo-photosphere is small, a large part of the flux will be depleted, but if it is large, then the increased emitting area will lead to a brightening of the system.

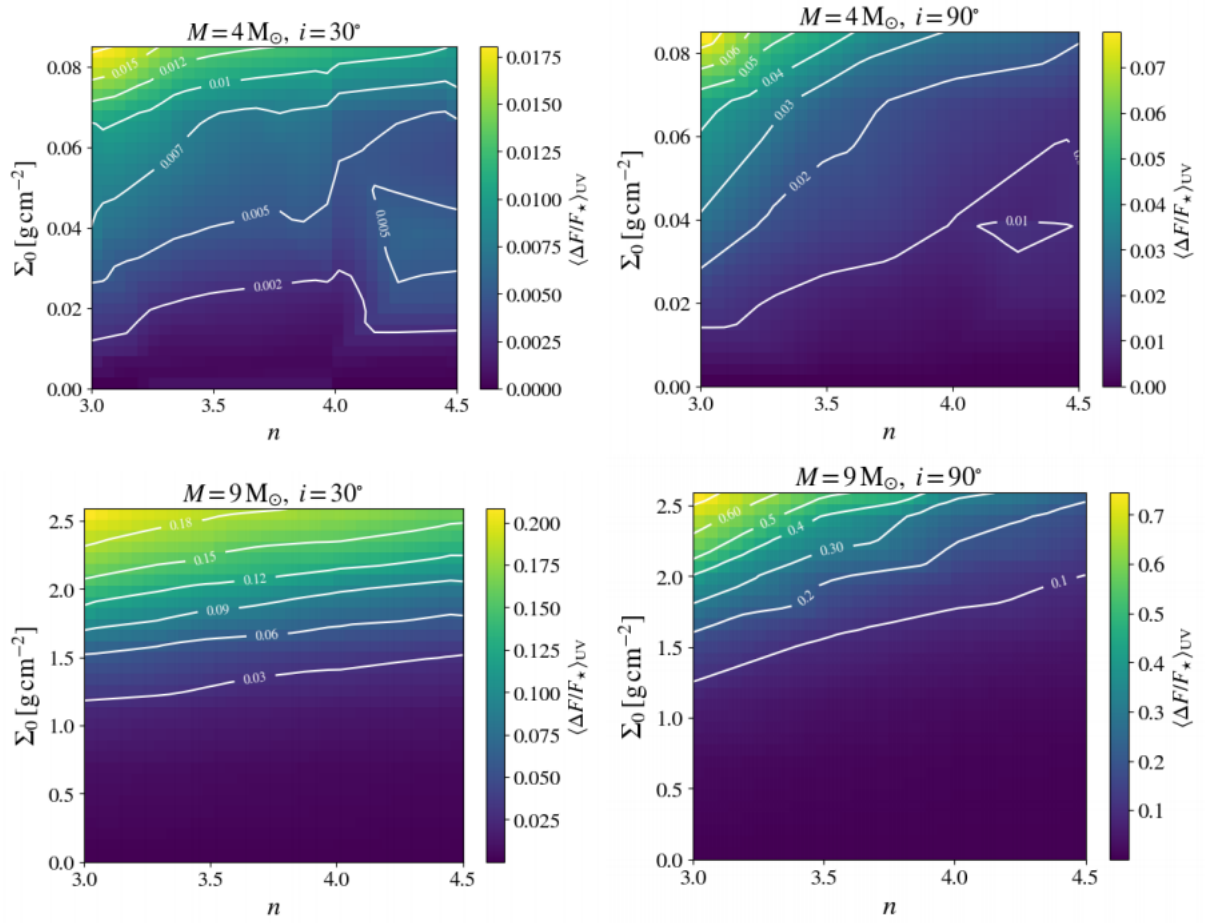


Figure 1.9: Figure 5.2 from Mota (2019). Top: UV disk effect function of a typical late-type Be star ($M = 4 M_{\odot}$) at different orientations. Left: $i = 30^{\circ}$. Right: $i = 90^{\circ}$. Bottom: the same, but for a Be star of $9 M_{\odot}$

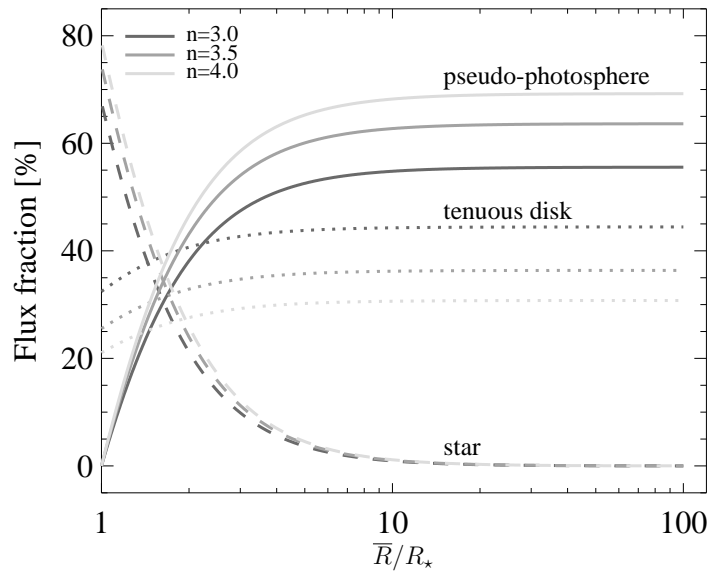


Figure 1.10: Figure showing the contribution of different Be star components to the flux as we increase the effective radius of the pseudo-photosphere. Figure from Vieira et al. (2015)

A takeaway from this discussion is that emission in different wavelengths are formed in different parts of the Be system, such as the central star dominating the UV emission, and the disk dominating in the IR region, as shown in Fig. 1.10. Thus, photometric bands correspond to different regions of the disk, with the V band coming mostly from the first $\sim 2R_\star$ of the disk and $60\mu\text{m}$ band from the much larger area of 1 to $\sim 15R_\star$.

1.4.3.3 Linear Polarization

When the unpolarized light from the central star hits the ionized thin disk, it is scattered in multiple directions and becomes polarized perpendicular to the disk plane. The polarization P depends on the asymmetry of the disk and the inclination angle, so if we see a Be star with an axi-symmetric disk perfectly pole-on, it will be zero. Attenuating effects such as absorption or re-scattering of the polarized light make it so the maximum value of P is reached at the intermediate inclinations of $70 - 80^\circ$ (Halonen and Jones, 2013). For Be stars, the highest P are of about 2%.

1.5 Objective of this dissertation

With this introduction on Classical Be stars, their viscous α -disks, and most prominent observational characteristics, we hope that the reader is well informed enough to

understand in depth the work presented in this dissertation.

The multi-technique works of Carciofi et al. (2009) and Klement et al. (2015) were important to cement the VDD as the paradigm for Be. They combined different types of observations (observables) and compared them to radiative transfer models to find the parameters that best described the central star and the disk of a Be star. As long as the Be disk is stable, the steady-state approximation was proved to describe the system satisfactorily.

Although those results are very satisfying, there is a clear need to make multi-technique modelling more robust. In this MSc dissertation, I, in collaboration with the PhD student Bruno Mota and the former post-doctoral researchers Rodrigo Vieira and Daniel Moser, helped develop a new approach that aims at improving the procedure of performing a simultaneous fit of all observables and inferring both stellar and disk parameters at once using Monte Carlo Markov chain (MCMC) based Bayesian data analysis. This resulted in the creation of the comprehensive grid of Be star models BeAtlas and the MCMC PYTHON package BEMCEE, described in details in Mota (2019).

Here, we use BeAtlas and BEMCEE, and photometric, polarimetric, and spectroscopic observational data to derive the defining parameters of the stable Be star α Col. This approach is a step up from the multi-technique analysis works cited in Sec. 1.4.1, as it derives not only the best fit result for a model fitting, but calculates the probability density function (PDF) of each parameter, and the correlations between them, allowing for a more robust determination and more grounded interpretation. Furthermore, our work allows us to identify which observables are optimally suited for constraining different parameters. This is a sister work to that of B. Mota's PhD thesis (Mota, 2019), as the procedure used is the same.

In Sec. 2.1 of chapter 2, we describe α Col as a Be star, presenting literature data and analysis, and the data used in this work: SED photometry, polarimetry and H α and UV spectroscopy. The following two sections describe theoretical tools: Sec. 2.2 refers to the workings of the HDUST code and Sec. 2.3 the Bayesian-MCMC methods. The next chapter explains the methodology behind this research. We detail the grid of models BeAtlas in Sec. 3.1 and the MCMC code BEMCEE in Sec. 3.2. Our results are presented in Chpt. 4.

Data and Tools

In this chapter we describe the main tools and data used in this project. Sec. 2.1 describes the star studied here, α Col. Sec. 2.2 is a brief overview of the 3D Monte Carlo radiative transfer code of Carciofi and Bjorkman (2006, 2008) used to generate state of the art Be star models, while Sec. 2.3 deals with Bayesian formulation and Monte Carlo Markov chains methods.

2.1 α Columbae

α Columbae (also known as Phact, HD 37795, and HR 1956) is the brightest star of the Dove constellation (*Columba*), with a right ascension of 05 39 38.94103 and declination of -34 04 26.7950, with an apparent magnitude of 2.65 in the V band ¹. It has been classified as a B9Ve star by Levenhagen and Leister (2006), but previous analysis in literature suggest it might be a B7 or B8 (Skiff 2014 - see Table 2.1 for all literature determinations). In 1897 was discovered to be a Be star (Jaschek et al., 1964), and being bright, it has been target of many observations over the years. Since then, α Col showed very little variation, as noted by Jaschek et al. (1964) in their spectroscopic survey. Dachs et al. (1981) and Slettebak (1982) also report no major variation in their observations of α Col. Weak variation in H β line profiles was studied by Bijaoui and Doazan (1979), and Jaschek et al. (1969) mentions stronger violet peaks for H β .

Our goal is to find the stellar and disk parameters that best describe this Be star, so data collection is paramount. We collected observational data in photometry (both optical and infrared), radio data, spectroscopy, polarimetry and interferometry. We have data

¹ <http://simbad.u-strasbg.fr/simbad/sim-id?Ident=alp+col&NbIdent=1&Radius=2&Radius.unit=arcmin&submit=submit+id>

V mag	Spectral Type	Reference
2.60	B5e	Cannon and Pickering (1918)
2.70	B6e	Rimmer (1930)
2.60	B8ne	Merrill and Burwell (1933)
2.70	B8Ve	Woods (1955)
2.70	B7Ve	Jaschek et al. (1969)
2.60	B7IV	Hiltner et al. (1969)
2.60	B8Vn	Molnar (1972)
2.70	B7V	Cucchiaro et al. (1977)
2.70	B7IVe	Slettebak (1982)
2.60	B7IV	Houk (1982)
2.70	B9Ve	Levenhagen and Leister (2006)

Table 2.1 - Spectral types in literature for α Col, from the Catalogue of Stellar Spectral Classifications (Skiff, 2014)

from ESO telescopes (AMBER interferometry, and FEROS spectroscopy), the BeSS² and BeSOS³ catalogues, polarimetric data from Observatório Pico dos Dias (OPD), spectroscopy from ESPaDOnS⁴ and photometry from VOSA⁵ and IUE⁶.

2.1.1 Ultraviolet spectra

For the UV region of the spectrum, we used data from the International Ultraviolet Explorer (IUE)⁷ obtained from the INES Archive Data Centre⁸. We selected the spectra taken in IUE's large aperture mode, comprised of an oval window of 10x20 arcsec, as there was only one spectra available with the small aperture configuration. 13 spectra were obtained in total, 3 with the Long Wavelength Prime camera (covering from 1850 to 3350Å) and 10 with the Short Wavelength Prime camera (1150-1980Å). There was only high dispersion data available. There was no significant variation in the spectra, therefore they are simply averaged and binned to match the models' resolution in the analysis.

² <http://basebe.obspm.fr/basebe/>

³ <http://besos.ifa.uv.cl>

⁴ <http://www.cadc-ccda.hia-ihp.nrc-cnrc.gc.ca/en/cfht/>

⁵ <http://svo2.cab.inta-csic.es/theory/vosa/>

⁶ http://sdc.cab.inta-csic.es/ines/Ines_PCentre/ines_sys.html

⁷ <http://sci.esa.int/iue/31284-summary/>

⁸ <http://sdc.cab.inta-csic.es/cgi-ines/IUEdbsMY>

Table 2.2 - SED fluxes from 0.3 μm to 6.3 cm. References are given in the text.

Instrument/Filter	λ [μm]	Flux [$\text{erg/s/cm}^2/\mu \text{ e-6}$]
Johnson U	0.36	5.224 ± 0.131
TYCHO B	0.43	6.514 ± 0.084
Johnson B	0.44	6.116 ± 0.061
TYCHO V	0.53	3.606 ± 0.030
Johnson V	0.55	3.107 ± 0.029
2MASS J	1.2	$2.593\text{e-1} \pm 0.659\text{e-1}$
2MASS H	1.6	$8.477\text{e-2} \pm 1.764\text{e-2}$
2MASS Ks	2.1	$3.160\text{e-2} \pm 0.763\text{e-2}$
AKARI/IRC	9	$2.500\text{e-4} \pm 0.008\text{e-4}$
IRAS	12	$1.715\text{e-4} \pm 0.051\text{e-4}$
WISE W3	11.5	$8.217\text{e-5} \pm 0.091\text{e-5}$
AKARI/IRC	18	$2.397\text{e-5} \pm 0.016\text{e-5}$
IRAS	25	$1.785\text{e-5} \pm 0.090\text{e-5}$
WISE W4	22	$1.331\text{e-5} \pm 0.020\text{e-5}$
IRAS	60	$1.142\text{e-6} \pm 0.080\text{e-6}$
APEX	870	$2.477\text{e-12} \pm 0.115\text{e-12}$
VLA	20000	$2.250\text{e-17} \pm 6.750\text{e-17}$
ATCA	35000	$2.204\text{e-18} \pm 6.612\text{e-18}$
ATCA	63000	$1.134\text{e-18} \pm 3.401\text{e-18}$

2.1.2 Visible - Radio observations

For the visible up to the far-infrared region we collected photometric data using the Virtual Observatory SED Analyser (VOSA)⁹ tool that gathers data from multiple catalogues. The acquired data was collected from catalogues Hipparcos (ESA, 1997), 2MASS (Skrutskie et al., 2006), TYCHO (Høg et al., 2000), and the Catalogue of Homogeneous Means in the UBV System (Mermilliod, 1997) in the visual, and IRAS¹⁰, WISE (Cutri and et al., 2014) and AKARI (Doi et al., 2015) in IR. We also have an APEX measurement from the European Southern Observatory's LABOCA instrument at 870 μm , and literature upper limit data from Clark et al. (1998) (Australian Telescope Compact Array - ATCA) and Taylor et al. (1990) (National Radio Astronomy Observatory's Very Large Array - VLA) in the radio region, at 2, 3.5, and 6.3 cm. The wavelengths and flux values of the observations are summarized in Table 2.2.

⁹ <http://svo2.cab.inta-csic.es/theory/vosa/>

¹⁰ <https://irsa.ipac.caltech.edu/Missions/iras.html>

Table 2.3 - $H\alpha$ spectra of α Col collected from various sources and online databases. In total, we had access to 112 spectra.

Instrument	Number of Spectra
ESPaDOnS	41
BeSS	6
BeSOS	9
OPD - MUSICOS	5
OPD - ECASS	3
FEROS	31
UVES	17
TOTAL	112

2.1.3 Polarimetry

The polarimetric data used in this project comes from Prof. Carciofi's research group's observational effort in the Pico dos Dias Observatory (OPD) in Minas Gerais, Brazil. Data was collected in multiple observation runs by members of the group. In most runs, the telescope used was 60 cm Boller & Chivens, but part of the data was also acquired with 160 cm Perkin-Elmer (PE) and 60cm Zeiss telescopes. The polarimeter used was IAGPOL (see Magalhães et al. 1996). For more details on the BEACON group polarimetry survey, see D. Bednarski's MSc dissertation and our website, www.beacon.iag.usp.br. The polarization for U, B, V, R and I filters is shown in Fig. 2.1, organized by observation date. It is clear that variation is very little, never deviating more than 1σ from the mean value, indicated by the gray region. This result confirms that α Col is not in a process of disk build-up or dissipation, both of which would be noticeable in polarization data. It further indicates that the mass injection rate into the disk is very steady over time.

2.1.4 $H\alpha$ spectroscopy

We had available $H\alpha$ spectra from the BeSS and BESOS catalogues, as well as FEROS (from Th. Rivinius and N. Leister), UVES (from ESO's Science Portal¹¹), and ESPaDOnS¹² data, as well as data obtained by the BEACON group at OPD using both ECASS and MUSICOS spectrographs. IN total, 112 spectra.

As they were collected from wildly different sources, each batch of spectra has different

¹¹ <http://archive.eso.org/scienceportal/>

¹² <http://www.cadc-ccda.hia-ihp.nrc-cnrc.gc.ca/AdvancedSearch/>

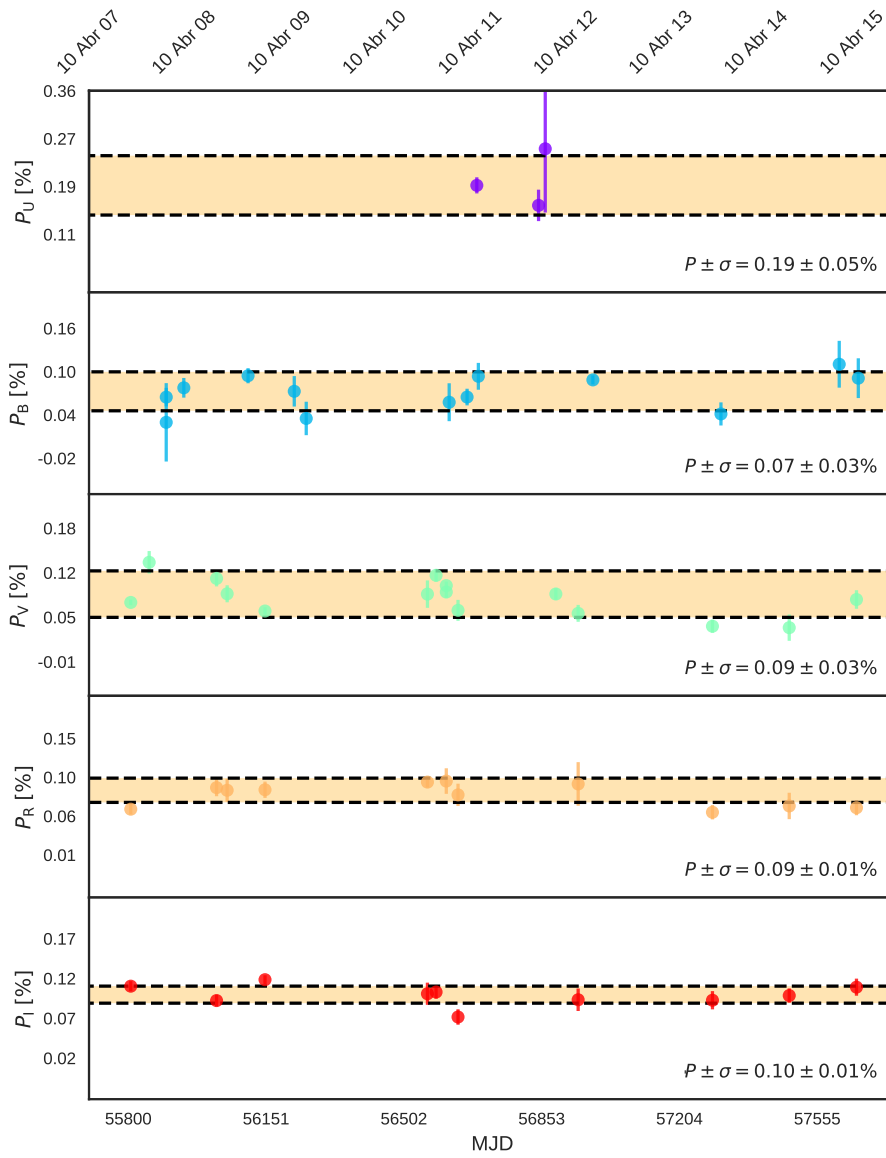


Figure 2.1: OPD polarization data for U, B, V, R and I filters, by date of observation. The orange region indicates $\pm 1\sigma$ from the mean value of the data for each filter.

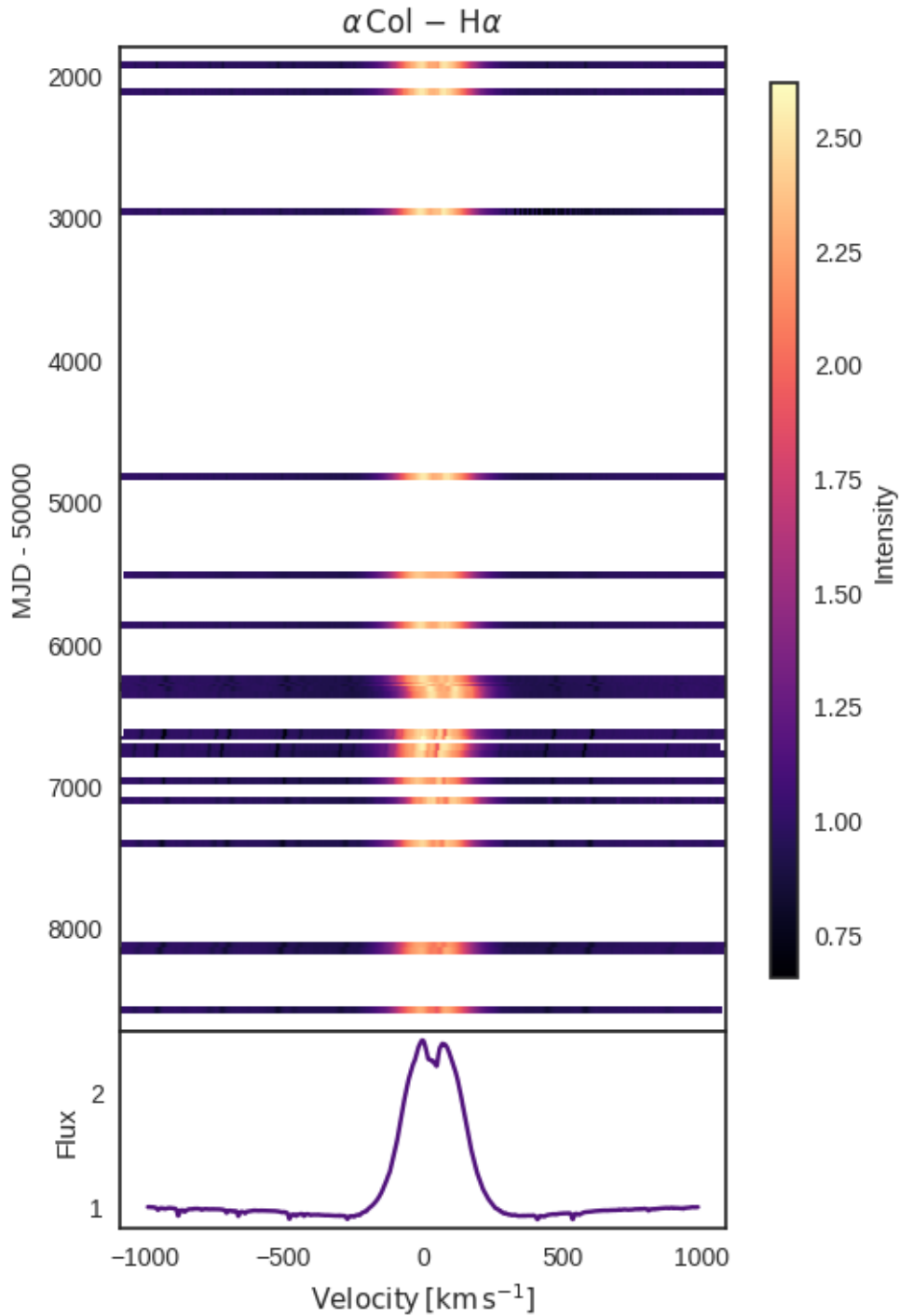


Figure 2.2: Top: dynamic H α spectra from ESPaDOnS, BeSS, the MUSICOS and ECASS OPD spectrographs, FEROS, UVES, and the BeSOS database. Bottom: average line profile.

resolution and calibration in general. ESPaDOnS is a fibre-fed high-resolution echelle spectrograph on the Canadian-France-Hawaiian Telescope (CFHT) reaches an average spectral resolution of about 81000. The BeSS spectra come from various sources: two of the spectra were taken with a LHIRES C11 spectrograph, with a resolution of 14000, another four with a LHIRES III spectrographs mounted on different telescopes (one with resolution of 17000, another with 18000, another with 11000, and the last one with 12000). BeSOS spectra are taken with a high resolution echelle spectrograph called PUCHEROS, with a resolution of 17000. OPD data are taken with either the MUSICOS fibre-fed high-resolution echelle spectrograph, with a resolution of 35000, or with ECASS, a low-resolution (4000) Cassegrain spectrograph. ESO's FEROS is a very high-res echelle spectrograph, with $R = 48000$, while UVES is a high-res optical spectrograph, able to reach $R = 80000$. The available $H\alpha$ line profiles are shown in Fig. 2.2, in the form of a dynamic spectrum. Very little variability is seen in this line, amounting to only 0.3% in equivalent width, measured at -29.71 \AA with a 0.91 \AA standard deviation, as shown in Fig. A.1.

Table A.1 is a compilation of α Col's stellar parameters from several sources, each study using different techniques. According to these data, α Col's mass can vary from 4.4 to $5.7 M_{\odot}$. Its $v_{\text{crit}} = \sqrt{\frac{2}{3} \frac{GM}{R_{\text{pole}}}}$ seems to be around 350 km/s, the $v \sin(i)$ close to 190 km/s, and inclination between 30 and 60° , but likely the true inclination is closer to the interferometric determination of Meilland et al. (2012) at 35° . The possible value for the effective temperature goes from 12000 to 15500 K, and $\log(g)$ is ~ 3.5 . The stellar radius is not well constrained, but is likely larger than $5 R_{\odot}$. The two determinations for $E(B - V)$ match too: it is very low, at 0.01.

Literature determination for disk parameters is tricky to find, as this kind of analysis is still restricted to few Be stars. However, α Col was one of the stars studied by Waters et al. (1987) in their IR survey of Be stars using IRAS data. They relate the IR excess in 12, 25 and $60 \mu\text{m}$ to disk emission, and fit a simple power-law disk model to their data. For α Col, they find a disk with a log base density of 12.2 ± 0.1 and a radial density exponent of 2.75. In Vieira et al. (2015), this work is revisited, their data being reinterpreted using the pseudo-photosphere model. They find the $n = 2.76_{-0.03}^{+0.04}$ and $\log n_0 = 11.51_{-0.01}^{+0.02}$.

2.2 HDUST

The main tool of the BEACON research group is the HDUST code. HDUST is a FORTRAN code capable of solving the radiative transfer equations in arbitrarily shaped 3D media, using a Monte Carlo technique (see Carciofi and Bjorkman 2006, 2008). HDUST considers in its calculations polarization, multiple scattering effects, radiative and statistical equilibrium conditions in non-local thermodynamic equilibrium (NLTE) regime for the hydrogen population levels in a 3D medium. The code also implements opacity sources such as Thomson scattering, Bremsstrahlung and even dust grains using the Mie theory. Since Be stars are rapid rotators, HDUST also considers effects such as gravity darkening and rotational flattening to accurately describe the central star. The code is capable of simultaneously solving the radiative and thermal equilibrium condition, such that the disk's temperature is obtained self-consistently with the radiative transfer. The code's output consists of images, flux and polarization for any desired spectral interval.

To solve a radiative transfer problem, HDUST uses a Monte Carlo method, simulating the journey of a given number N of photons packets (PPs) through the disk, accounting for their scattering, absorption and re-emission, until they leave the system. The PPs are defined in such a way that all PPs are monochromatic and have the same energy when they leave the star. Since we are dealing with an equilibrium situation, whenever a PP is absorbed, it must be re-emitted with the same energy, but with new direction and frequency as determined by the emissivity at that point in the disk. However, the disk is an enormous structure and many processes can happen in the PPs' way from the star to the exit point, and the MC method is statistical: it must sample a very large number of events in order to determine the disk gas state variables (density, kinetic temperature, and level populations). HDUST deals with this by breaking the disk in thousands of cells, each with a given initial set of state variables, and sampling them individually throughout the MC simulation. At the end of a simulation, the variables are updated and a new simulation begins; this process is repeated until the convergence is reached in each cell.

Fig. 2.3 is a flowchart of the MC calculation performed by HDUST for an envelope of M cells. Through each of the cells, a number of N PPs are absorbed and suffer a given reemission process k . For more details, see the original papers of Carciofi and Bjorkman (2006) and Carciofi and Bjorkman (2008).

HDUST

Step-by-step Monte Carlo calculation. Carciofi & Bjorkman 2006

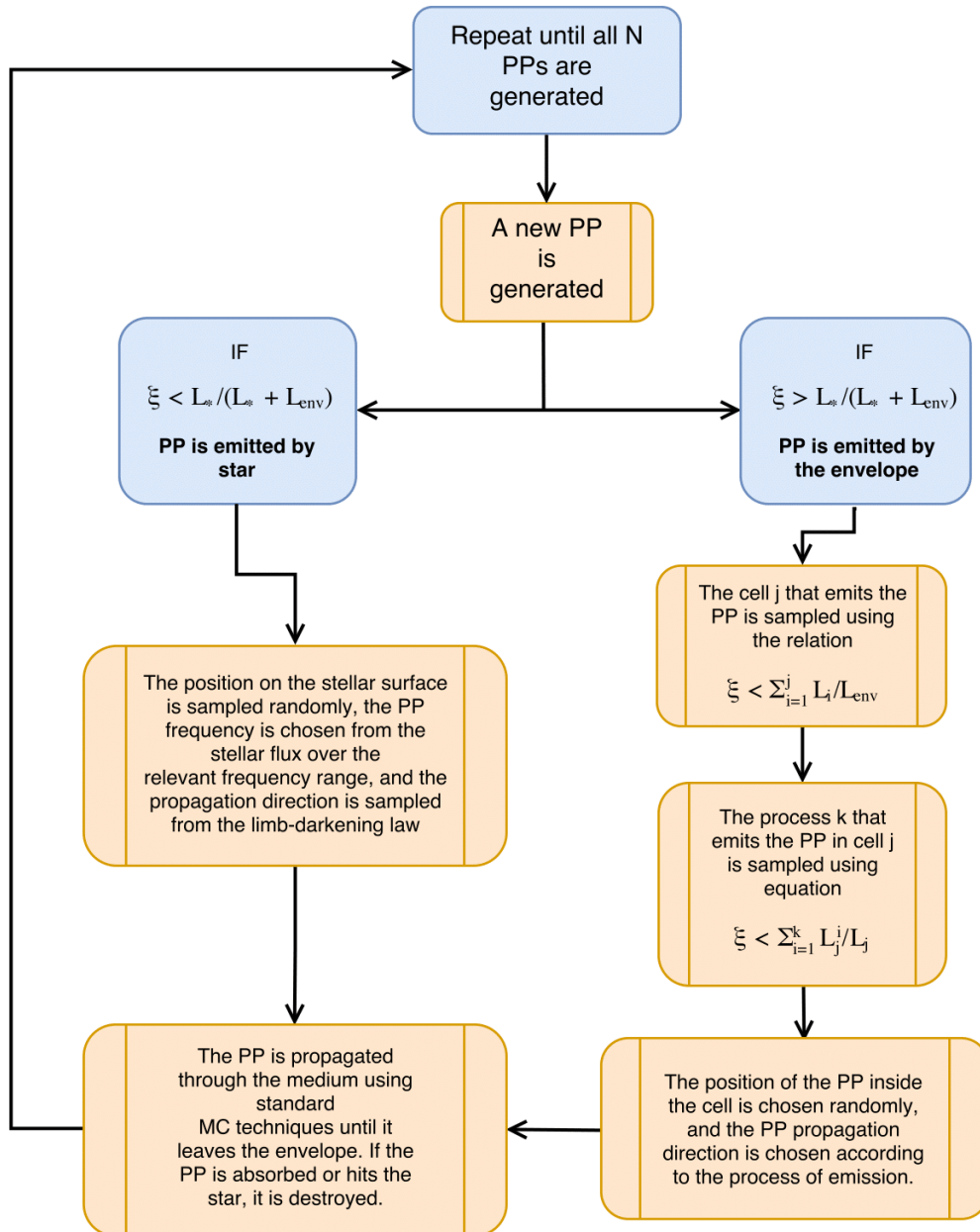


Figure 2.3: Flowchart of HDUST's sampling process, for an envelope of many cells.

The stellar parameters HDUST takes as input are stellar mass (M), pole radius (R_{pole}), rotation rate (W), luminosity (L) and gravity darkening exponent (β). The disk is described according to the power-law steady-state VDD formulation (Sec. 1.4.1). As such, the disk input parameters are the base density $\log n_0$, the radial density exponent n and the disk size R_D . HDUST also takes as input the inclination angle of the system.

As outlined in Mota et al. (2019), we use the HDUST code to create a number of models by varying the input parameters. To run these computationally expensive simulations, we use IAG's cluster Alphacrucis. The grid of models calculated for this work is part of the BeAtlas Be star model grid of the BEACON group, as will be further discussed in Sec. 3.1.

2.3 Bayesian Statistics and Monte Carlo Markov Chain Methods

In recent years, the use of Bayesian-MCMC data analysis in astronomy has grown exponentially. Advances in both engineering and computer science has made MCMC codes, once too computationally (and monetarily) expensive, available to the scientific community at large, leading to a revolution in the way we see data in science. Sharma (2017) is a good review of the Bayesian-MCMC and its use in astrophysics.

Bayesian statistics is a data interpretation theory, and it is not the only one. The most commonly used is frequentist statistics. The difference between the two lies on the way they define what probability is. Frequentist says probability relates to the relative frequency of occurrence of an event, once performed many times. Bayesian definition is closer to what we colloquially use the word for: the measure of the plausibility of a proposition.

Another key difference is that the Bayesian method includes background information on the problem at hand when searching for the probability. If we try to solve the statistical problem of which athlete has a greater chance of winning a match, frequentist approach would say it is a 50%-50% chance for each. The Bayesian approach, however, would take into account that one of the athletes is the current world champion, while the other is a newcomer. Then the victory of the current champion is the most probable outcome.

One of the cases in which using the Bayesian approach is beneficial is for model fitting. If we have hundreds of possible models, how to find the one that best describes the data?

First, the problem must be laid out in Bayesian terms. Bayes's theorem states that

$$p(H|D, I) = \frac{p(D|H, I)p(H|I)}{p(D|I)}, \quad (2.1)$$

where H is the hypothesis made regarding the data, D is the data itself and I is the background information we have on the problem, which is previously known to us. $p(H|D, I)$ is the probability of the hypothesis being correct, given the data and the background information. $p(D|H, I)$ would then be the probability of getting the data given our hypothesis and the background information. $p(H|I)$ is the probability of the hypothesis being correct, considering just the background information. $p(D|I)$ represents what is the data given the background information, which is mainly a normalization factor. Putting the theorem in simpler terms, we could say that

$$\textit{Posterior} = \frac{\textit{Likelihood} \times \textit{Prior}}{\textit{Evidence}}. \quad (2.2)$$

The posterior $p(H|D, I)$ is therefore the result we are looking for: considering the evidence (what we measured), the prior (information previously known) and the likelihood (probability of getting that data given H and the prior), what will be the probability density function of the parameters we are sampling, and what will be the correlation between them? In our case, we have hundreds of models, each described by a set of parameters. The hypothesis H will be our set of parameters that uniquely define a given model.

To solve a problem that has been set up using Bayesian theory is to find $p(H|D, I)$. However, it is not trivial to solve Bayes' theorem for the posterior, so we want to do is to sample points from the distribution in order to characterize it. The go-to solution is to use a Monte Carlo Markov chain implementation. A Monte Carlo method attempts to solve the problem by assigning random values to the parameter set H , and observing the model's behaviour. In a Markov chain Monte Carlo, these numbers will travel along a Markov chain, where, by definition, the next step on the chain depends on the current one.

We use the PYTHON MCMC implementation EMCEE (Foreman-Mackey et al., 2013), which follows the Metropolis-Hastings (MH) algorithm (Metropolis et al. 1953, Hastings 1970). The MH algorithm is the most common implementation of the MCMC method used in astrophysics. In simple terms, MH follows two steps. Consider a chain of random values of the parameter set, H

1. From position x in the chain, sample a proposal position y from a given transition kernel $q(y|x)$
2. Accept the proposal with the acceptance fraction $af(x, y) = \min\left(1, \frac{f(y)q(x|y)}{f(x)q(y|x)}\right)$.

First we propose the algorithm go from position x in the chain to position y , the transition $q(y|x)$. $q(y|x)$ is an easy-to-sample probability distribution, such as a Gaussian centred on the initial position x . The second step in MH determines if going from x to y is a smart choice or not. For that, it has to consider what the likelihood and priors (function f) of each position are, and then compare them. If $f(y)q(x|y)$ is greater than $f(x)q(y|x)$, that is, if the model proposed at point y has a better likelihood than the model at point x , position y is always accepted as the next step in the Markov chain. If it is not, there is a non-null probability that it will move to y anyway: this makes it possible for the chain to escape local minima and sample the whole parameter space. This is called the acceptance fraction, af . On the other hand, y can be rejected as the next position, in which case the chain will remain on x and the process will be repeated. As this process is repeated many times ($N \rightarrow \infty$), an stationary state is reached as MH converges.

EMCEE is an ensemble MCMC algorithm. This means it does not consider a single Markov chain, which would take a very long time to find the stationary state, but multiple chains where the next step in each chain depends on the present position of each member of the ensemble. This characteristic is translated in the code by the walkers variable, a number chosen by the user (usually a few hundreds), that determines how many “Markov chains” the code will use to sample the problem given (Goodman and Weare, 2010). The actual implementation of EMCEE is much more robust, as can be read in the original work Foreman-Mackey et al. (2013).

The great advantage of using Bayesian-MCMC methods instead of obtaining just the best fit model, as we would from the frequentist approach, is that here we find a distinct probability density function for each of the parameters, and the correlations between them. This gives us more insight into the characteristics of the star, and an overall more robust inference.

Methodology

This chapter outlines the methodology of our work. Our goal is to use HDUST models combined with a MCMC code to find the PDFs of the main parameters that describe a Be star: mass, rotation rate, age, disk base density, disk radial density exponent, disk radius, inclination of the system, distance and extinction $E(B - V)$. The model grid is fed to the MCMC code along with the data of the star and any prior information available, and returns the PDFs and correlations for all the parameters.

We describe the BeAtlas model grid in Sec. 3.1 and the MCMC code developed to infer the parameters in Sec. 3.2.

3.1 *BeAtlas Grid*

Calculating a Be star grid of models is a time consuming effort. For past works such as Klement et al. (2015), choosing which parameters to use to create models was important so that only the necessary was calculated, but it could still take months to create a good enough grid. Also, a manual search in a multidimensional parameter space is not guaranteed to find the best solution. The idea for BeAtlas was to create an universal grid for Be stars, covering all possible parameters such a star could have. In this way, no new tailor made grid would have to be calculated for new projects, as they should all the be included in BeAtlas.

BeAtlas was the main focus of B. Mota's PhD thesis (Mota, 2019), where it is described and tested in great detail. Here we present some aspects that are relevant to this particular work. BeAtlas is divided in two subgrids: the purely photospheric and the disk grid. The photospheric grid is simpler, as it does not include the disk, only the rapid rotating central

Be star. The disk grid includes the disk in the simulations, and is therefore much larger and takes a much longer time to calculate even a single model.

As stated in Sec. 2.2, HDUST takes as input the stellar parameters, the stellar mass (M), pole radius (R_{pole}), rotation rate (W), luminosity (L) and gravity darkening exponent (β). Five parameters may not seem like a lot, but when creating a grid of models, the number of each of them has to be multiplied by the others to correctly close the grid. If we had 5 values for each of the parameters, in the end we would need $5^5 = 3125$ models. Thus, reducing the number of free parameters was in our interest.

To do so, we investigate the existence of correlations between the parameters in such a way that, by choosing a value to one of them, another is also constrained. The exponent β is the simpler to correlate: Espinosa Lara and Rieutord (2011)'s formulation present it as a function of W . To connect R_{pole} and L to M and W , we make use of the evolutionary models of rotating stars created by the Geneva group (Ekström et al., 2008; Georgy et al., 2013; Granada et al., 2013).

The Geneva models compute the stellar structure and evolution from the MS up to the end of carbon burning for massive stars, the early asymptotic giant branch phase for intermediate-mass stars. Their models cover the mass range from 1.7 to 15 M_{\odot} , and was expanded up to 20 M_{\odot} specially for the BeAtlas project by collaborator C. Georgy. It also covers rotation rates from 0 to 1 (critical). With these models, we can relate R_{pole} and the luminosity of the star to the mass and rotation rate if we also consider the X_c parameter: the fraction of H in the stellar core. X_c , on the other hand, is connected via these models with the age of the star, its main sequence age, t/t_{MS} , expressed as the fraction between the age and the theoretical lifetime in the main sequence t_{MS} (see Fig. 3.1). Therefore, with the Geneva models we can describe basically any Be star using just three parameters: M , W , and t/t_{MS} . Another parameter that is relevant but was not included in our grid was the metallicity, which influences the stellar evolution and therefore the stellar parameters. In our grid it is fixed at $Z = 0.014$.

The disk model computation in HDUST follows the steady-state power-law VDD formulation as in Eq. 1.13. The code takes as input three parameters: the base density ρ_0 , the radial exponent n and the disk truncation radius R_d .

When this project started, the BeAtlas grid was still being planned, and only partially computed. Therefore, over the course of my undergrad research project and later MSc we

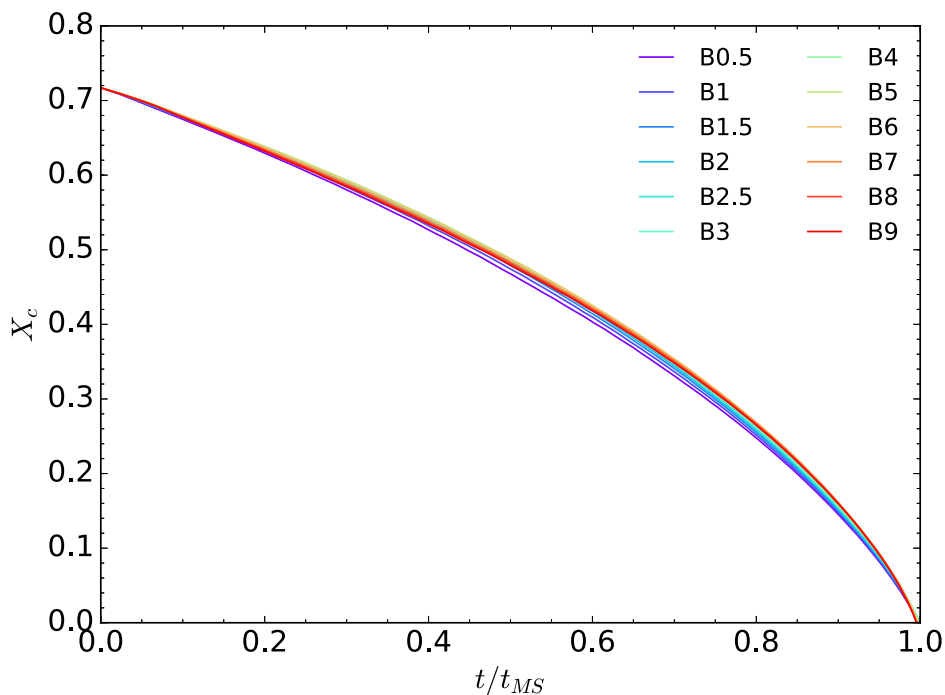


Figure 3.1: X_c relation with stellar age t/t_{MS} , for many spectral types.

calculated a subgrid of BeAtlas specifically tailored for α Col. As the project developed into the Bayesian analysis we present here, the grid became rather massive, as it was updated and expanded several times as it became necessary. Table 3.1 shows the parameters and their ranges in the disk grid used for most of this work.

In its final form, the grid was comprised of 21600 models, all computed using the Alphacrucis cluster at IAG-USP, without which the BeAtlas project could never come to fruition. Each model is calculated in parts, as to increase the efficiency of the process. We break the SED into spectral ranges, each defining a different band in HDUST. The grid for α Col was divided according to Table 3.2, and later concatenated into the final form.

3.2 BEMCEE Package

Without a sampler, however, the grid has no purpose. The Bayesian-MCMC theory used in this work was described in Sec. 2.3, but here we explain the implementation of the EMCEE package to our situation, and the creation of the PYTHON package BEMCEE.

Parameters	Values
M	3.00, 3.80, 4.40, 4.90, 6.00 M_{\odot}
R_{eq}/R_{pole}	1.20, 1.30, 1.45
X_c	0.0, 0.1, 0.3, 0.5, 0.7
$\log n_0$	11, 11.5, 12, 12.5 cm^{-3}
ρ_0	9.9×10^{-13} , 3.1×10^{-12} , 9.9×10^{-12} , 3.1×10^{-11} g cm^{-3}
n	2.0, 2.5, 3.0
R_d	10, 20, 30, 40, 50, 60 R_{eq}
i	20, 30, 40, 50°

Table 3.1 - Parameters used to create the grid. The fraction of H in the core of the star X_c corresponds to the time of life of the star in the Main Sequence, t/t_{MS} . Parameter n_0 is the actual input value required by HDUST, but its more physically interesting counterpart ρ_0 is the one used to discuss the results.

Observable	λ min [μm]	λ max [μm]
UV	.115	.35
VISIBLE	.35	1
NIR	1	5
NIR2	5	12.5
IR	13.0	100
MM	860	880
SUBMM	100	1000
UP1	19990	20010
UP2	34990	35010
UP3	62990	63010
CM07	6000	7500
CM13	11300	16700
CM20	16700	25000
CM30	25000	37500
CM60	37500	75000
CM100	75000	110000

Table 3.2 - Band definitions for the grid.

3.2.1 Posterior sampling

By itself, EMCEE implements MCMC, but requires further instructions and definitions to actually produce the results. It is up to the user to create the prior and likelihood functions that make sense for their work. BEMCEE, the complete package that carries out the MCMC inference for Be stars using the BeAtlas grid, was build by mainly by group members B. Mota and R. Vieira, with my assistance as well.

In Sec. 2.3, we say, in order to simplify Bayes's theorem, that the probability of getting the data D given our model H , $p(D|H)$, is the likelihood. In fact, the likelihood is a function *proportional* to $p(D|H)$. The likelihood does the reverse of the probability $p(D|H)$: $L(H|D)$ asks what is the probability of model H being correct given the data D . Therefore,

$$L(H|D) = k p(D|H), \quad (3.1)$$

where k is a positive constant.

The general expression for the likelihood of n independent measurements given a set of parameters θ is

$$L(\theta|x_1, x_2, \dots, x_n) = \prod_{i=1}^n p(x_i|\theta). \quad (3.2)$$

It is useful to find instead the logarithmic function of the likelihood, where this product turns to a sum

$$\ln L(\theta|x_1, x_2, \dots, x_n) = \sum_{i=1}^n \ln p(x_i|\theta). \quad (3.3)$$

For a set of independent points with independent errors, the most common function to use for the distribution $p(x_i|\theta)$ is

$$\ln p(x_i|\theta) = \frac{(D(x_i) - f(x_i|\theta))^2}{2\sigma_i^2}, \quad (3.4)$$

where our data points are $D(x_i)$ with error σ_i and the model built from a set of parameters θ is $f(x_i|\theta)$. This follows from the central limit theorem, that dictates that when we sum independent random variables with independent errors, the end results tends to a normal distribution. In BEMCEE, we use the logarithm of the data, model and errors, as the range in wavelength (from the UV to the radio) and in flux of the SED (spanning ~ 12 orders of magnitude) is very large. For all n samples of data points $D(x)$, with an error σ and a

model $f(x|\theta)$, the function becomes the sum of the square errors, as

$$\chi^2 = \sum_{i=1}^n \frac{(\ln D(x_i) - \ln f(x_i|\theta))^2}{2 \ln \sigma_i^2}. \quad (3.5)$$

Finally, the log of the likelihood for the model with parameters θ given the data points x_i is

$$\ln L(\theta|x_i) = \ln(k) - 0.5\chi^2. \quad (3.6)$$

This is how we define the likelihood in BEMCEE

BEMCEE also takes into account the priors, information we already have on the data. If we have reliable measurements on certain parameters of the Be star, our inference of the rest of them can only improve, if used correctly. We decided to use as priors the information on stellar parallax and $v \sin(i)$. The idea of the priors is to constrain the parameters related to them.

In Bayesian theory, the prior function can, in principle, take whatever form we choose. It can have flat, or step form, which is what we implicitly do when defining ranges for the parameters in our models. Since we are setting as prior two measurements with their respective errors, we chose to set it as a Gaussian with peak value and variance taken from the published values. The form they take, therefore, is simply

$$\chi_a^2 = \frac{(a - a_{model})^2}{\sigma_a^2}, \quad (3.7)$$

where a is the measured value, a_{model} the model estimate, and σ_a the uncertainty on the measurement. Since we have more than one prior $p(\theta|a)$, they are summed in a similar fashion to the likelihood, giving

$$\ln p(\theta|a_i) = -0.5 \sum_{i=1}^n p(\theta|a_i) = -0.5 \sum_{i=1}^n \chi_{a_i}^2, \quad (3.8)$$

We also developed a way to use as prior not a simple Gaussian, but a more complex distribution. For instance, if we have a previously determined PDF of a given parameter and wish to use it as prior for the next MCMC inference, it can be done with BEMCEE. What we do is save the PDF (which a huge array of all values sampled for that parameter during the MCMC inference) after a run and fed it back to the code for a second run. The code reads this and computes a Kernel density estimation (KDE) of the PDFs, which is a smooth function (see Fig. 3.2). With this KDE distribution K at hand, we can compare

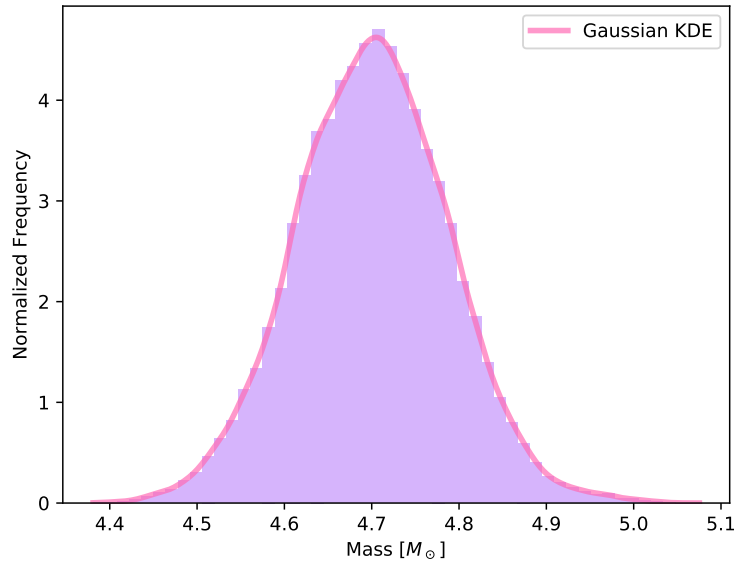


Figure 3.2: The difference of using KDE or histogram for the same data. The line represents the KDE calculated a Gaussian kernel for the histogram of the mass of the star.

the suggested value of the parameter for the current from with the previous distribution.

This KDE prior has the form

$$\chi_b^2 = \frac{1}{K(b)}. \quad (3.9)$$

As before, if there is more than one such prior, the total will be as Eq. 3.8. One note is that this type of prior is only used in certain occasions, as will be explained in our results in Sec. 4.1.

Since now we have the likelihood and the prior, we can go back to Bayes's theorem to calculate the logarithm of the posterior distribution

$$\ln P(\theta|x_i) = \ln L(\theta|x_i) + \ln p(\theta). \quad (3.10)$$

For each set of parameters θ we propose to the code, we will have a posterior. If we compare the posteriors of two models with parameters θ and θ_0 , we have

$$\frac{\frac{P(x|\theta)P(\theta)}{P(x)}}{\frac{P(x|\theta_0)P(\theta_0)}{P(x)}} = \frac{P(x|\theta)P(\theta)}{P(x|\theta_0)P(\theta_0)} = \frac{P(\theta|x)}{P(\theta_0|x)}. \quad (3.11)$$

The evidence term in the theorem in Eq. 2.1, being a multiplicative constant, is cut out when this comparison is done, as well as the constant k from Eq. 3.1. The relation $\frac{P(\theta|x)}{P(\theta_0|x)}$ should be familiar: the acceptance of a step on the MH algorithm depends on the posterior

function (called f for simplification) of the two positions x and y as

$$af(x, y) = \min \left(1, \frac{f(y)q(x|y)}{f(x)q(y|x)} \right). \quad (3.12)$$

The relation $f(y)/f(x)$ is exactly what we sample.

3.2.2 Structure

BEMCEE has the following input files:

- SED data in `xml` format
- Polarization data in `csv` format
- Table with additional information on the star (used for the priors) in `txt`
- BeAtlas model grid in `xdr` format

In the main initialization file in the package, the user must set the following parameters:

- a parameter
- Include R_V as a free parameter or choose a fixed value for it
- Number of walkers, number of steps, and burn-in
- KDE priors
- Wavelength range

The a parameter is an internal EMCEE parameter related to the transition distribution q , that deals with the size of the step between two suggested positions. Foreman-Mackey et al. (2013) advise we keep this value to set to 2, but it can be changed depending on the necessity. The reason for this is that the acceptance fraction af depends on a . If af goes either too low or too high (its range is 0 to 1), it indicates there is a problem with the setup of EMCEE. If af is 0, then all proposed steps are rejected, so we would just be sampling the same position over and over. On the other hand, if af is 1, all steps are being accepted with no regard for their likelihood, and therefore the posterior would be meaningless. The optimum range for af according to Foreman-Mackey et al. is between 0.2 and 0.5, but it is preferable if it is closer to 0.234 (Gelman et al., 1996; Hogg and Foreman-Mackey,

2018). It may the case to tinker with a if it drops a bit below 0.2 or above 0.5. If the case is extreme (e.g., $af = 0$), then it is likely a structural problem on the implementation, or a gross mistake in the input parameters and/or observational data.

The parameters sampled by BEMCEE for a Be star are 9: mass, rotation rate, age, base density of the disk, radial density exponent, disk radius, inclination, distance and $E(B - V)$. However, one can choose to make it 10 by adding R_V , that relates to $E(B - V)$ as $R_V = A_V/E(B - V)$. The user has the option of allowing it to vary or keeping it to either the standard value of 3.1 or another value, should an estimate from the literature be available.

From the 9 parameters, only 7 are model parameters intrinsic to the star (see Tab. 3.1). Distance and $E(B - V)$ are implemented internally in the BEMCEE code. The distance is added when we calculate the normalization¹ of the model flux, multiplying the flux by $(10/d)^2$. The $E(B - V)$ is accounted for when we redden the model using the PYTHON PYASTRONOMY² package `unred` function. It uses the Fitzpatrick and Massa (1999) prescription for the interstellar extinction.

Two very important parameters in EMCEE are the number of walkers and the number of steps in each run. Since it is an ensemble sampler, EMCEE has the advantage of setting many concurrent chains at once, all working together to sample the distribution. The number of Markov chains is what we will refer to as the number of walkers in the run. Foreman-Mackey et al. (2013) advise to use hundreds of walkers. The number of steps defines the maximum number of steps each walker will take during the run. The burn-in phase of the sampling is an initialization of the procedure, usually set to 10% of the total number of steps. These burn-in steps are discarded from the chain to calculate the final PDF.

The user can also choose whether or not to use chains calculated by previous runs as input for the current run. If set to ‘True’, the code will use as prior the KDE of the mass, rotation rate and age of the star as found by a previous run. This is particularly useful for when we study the polarization of the star, as will be discussed in Sec. 4.1. Otherwise, it is set to ‘False’.

The wavelength range defines which parts of the SED will be probed by the code. Thus,

¹ BeAtlas fluxes are normalized for a star 10pc away

² <https://www.hs.uni-hamburg.de/DE/Ins/Per/Czesla/PyA/PyA/index.html>

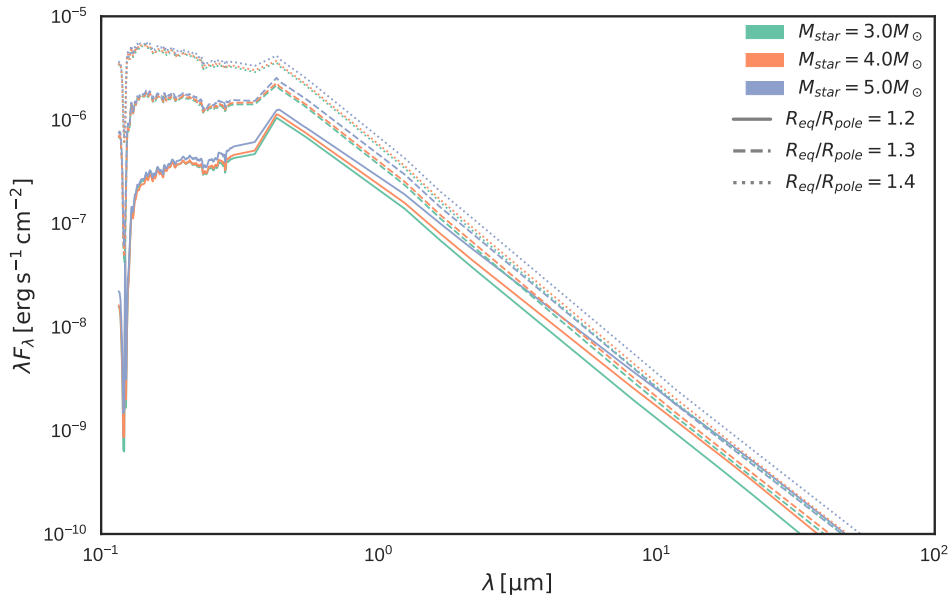


Figure 3.3: Effects on the flux caused by changing the stellar parameters while maintaining the same disk, from the UV to 1 μm .

it is possible to ‘cut’ the SED in sections and analyse them independently, with interesting results. The sections are defined in Table 3.3. In the polarization setup, this parameter is not used. The reason for the region definitions comes from our understanding of Be star emission: the UV light comes mainly from the central hot B star, while flux in IR and longer wavelengths come mostly from the disk. The star and disk emission, although obviously interconnected, have more weight in shorter and longer wavelengths respectively. As such, we expect the UV region to provide a lot of information on the stellar parameters, and be blind to the disk, while the centimetre observations probe the outermost disk, and say next to nothing on the central star. This is shown in Figs. 3.3 and 3.4.

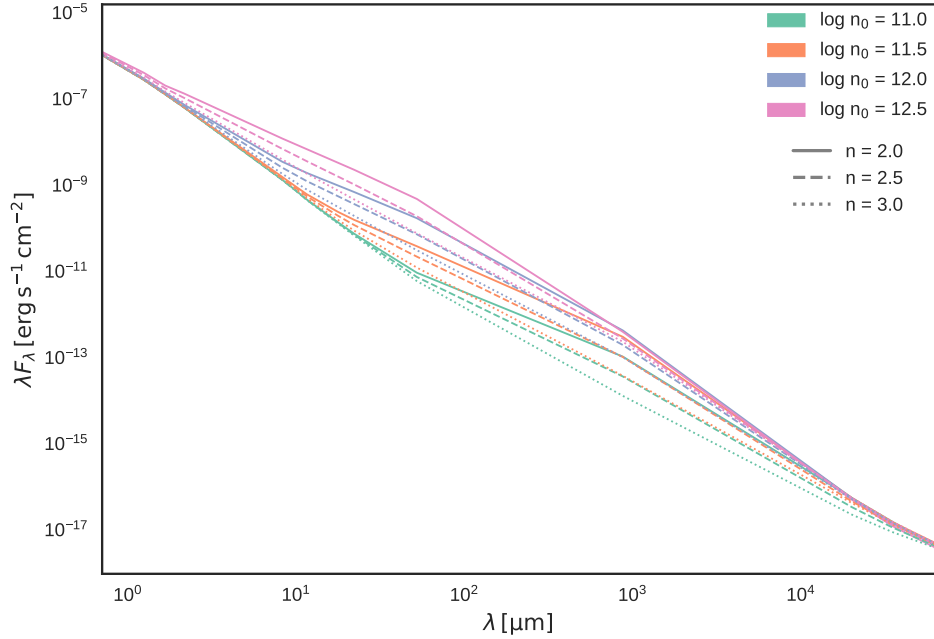


Figure 3.4: Effects on the flux caused by changing the disk parameters while maintaining the same central star, from the near-infrared ($0.7 \mu\text{m}$) to 6.3 cm .

Region	Wavelengths (μm)
UV	0.1 to $0.3 \mu\text{m}$
UV+VIS	0.1 to $0.7 \mu\text{m}$
UV+VIS+NIR	0.1 to $5.0 \mu\text{m}$
UV+VIS+NIR+MIR	0.1 to $40.0 \mu\text{m}$
UV+VIS+NIR+MIR+FIR	0.1 to $350. \mu\text{m}$
UV+VIS+NIR+MIR+FIR+MICROW+RADIO	0.1 to $63000 \mu\text{m}$
VIS+NIR+MIR+FIR+MICROW+RADIO	0.39 to $63000 \mu\text{m}$
NIR+MIR+FIR+MICROW+RADIO	0.7 to $63000 \mu\text{m}$
MIR+FIR+MICROW+RADIO	5.0 to $63000 \mu\text{m}$
FIR+MICROW+RADIO	40.0 to $63000 \mu\text{m}$

Table 3.3 - “Cut” regions defined in our analysis.

The results from BEMCEE consist in PDFs, correlation maps, and trace plots. The main figure output is a triangular or corner plot. An example corner plot is shown in Fig. 3.5. In the example, we have three parameters: x , y , and $\log(a)$. The PDF for each parameter is shown in the main diagonal of the plot as a histogram, while the intersection between a column and a row parameter gives their respective correlation map. The sharpness of

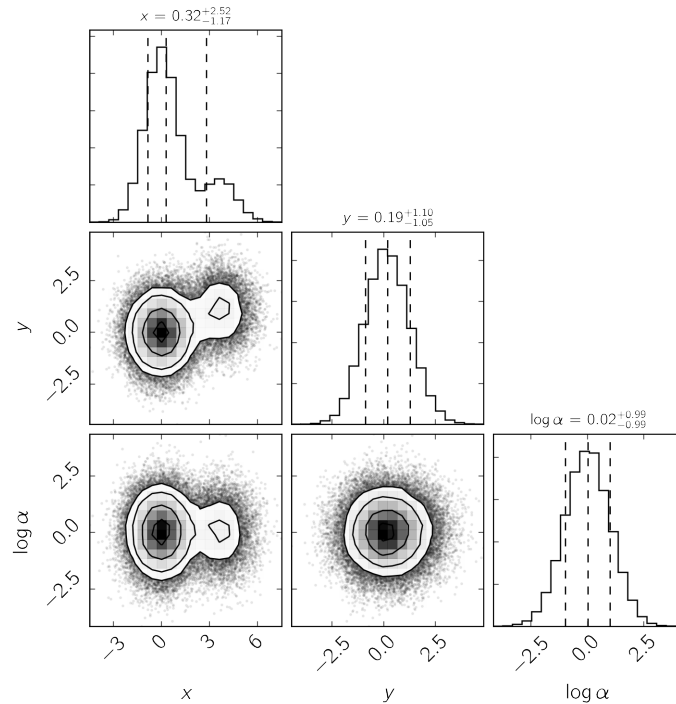


Figure 3.5: Example of a corner plot. Image from www.corner.readthedocs.io/en/latest/pages/quickstart.html

the PDF is an indicator of how well the parameter was constrained by the code. A flat PDF tells us there was not enough information for the MCMC inference to actually choose the more likely parameter: choosing different numbers for it amounted to no significant change in the model, and therefore the likelihood was so similar in the entire space that the walkers never converged to a estimate. The ideal is for the PDF to have a clear peak and fall to zero on both sides as it distances itself from the peak. Another output of the code is the trace plots, that show the path of each walker through parameter space throughout the entire run for each parameter evaluated. The last output is the chord diagram, a visualization tool that helps us see the correlations between the parameters in a clearer fashion.

With our methodology explained, we go now to our results in the following chapter.

Results

In this chapter we present the results of the multi-technique work done during my MSc. We first analyse each observable separately, in order to study which parameters they constrain and how differently they behave. We expect, for instance, that the polarization will not offer great insight into the stellar parameters, as it comes from scattering off the disk. It will, on the other hand, constrain the inclination of the system, of which it greatly depends. The SED, since it covers a large range of wavelengths, is also divided in sections and first analysed separately, as shown in Table 3.3. The prior on $v \sin(i)$ is set as a normal distribution around the value found by Frémat et al. (2005) of $192 \pm 12 \text{ km s}^{-1}$. The distance (parallax) prior is similarly set around the Hipparcos¹ determination of $12.48 \pm 0.36 \text{ mas}$. We opted for the Hipparcos (van Leeuwen, 2007) determination over the more recent Gaia data release 2 (Gaia Collaboration et al., 2017) for the same reasons explained in Mota (2019): Gaia DR2 and Hipparcos disagree well above the nominal uncertainties for $\alpha \text{ Col}$. DR2 also has several issues for bright and nearby sources, most notably the ones that are in binary systems.

4.1 SED

The results for the fitting of each SED cut are shown in Figs 4.1 to 4.10, the corner plots obtained from BEMCEE for each of the cuts defined in Table 3.3. Their respective trace plots are shown in Appendix B.

The analysis covering only the UV region of the SED (Fig. 4.1) immediately gives a very sharp PDF for the mass of the star, age, and $E(B - V)$. As previously discussed,

¹ <http://cdsarc.u-strasbg.fr/viz-bin/cat/I/311>

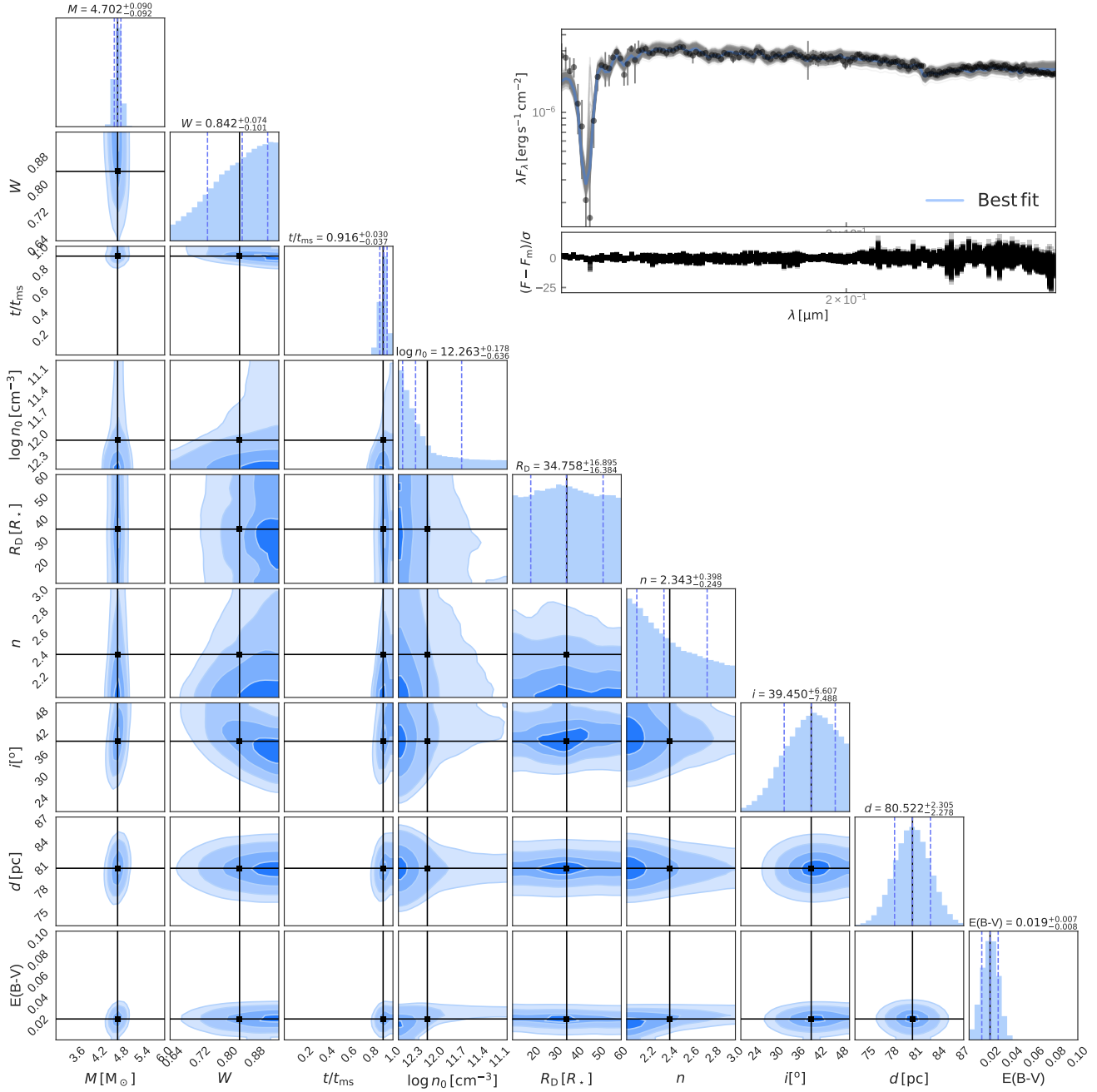


Figure 4.1: Corner plot for the UV region of the SED, with 300 walkers and 20000 steps, $af = 0.24$.

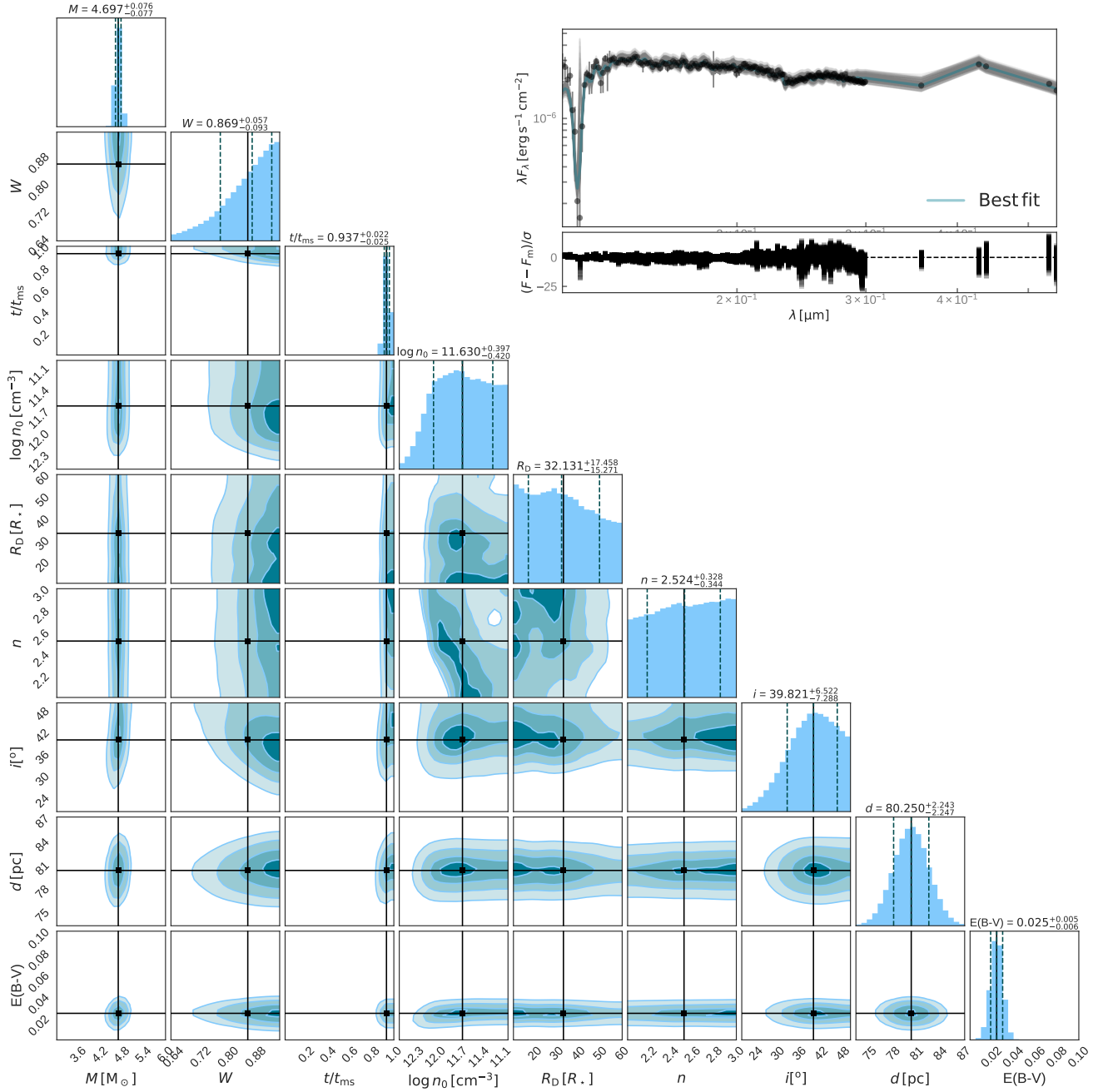


Figure 4.2: Corner plot for the UV+VIS region of the SED, with 300 walkers and 20000 steps, $af = 0.26$.

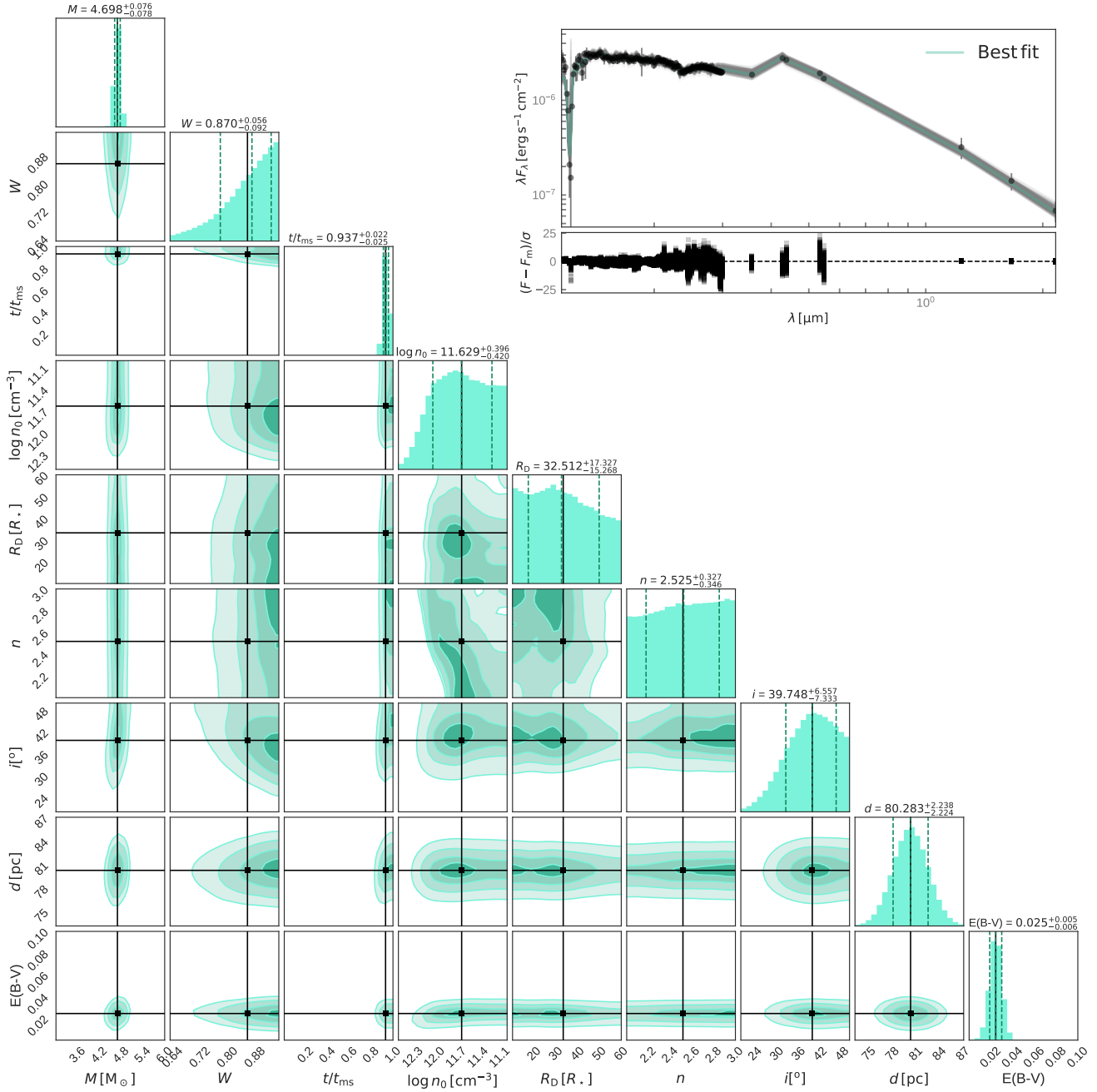


Figure 4.3: Corner plot for the UV+VIS+NIR region of the SED, with 300 walkers and 20000 steps, $af = 0.26$.

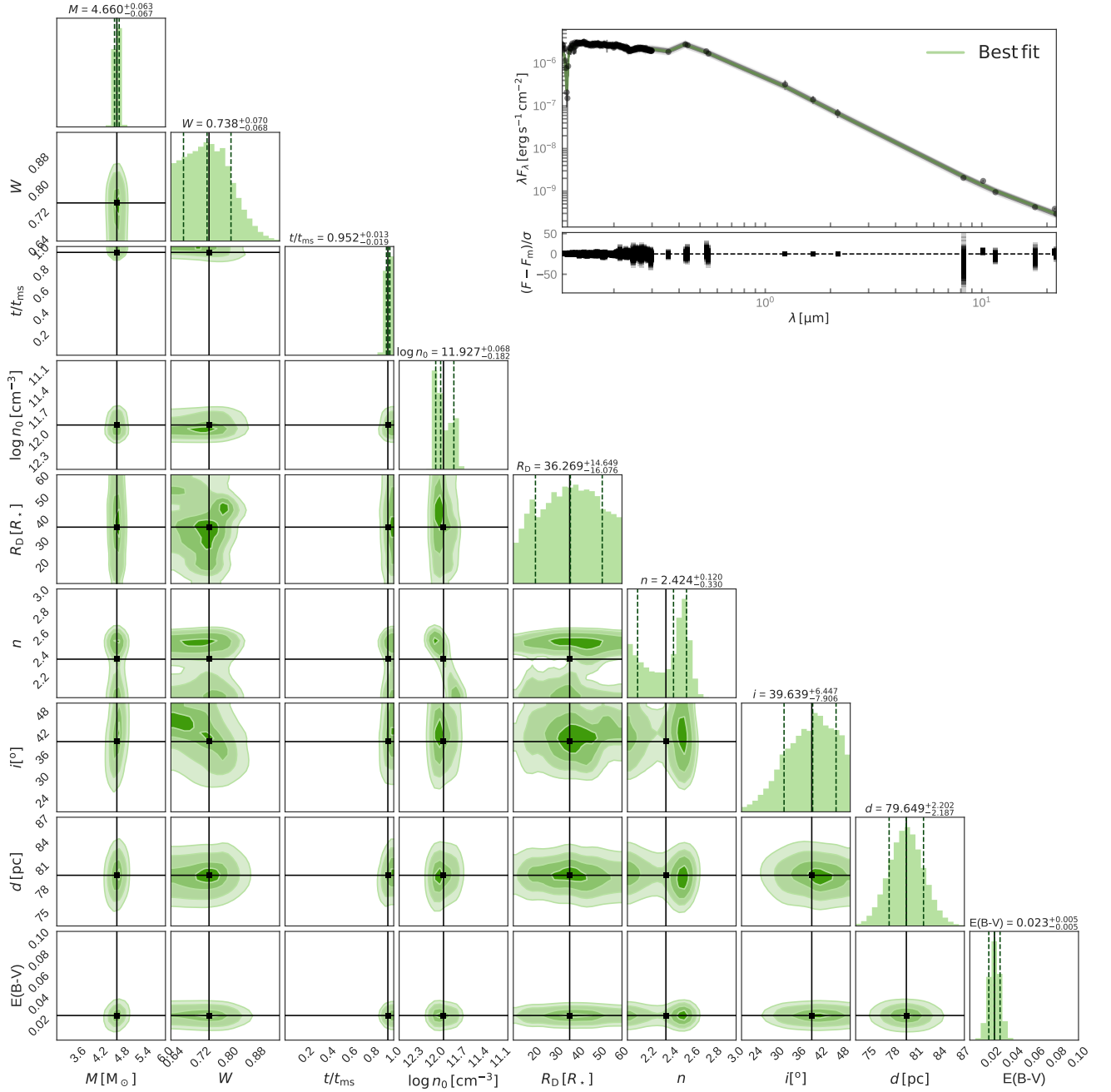


Figure 4.4: Corner plot for the UV+VIS+NIR+MIR region of the SED, with 300 walkers and 20000 steps, $af = 0.21$.

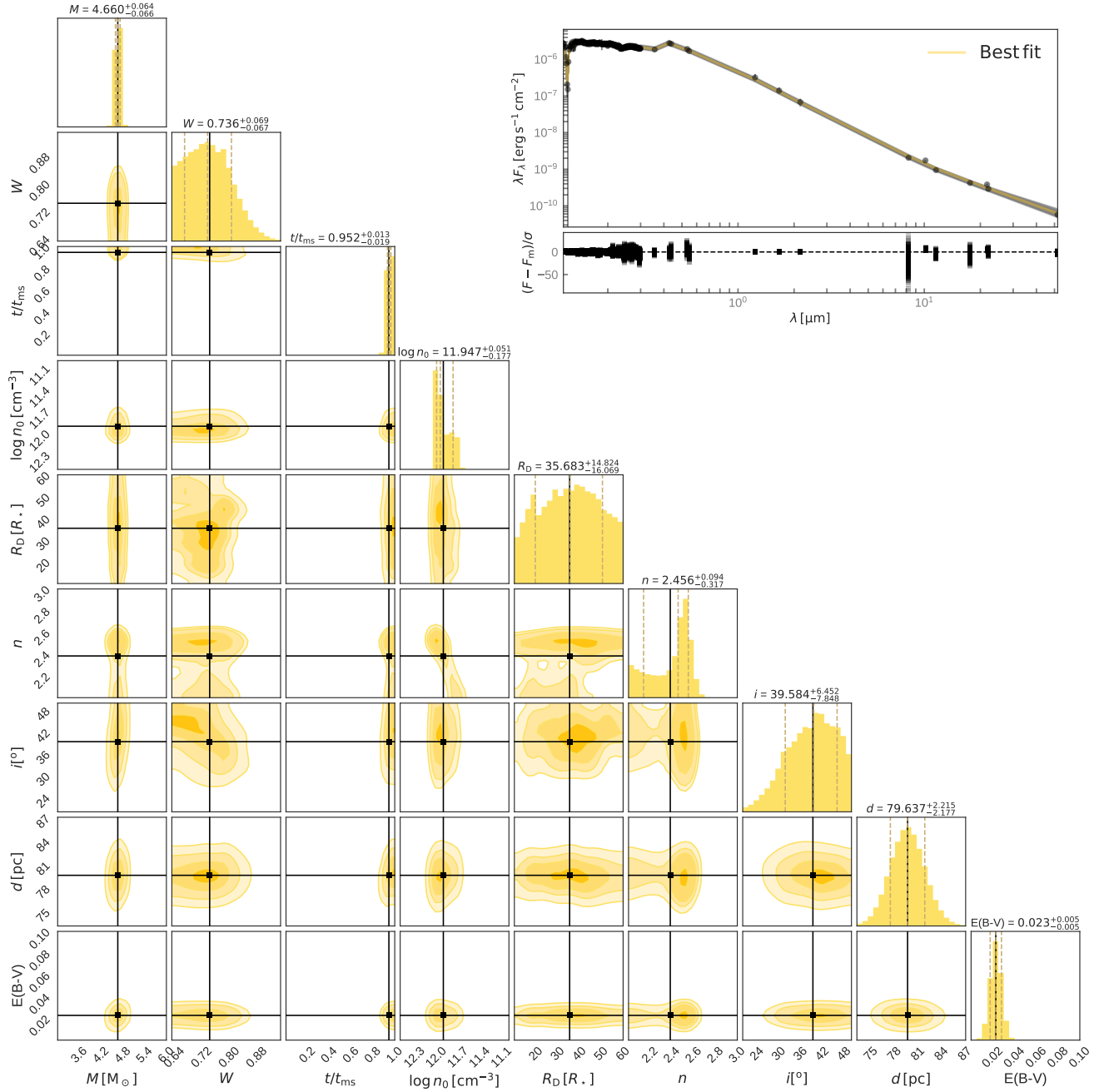


Figure 4.5: Corner plot for the UV+VIS+NIR+MIR+FIR region of the SED, with 300 walkers and 20000 steps, $af = 0.22$.

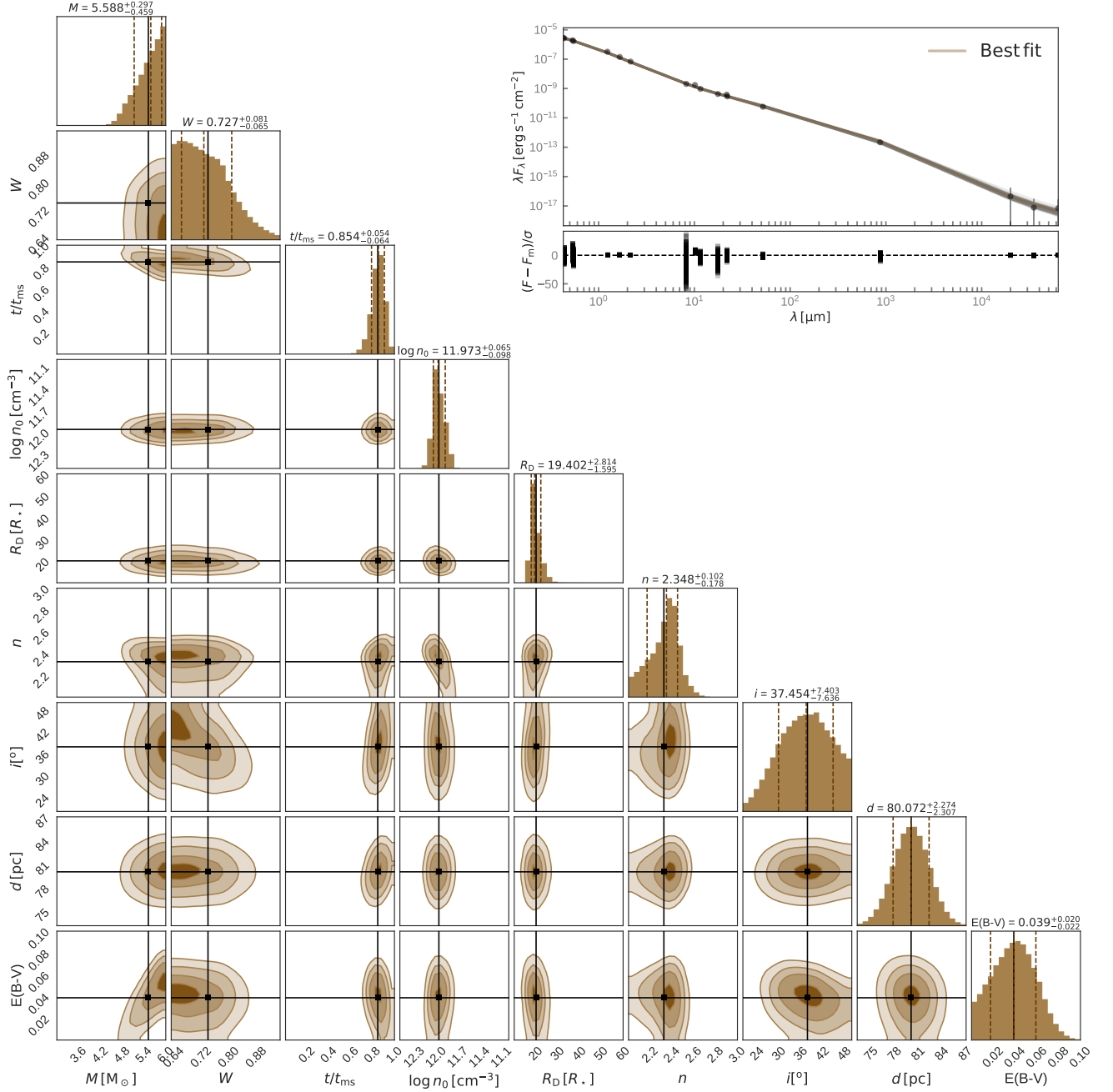


Figure 4.6: Corner plot for the VIS+NIR+MIR+FIR+MICROW+RADIO region of the SED, with 300 walkers and 20000 steps, $af = 0.22$.

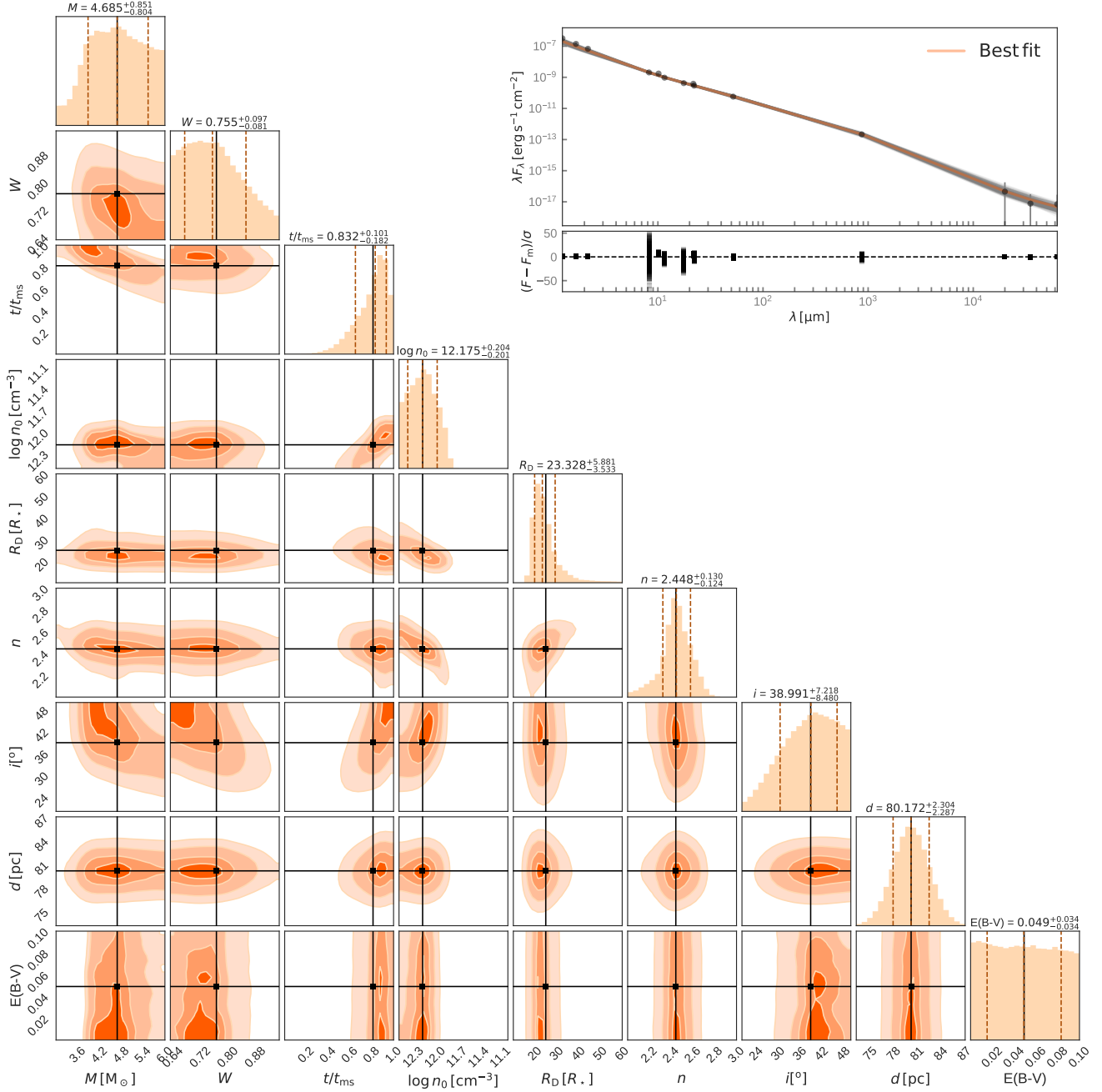


Figure 4.7: Corner plot for the NIR+MIR+FIR+MICROW+RADIO region of the SED, with 300 walkers and 20000 steps, $af = 0.22$.

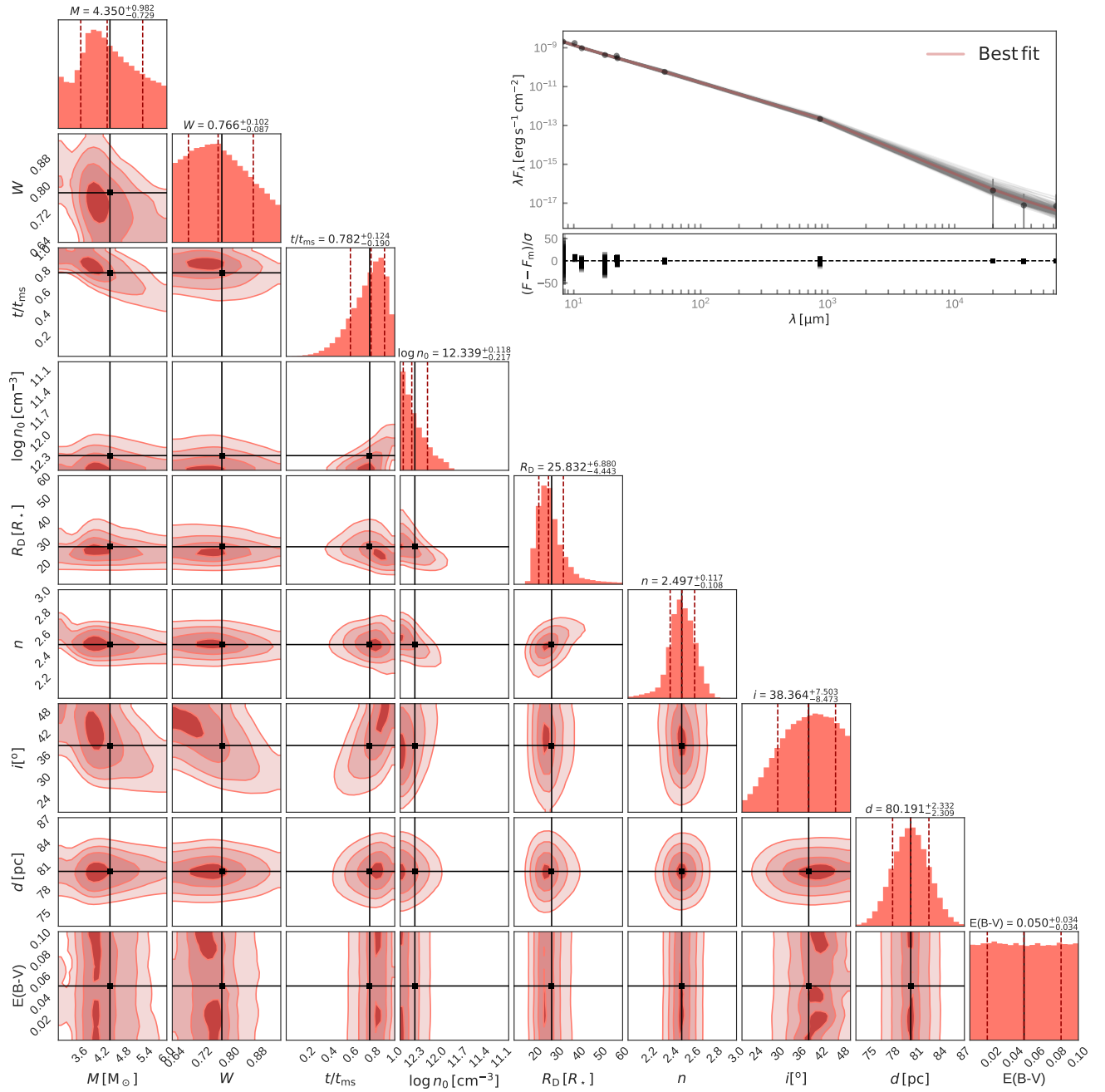


Figure 4.8: Corner plot for the MIR+FIR+MICROW+RADIO region of the SED, with 300 walkers and 20000 steps, $af = 0.22$.

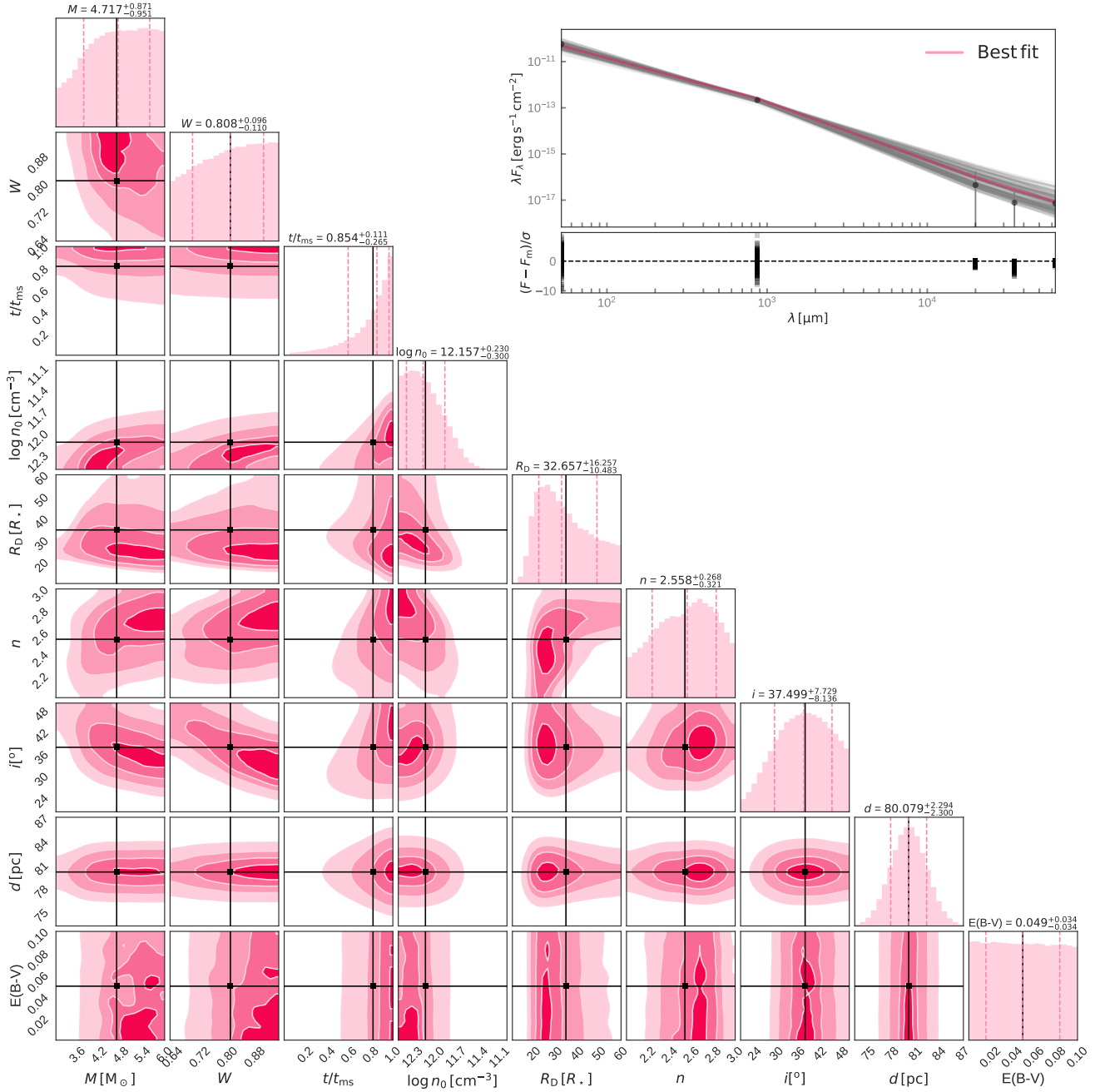


Figure 4.9: Corner plot for the FIR+MICROW+RADIO region of the SED, with 300 walkers and 20000 steps, $af = 0.22$.

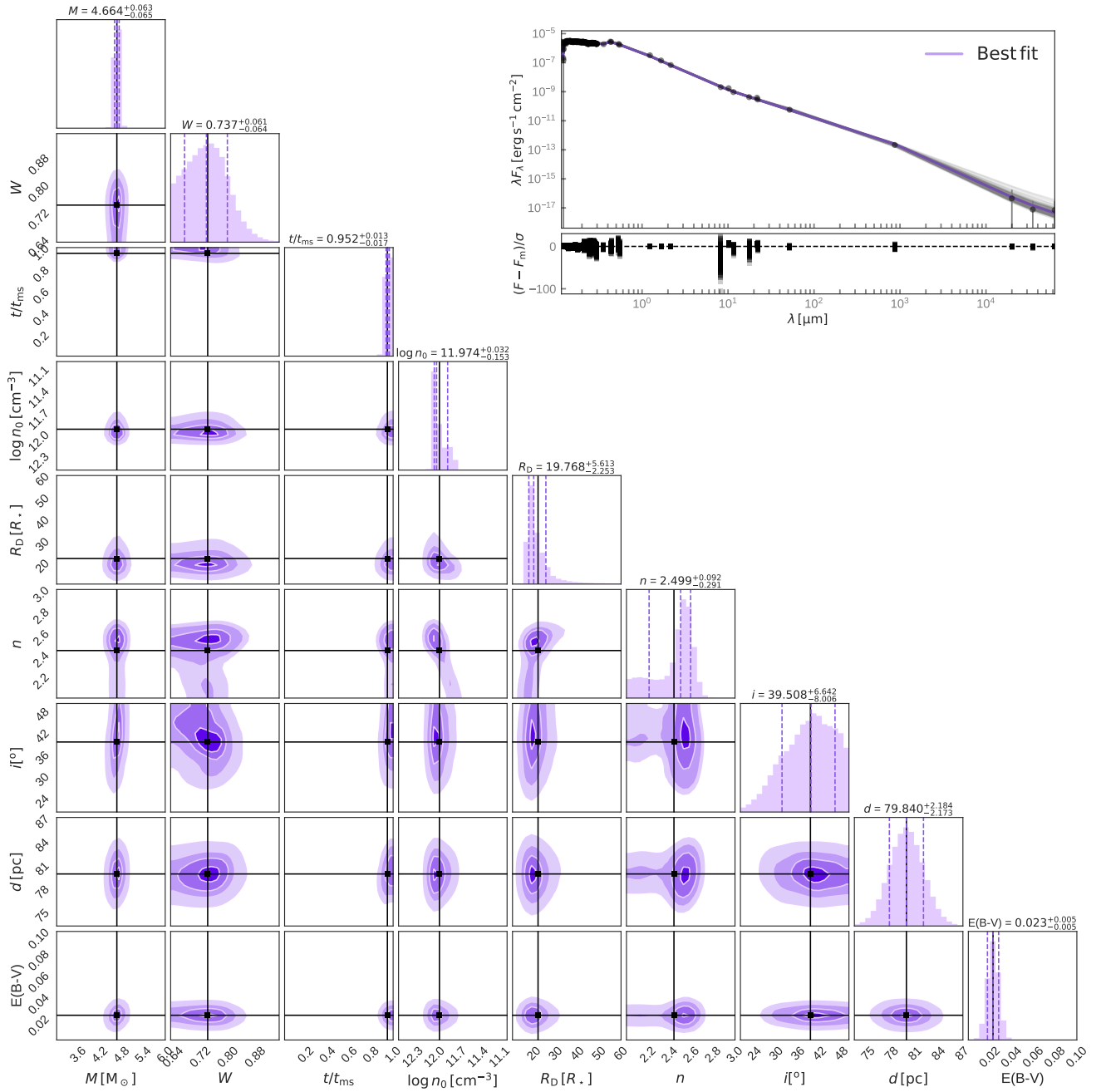


Figure 4.10: Corner plot for the entire SED, with 300 walkers and 20000 steps, $a_f = 0.22$.

the light in the UV comes mainly from the central star. For B stars in general, the peak of the photospheric emission is at the UV region; for α Col in particular, if we take the estimate of the effective temperature given by Zorec and Royer (2012) of 11830 K, the peak emission should be at around $0.25 \mu\text{m}$. Therefore, this particular part of the SED is very susceptible to changes in the stellar mass and age (see Fig. 4.11).

The mass is remarkably well constrained at $4.70_{-0.09}^{+0.09} M_{\odot}$, inside the uncertainty range of Levenhagen and Leister (2006) and Zorec et al. (2016) (see Tab. A.1). A word of caution is necessary, though, to interpret the mass result. The mass is notably a difficult parameter to determine in stars in general, and by far the best method for its determination is binary studies, in particular visual binaries for which all orbital elements can be determined. A 2% accuracy in the mass corresponds to a very good result in binary studies. The mass we determine in our modeling is more properly referred to as a "theoretical" mass, as it depends strongly on the underlying evolutionary model. A comparison between a value thus determined, and a direct determination (if possible) would prove invaluable for testing stellar evolution theories.

Contrary to the mass, whose PDF fits comfortably in the parameter range, the PDF for the age is piled up in the maximum limit for the age. Usually in this case we would increase the grid in that direction, but t/t_{MS} cannot be set to values larger than 1 (that is, the very end of the MS) in the current version of BeAtlas, which tacitly assumes that Be stars are MS objects. Our result indicates that α Col is at the very end of its main sequence life time with $t/t_{\text{MS}} = 0.916_{-0.03}^{+0.03}$, that matches the previous determination of Zorec et al. (2016), which puts it at 0.97 ± 0.06 , and Levenhagen and Leister (2006) at 0.91.

The absorption feature centered at $217.5 \mu\text{m}$, the "UV bump", is closely related to the $E(B - V)$ of the star (Dougherty et al., 1994). Therefore, it follows that this region of the SED would be more sensitive to this parameter (Mota, 2019). It sits comfortably at $0.019_{-0.009}^{+0.007}$, in accordance to Zorec et al. (2016) determination of 0.019 ± 0.017 . Also, as expected, the disk parameters n , $\log n_0$ and R_D are not constrained at all by the UV data.

Fig. 4.2 adds the visible Johnson and TYCHO photometry to the analysis, but the change in the estimates is small. The disk is still unconstrained and the star remains the same inside the uncertainty range. The same is true for Fig. 4.3, that includes the near-infrared photometry of 2MASS. The above results already allow us to conclude that

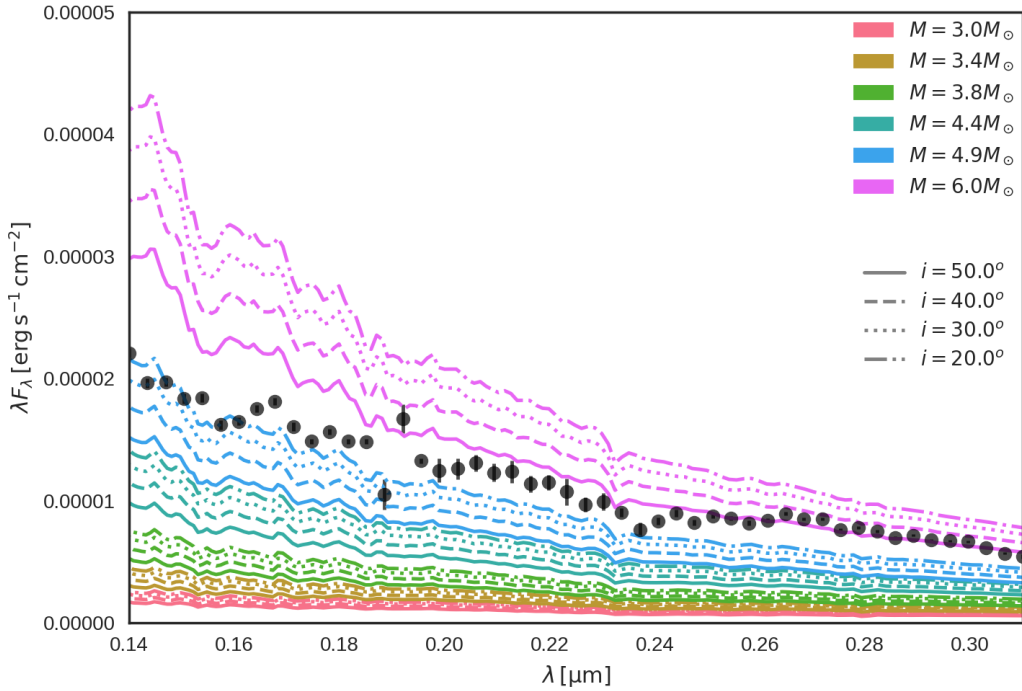


Figure 4.11: Behaviour of the models when we vary mass and inclination in the UV region. In black is our IUE spectra, binned, for reference.

the disk around α Col is probably very tenuous, as no, or very little, excess emission is present at these wavelengths.

Dramatic change happens when we finally add the mid-infrared data (Fig. 4.4), the region where the presence of the disk leads to a noticeable flux excess. The base density $\log n_0$ is now constrained to $11.93^{+0.03}_{-0.18}$, or $8.4 \times 10^{-13} \text{ g cm}^{-3}$, while the radial density exponent settles around $2.42^{+0.12}_{-0.33}$. Adding the far-infrared (Fig. 4.5) cleans up the left tail of the n PDF, but the results are otherwise the same. It is interesting to note that even in the far infrared, the outermost part of the disk is still not well probed, as the nearly flat PDF for the disk radius indicates.

In Fig. 4.6, we include the microwave and radio regions to the analysis, but remove the UV region. The effect on the parameters is huge: while the addition of the radio finally puts a significant constrain in the disk radius (at $19.40^{+2.81}_{-1.60} R_{eq}$), taking away the UV leads changes in the mass, age and extinction. Without the UV bump, the PDF for $E(B - V)$ spreads out, settling for a higher mean value. As they are correlated, the mass follows suit, wishing to probe higher values. The age, also correlated to both, climbs down from

Parameter	Value
Mass [M_{\odot}]	$4.66^{+0.06}_{-0.06}$
Rotation Rate	$0.74^{+0.06}_{-0.06}$
Age	$0.95^{+0.01}_{-0.02}$
Log Disk Base Density [cm^{-3}]	$11.97^{+0.03}_{-0.15}$
Disk Radius [R_{eq}]	$19.77^{+5.6}_{-2.2}$
Disk Density Exponent	$2.5^{+0.09}_{-0.29}$
Inclination [$^{\circ}$]	$39.51^{+6.6}_{-8.0}$
Distance [pc]	$79.84^{+2.2}_{-2.2}$
Extinction	$0.023^{+0.005}_{-0.005}$

Table 4.1 - Parameter results from BEMCEE for the complete SED of α Col.

its usual cornered position to sit at 0.85.

We continue the exercise of removing the smallest wavelengths on Fig. 4.7, now without the visible data. Both the mass and $E(B-V)$ are completely undetermined. The age spreads further, and so does the rotation rate. Disk parameters are still somewhat constrained, specially n and R_D . Removing the near-infrared in Fig. 4.8 continues this trend, and $\log n_0$ is now piling up on its minimum range value. Doing away with the mid-infrared (Fig. 4.9) leaves BEMCEE with only 5 points to model, and as a result the parameter determinations are very poor.

Finally, we perform an analysis using all data from the UV to the radio (Fig. 4.10). We immediately see that the influence of the UV in the stellar parameters returns, with the mass and the age going back to their previous positions around $4.66 M_{\odot}$ and 0.95. Additionally, the longer wavelengths now constrain the disk parameters to give us our best determination of all the parameters concomitantly.

All in all, this exercise shows that the more information we give the MCMC code, the better it can constrain the parameters as a whole. But we also notice that certain parts of the SED do a much better job with some parameters than others. This is shown a very clear way in the boxplots in Figs 4.12 to 4.20. Each boxplot represents the BEMCEE derived PDFs for each parameter, the different colours representing each SED cut. The line at the centre of the box stands for the mean value, the edges of the box the first and third quantiles (0.16 and 0.84). The upper and lower whiskers represent the limits of the distribution, while the individual points are outliers.

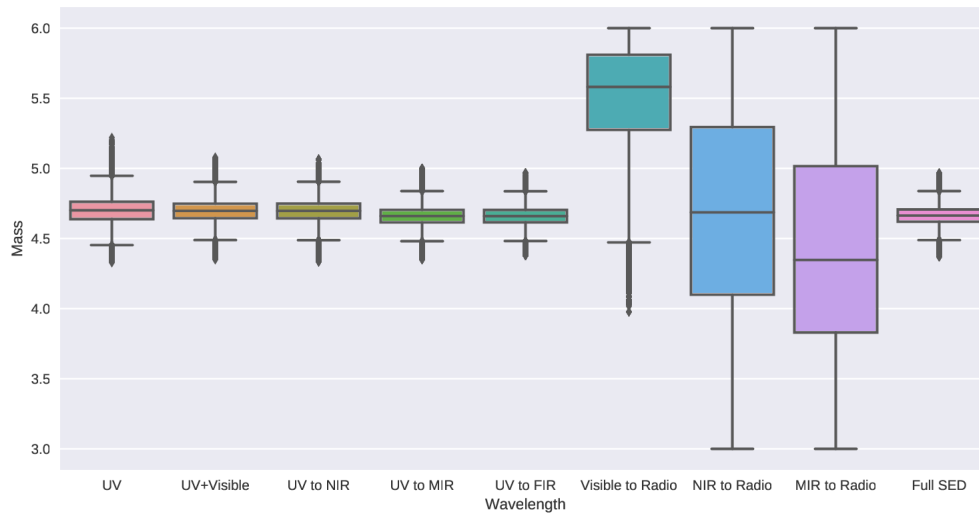


Figure 4.12: Boxplot for the PDFs derived in each SED cut BEMCEE run for the mass of the star.

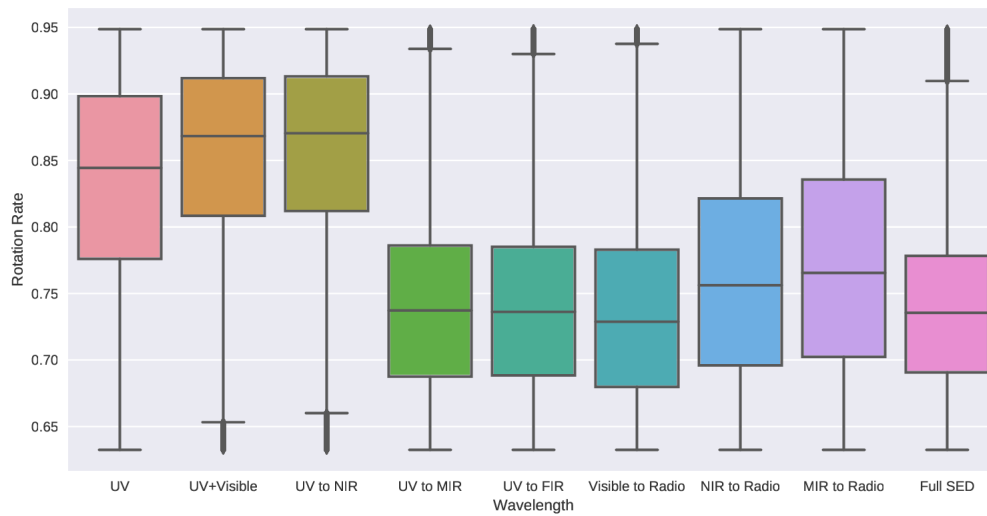


Figure 4.13: Boxplot for the PDFs derived in each SED cut BEMCEE run for the oblateness of the star.

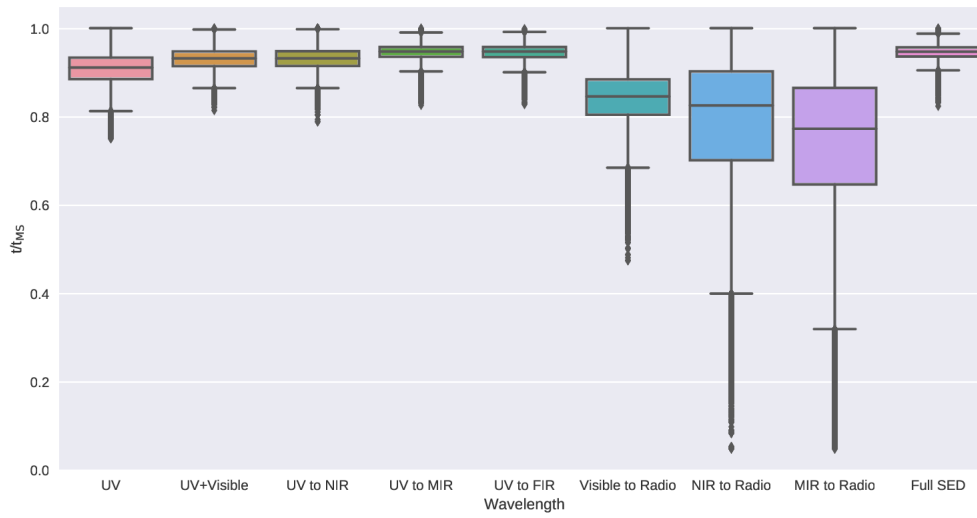


Figure 4.14: Boxplot for the PDFs derived in each SED cut BEMCEE run for the fraction of Hydrogen in the stellar core.

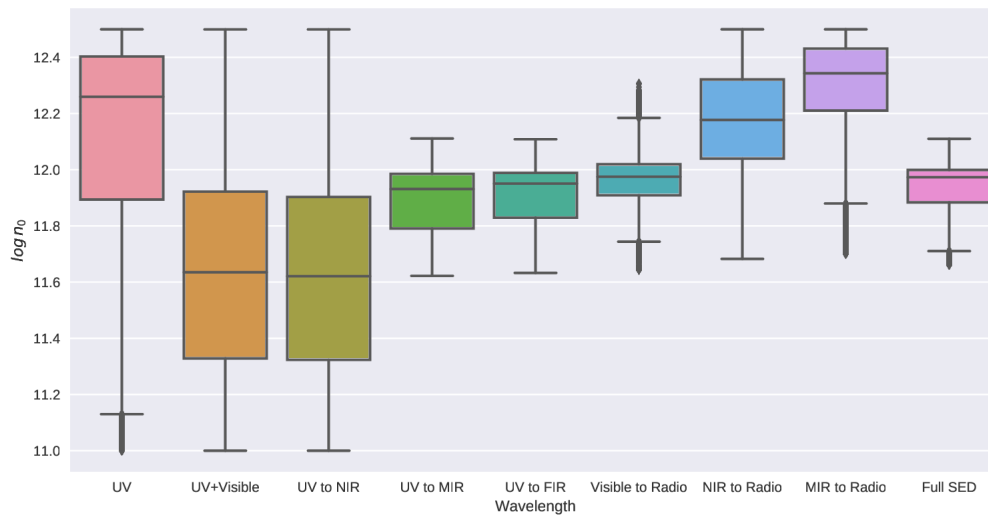


Figure 4.15: Boxplot for the PDFs derived in each SED cut BEMCEE run for the log of the base density of the disk.

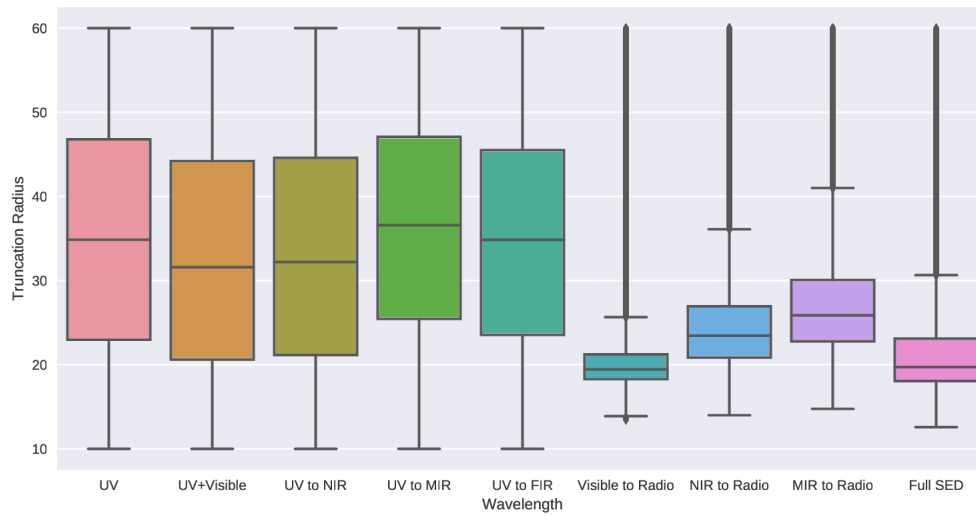


Figure 4.16: Boxplot for the PDFs derived in each SED cut BEMCEE run for the radius of the disk.

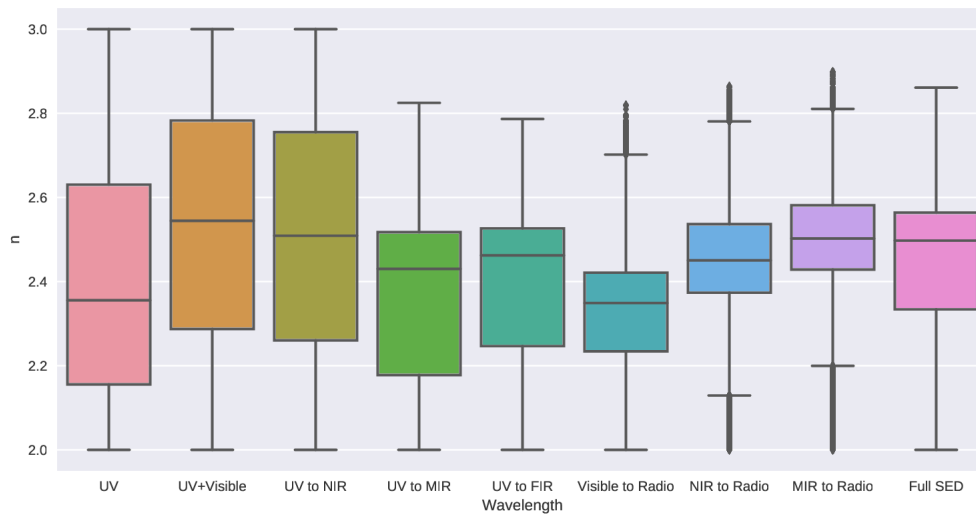


Figure 4.17: Boxplot for the PDFs derived in each SED cut BEMCEE run for the radial density exponent of the disk.

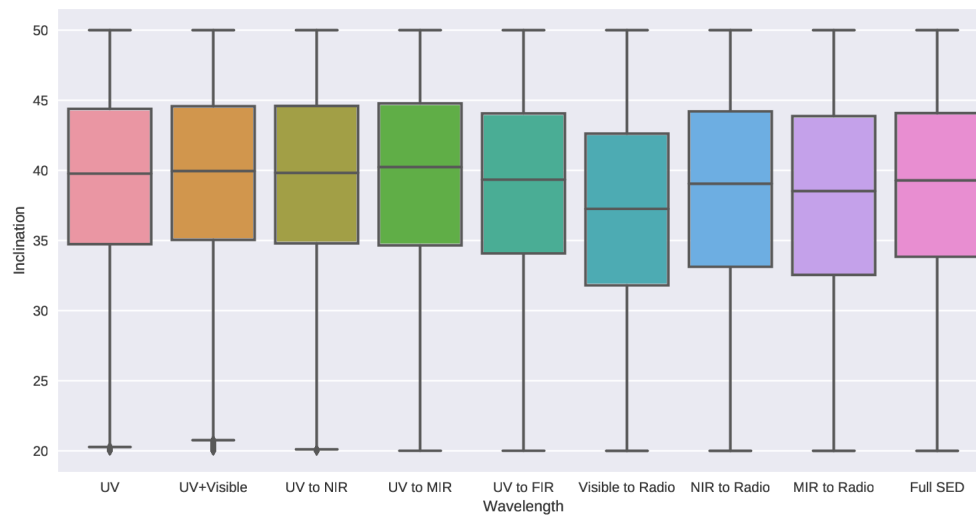


Figure 4.18: Boxplot for the PDFs derived in each SED cut BEMCEE run for the inclination of the system.

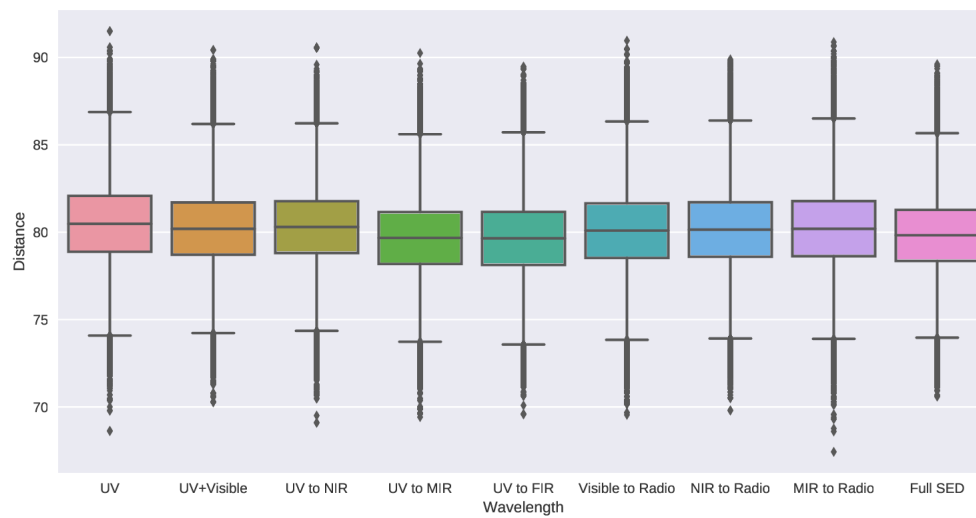


Figure 4.19: Boxplot for the PDFs derived in each SED cut BEMCEE run for the distance of the star.

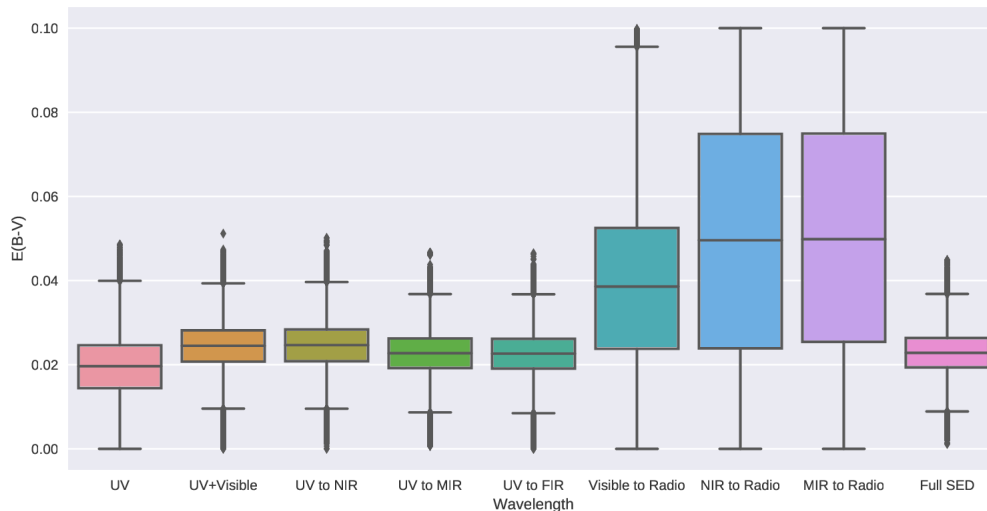


Figure 4.20: Boxplot for the PDFs derived in each SED cut BEMCEE run for the extinction.

The mass boxplot (Fig. 4.12) displays just how crucial the UV is to its determination. For the SED cuts where the UV is removed, the PDF becomes large and flat, until we re-add the UV in the full SED, and it once again sharpens. The age (or fraction of Hydrogen in the core - Fig. 4.14), is similarly affected, broadening once the UV is removed, and becoming undetermined. The opposite effect happens for the disk quantities (radius, Fig. 4.16, density level, Fig. 4.15, and density exponent, Fig. 4.17), that can only be reliably inferred with long-wavelength observations. The disk radius in particular could only be constrained when the radio observations were considered.

Figs. 4.18 and 4.19 show that the inclination and distance are the most stable parameters throughout our wavelength study. This makes sense, since these are parameters directly impacted by our priors, which are present in all BEMCEE runs. The priors being defined as Gaussian in nature enforces that the PDF also follows a similar shape.

The rotational rate (and consequently the oblateness) shows an interesting behaviour throughout our study. Looking just at the first three boxes on Fig. 4.13, there seems to be a trend for a high oblateness, but adding the infrared pushed it to lower values.

4.2 Polarimetry

The next step in our analysis for α Col was to perform the BEMCEE fit for the polarization. Our polarization data comes entirely from the Beacon Survey of Be stars at OPD,

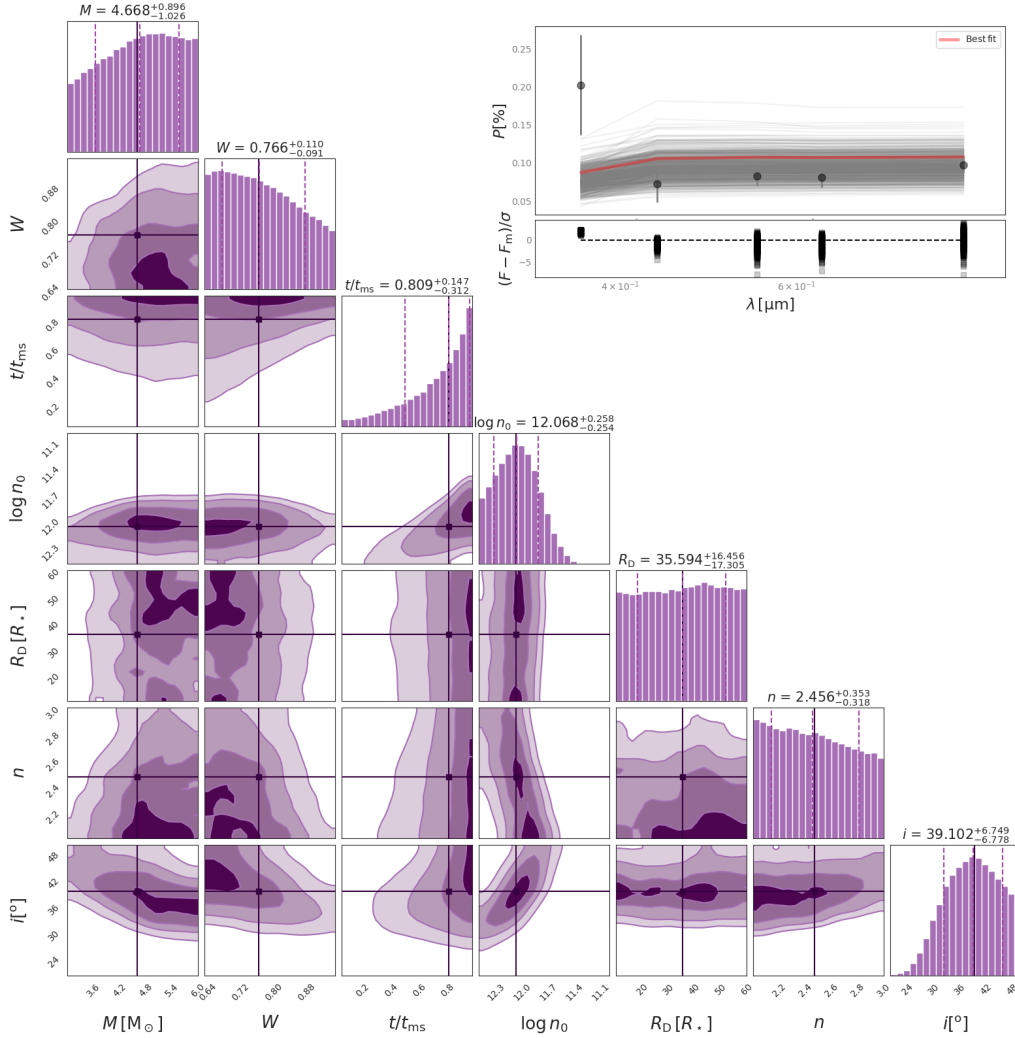


Figure 4.21: Corner plot for the polarization (U, B, V, R, and I), with 600 walkers and 2000 steps, $af = 0.32$. This run only included the priors on distance and $v \sin(i)$.

data ranging from 2007 to now. As can be seen in Fig 2.1 in Sect. 2.1, the star has a very low polarization fraction, due to its low density disk. The polarization levels have been more or less stable for the past decade, again confirming the relative stability of the disk. Fig. 4.21 is the corner plot obtained for our polarization data, taking the mean of all data for each filter. The error bars correspond to the standard deviation of the mean. We find that the stellar parameters are completely undetermined. This was expected, as polarimetry is an extraordinary probe of the disk, but contains less information about the star, since it is a measurement of scattered light.

The degree of polarization depends on the density of the disk and its geometry. Because the density, and hence the number of scatterers, drops quickly with radius, the bulk of the polarized light is created close to the star (see Fig. 1 of Carciofi 2011). Therefore, the most

relevant parameter related to the amount of light that is polarized is the density at the base of the disk, rather than its size and radial exponent. The polarization also depends strongly on the angle between the plane of the disk and our line of sight, so we also expect this observable to provide constraints to the inclination angle.

We test the hypothesis of whether setting our previous SED determination of the 3 stellar parameters (mass, rotation rate and age) would improve our result. We expect giving information on the star as a prior would make the determination of the disk parameters more precise, since the number of scatterers is also proportional to R_{eq} , and thus the central star characteristics do also play a role in the polarization level.

Setting the results obtained by the full SED fit for the stellar parameters as a prior is not as simple as the priors previously used. For $v \sin(i)$ and parallax, we simply defined a gaussian centered in the literature values, with a variance of 1σ of the measurements. What is needed now is to set the mass, rotation rate and age PDFs as priors. Essentially, after each BEMCEE run, we save the values each parameter took for every walker in every step. From this chain, it is easy to reconstruct exactly the same histogram as the one presented in the corresponding corner plot. We use the kernel density estimation (KDE) of the PDFs, which is a much smoother function containing the same information, to set up the prior for the polarization. Fig. 4.22 are the new results, using the KDE from the full SED determination of the mass, W and t/t_{MS} as prior.

All in all, there is no great change between Fig. 4.21, with no stellar priors, and Fig. 4.22 with the priors beyond a slight shift of the $\log n_0$ to 11.87 and a slight decrease on the width of the PDF. Our interpretation for this is that the polarization degree depends only weakly on the stellar characteristics, and therefore not knowing the stellar parameters do not hamper us to obtain a reasonable estimate of the disk density.

Our results for the best fit model for the polarization (Fig. 4.22) recovers the base density $\log n_0$ and i , but has flat PDFs for both R_D and n , as expected from theory. Both $\log n_0$ and inclination agree within the uncertainties with the results obtained from the full SED analysis. This is an important result: two fundamentally different observables, photometry and polarimetry, are agreeing of the disk properties and on the inclination angle of the system, even when no priors connect the two simulations.

Fig. 4.23 is the combined corner plot for the SED and polarimetry final results. The PDF resulting of the multiplication of the two results is the black outline, which we found

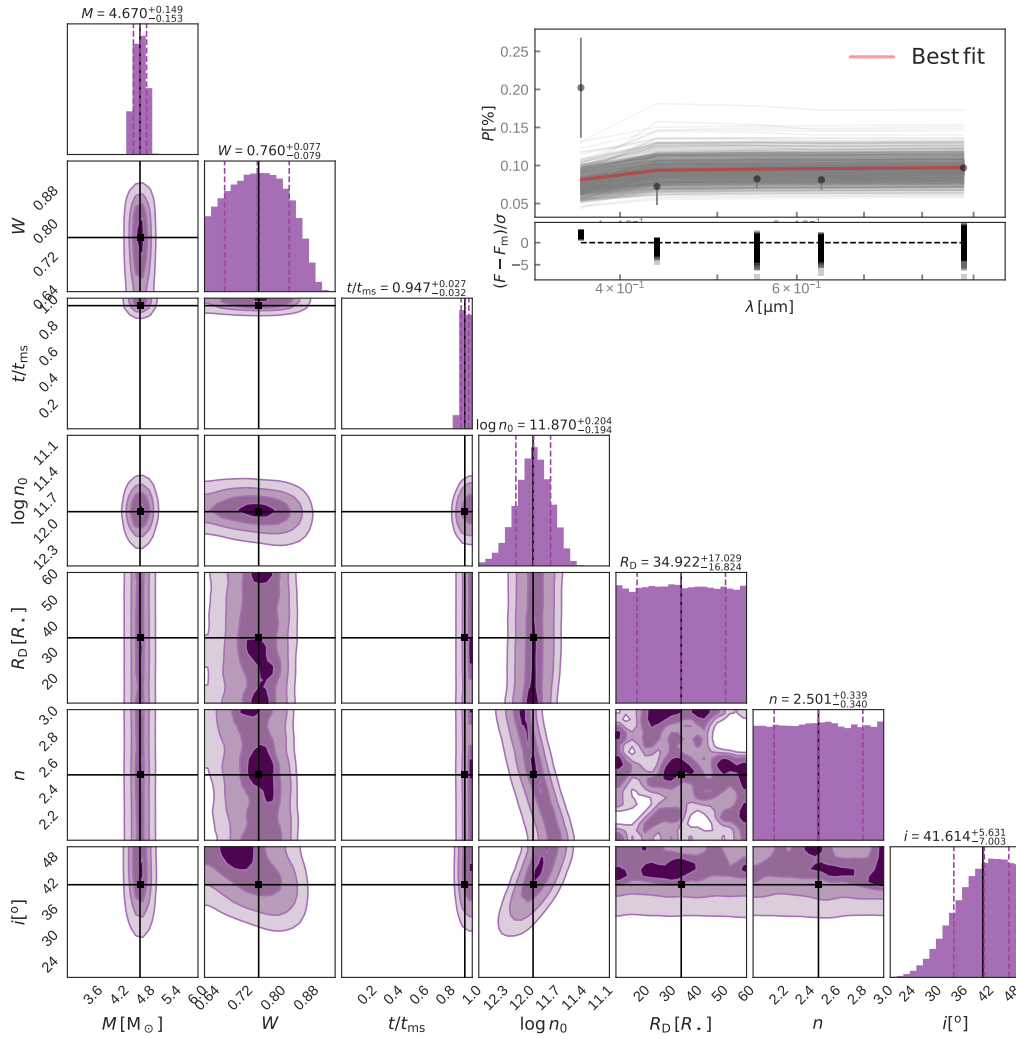


Figure 4.22: Corner plot for the polarization (U, B, V, R, and I), with 600 walkers and 2000 steps, $af = 0.37$. This run included the KDE priors on the mass, W and age of the star as determined in the run shown in Fig. 4.10.

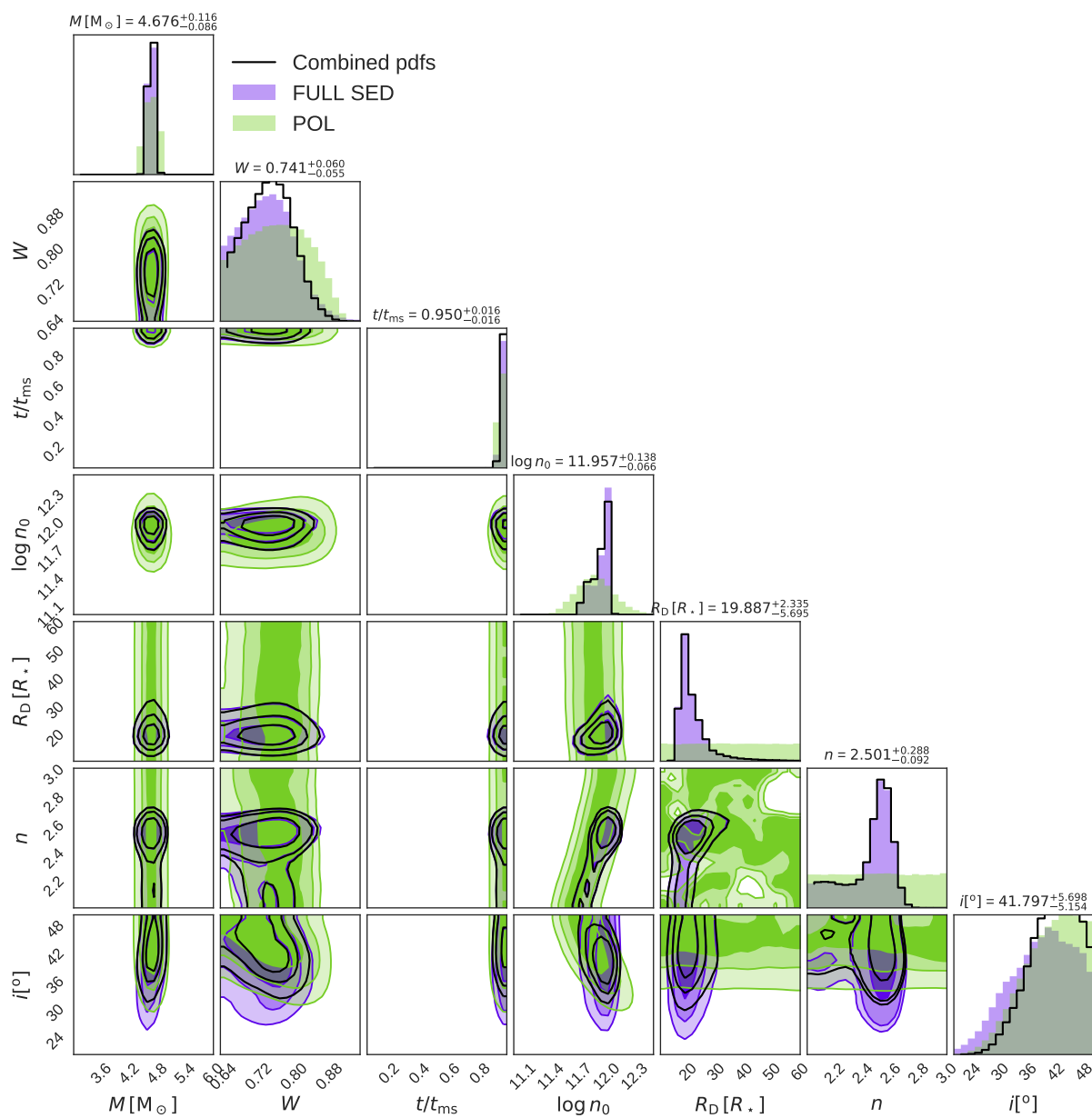


Figure 4.23: Combined corner plot for the full SED result (Fig. 4.10) in purple and the polarimetry result (Fig. 4.22) in green, with the combined PDFs in black.

Parameter	Value
Mass [M_{\odot}]	$4.68^{+0.12}_{-0.09}$
Rotation Rate	$0.74^{+0.06}_{-0.06}$
Age	$0.95^{+0.01}_{-0.02}$
Log Disk Base Density [cm^{-3}]	$11.96^{+0.14}_{-0.07}$
Disk Radius [R_{eq}]	$19.89^{+2.3}_{-5.7}$
Disk Density Exponent	$2.50^{+0.29}_{-0.09}$
Inclination [$^{\circ}$]	$41.78^{+5.7}_{-5.1}$
Distance [pc]	$79.84^{+2.2}_{-2.2}$
Extinction	$0.023^{+0.005}_{-0.005}$

Table 4.2 - Parameter results from BEMCEE for the combination of the results for the SED and polarimetry of α Col. Distance and extinction are the same as the SED result, as these parameters are not included in the polarimetry run.

was the best way to represent a combination of the results. Table 5.1 presents the parameters of this combination. We can see that for parameters such as i and distance, which were defined well for both the SED and polarimetry, the end result is a sharper PDF with smaller errors.

4.3 Correlations

With well determined results, we are now able to analyse the correlations between the various parameters. The correlations maps in the corner plot are not the greatest way to visualise the correlations and their relative strengths, so we refer to Figs. 4.24 and 4.25, the chord diagrams corresponding to the our best results of the full SED (Fig. 4.10) and polarization (Fig. 4.22).

On a chord diagram, the correlations between parameters are show as straps connecting their relative segments on the circle. The width of the strap represents how strong the correlation is, relative to all other correlations. Some parameters are strongly correlated, such as the disk base density $\log n_0$ and the radial density exponent n , while others, such as mass and rotation rate W , seem not to be correlated at all. Below we list the most significant correlations and their physical causes.

Mass and inclination: There appears to be a positive correlation between mass and inclination angle. The correlation could be explained in terms of temperature. A more massive star would produce a hotter spectrum than a less massive one. However, we

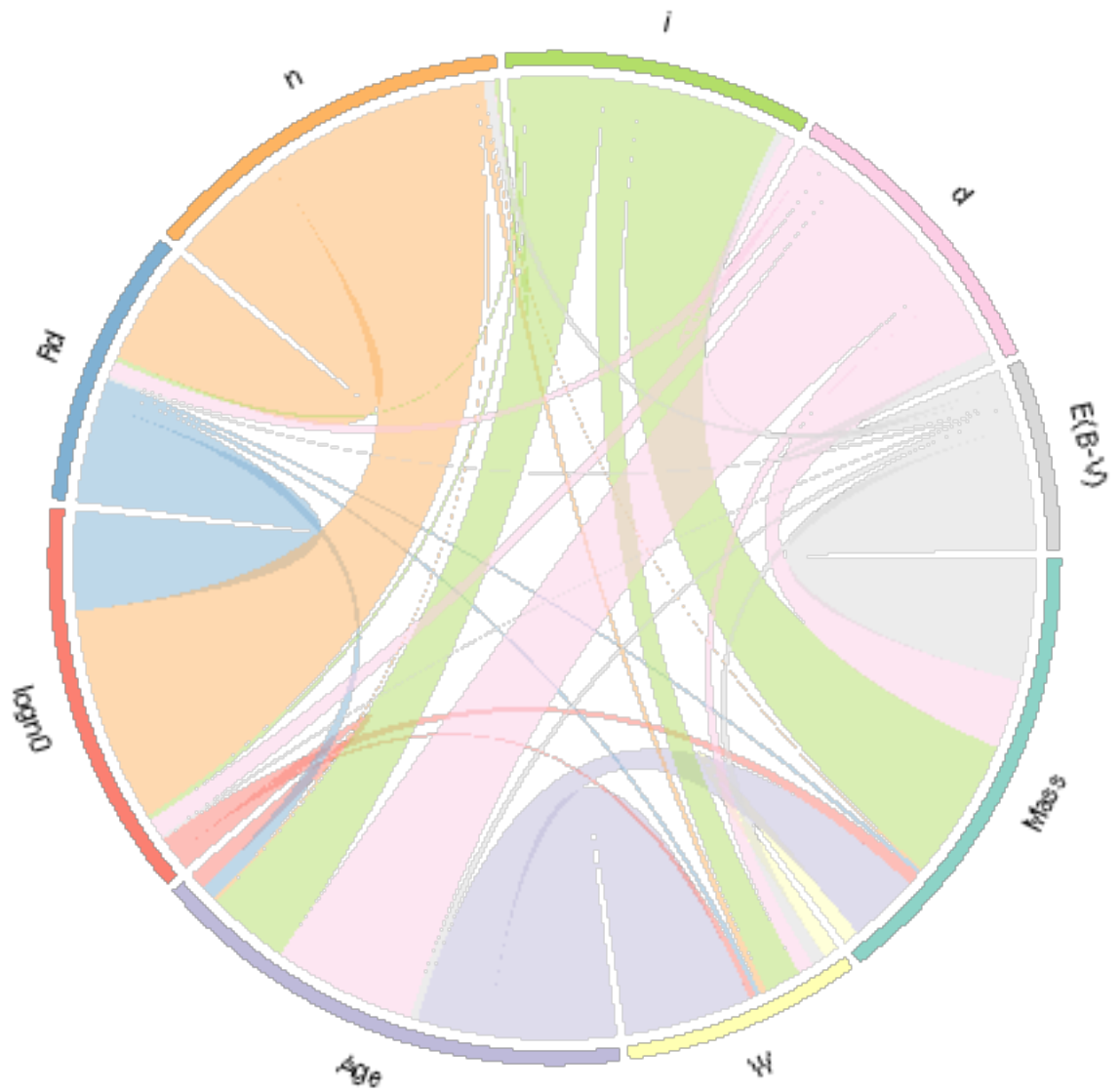


Figure 4.24: Chord diagram for the correlations seen in Fig. 4.10

are considering a Be star, which does not have a spherical structure, but an oblate one. Additionally, due to the effects of gravity darkening, the equator of the star is colder than the pole. If the Be star is seen in an edge-on case, it would have a smaller projected area than if it is seen pole-on. The difference in temperature between the pole and the equator will further magnify this effect. Therefore, a hotter (and more massive) star seen edge-on could also be interpreted as a colder (and less massive) star seen pole-on.

Rotation rate and inclination: As expected, there is a negative correlation between these two parameters, as a rotating star seen pole-on is perceived as not rotating at all, while the effect is maximized when seen edge-on. Also, the radius of the disk is larger if the star is seen pole on than edge on due to oblateness.

Rotation rate and age: The age of the star has implications on its size, R_{pole} and R_{eq} , as its radius grows during main sequence evolution. As such, it correlates with the rotation rate, that depends on the stellar radius. An older and larger star rotating at the same speed as a younger and smaller star would be seen as having a lower rotation rate than the latter.

Base density and inclination: There is a positive correlation between the inclination angle and the base density. As the inclination increases, the projected area of the disk would decrease, which would result in less flux seen by the observer. However, if we increase the density of the disk, the amount of flux emitted would also increase. Hence, a dense disk seen edge-on could also be interpreted as a tenuous disk seen pole-on.

Extinction and mass: There is a positive correlation, as the stronger the extinction, the less UV flux reaches the observer. As such, it would be necessary to have a more massive star to reach the same amount of flux as a less massive star seen with a smaller $E(B - V)$.

Base density and radial density exponent: We can see a positive correlation between the base density of the disk and the radial density exponent. This can be better understood in terms of emission by a pseudo-photosphere. If n increases, the spectrum becomes steeper, which translates in the SED as less flux excess. To remedy this, the disk would have to be denser, which will increase the excess. In this way, a disk with a steeper density slope and a denser inner disk have a similar SED than a disk with a shallower density slope, with a tenuous inner disk.

Disk radius and base density: There is a positive correlation. The reason is very

clear: if the disk is smaller, it would decrease the emission. Increasing the base density would counterbalance this effect.

Disk radius and radial density exponent: There is a positive correlation. A likely cause is that as we decrease the size of the disk, we decrease the emitting area, which will cause a drop in the excess. To balance this, n would have to decrease as well, leading to an increase in excess.

Deriving the correlations of the parameters along with their PDFs was an important factor in our early choice for employing Bayesian-MCMC techniques in our work with BeAtlas. As such, ours (this work and Mota 2019) are the first studies of Be stars that are able to obtain and quantify the correlations of its parameters, both stellar with stellar, disk with disk, and stellar and disk self-consistently.

4.4 *Uncertainties and BEMCEE*

During our analysis of the SED cuts, we expected variations in the parameter PDFs as we added more data to the code. However, in our first runs with BEMCEE, a rather dramatic alteration was seen in the PDF for the rotation rate W when we added the mid-infrared (5.0 to 40 μm) to the analysis. The PDF that was previously piled up in the higher end of the W range suddenly moved to the opposite side, in the lower end of the range. This behaviour was unexpected, as the rotation rate does not exert such a strong influence in this particular wavelength range (see Fig. A.2).

Our observational data at the MIR region are two AKARI points at 9 and 18 μm , two IRAS at 12 and 25 μm and two WISE at 11.5 and 22 μm (Tab. 2.2). An inspection of the data lead us to realise that the uncertainty of the 9 μm AKARI point was very low, with a σ/flux of 0.003, or 0.3%. As this point is so precise, our likelihood function would attribute a high weight to it when calculating the χ^2 . Plotting the squared residues of our fit to the most likely model, we find that indeed the AKARI data point has a much higher weight than any of the other data point in our set, causing the code to fixate on fitting it in detriment of the rest of the SED data (Fig. 4.26).

This leads us to the discussion of how accurate can a photometric measurement of a Be star truly be in a time independent study such as ours. The uncertainty in the AKARI point comes directly from their database, following their own procedure, and measurement

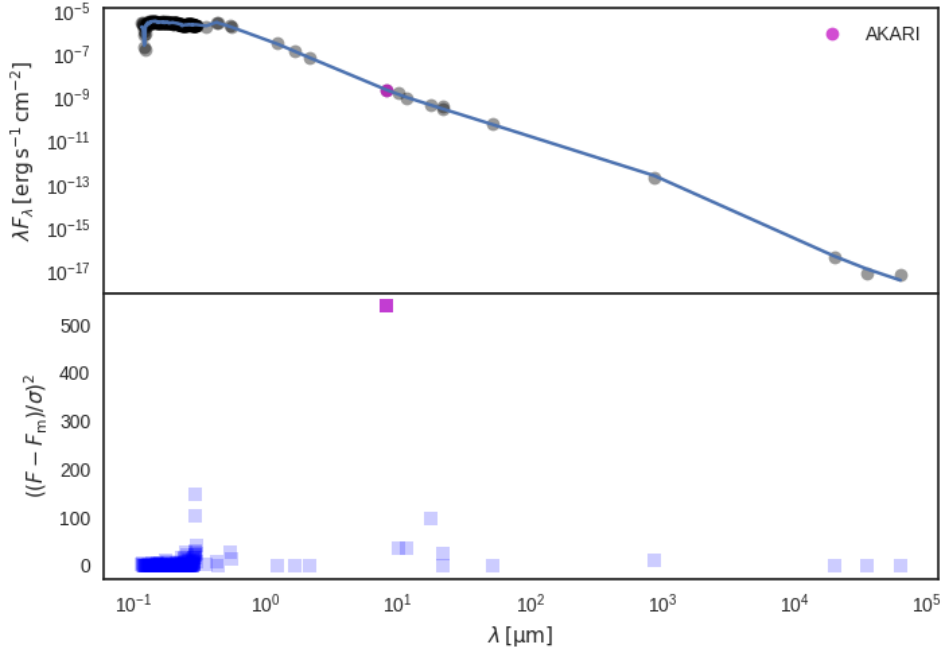


Figure 4.26: Top: Best fit SED (model of Fig. 4.10). Bottom: squared residue plot.

corresponds to the flux emission at the moment the data was taken. However, Be stars, even ones as quiet as α Col, are variable in time in many timescales, as discussed in Sec. 1.4.1.2. In this work, where we collect data taken from various years, our focus is more on modelling the mean shape of the SED throughout the period for which we have data than on very precise individual points. From the $\text{H}\alpha$ equivalent width measurements shown in Fig. A.1, the line varies nearly 3%. Therefore, we chose to set a minimum value for all errors on SED photometry values at 1%. The resulting squared residue plot is shown in Fig. 4.27. All our results shown in Sec. 4.1 make use of this lower limit for the errors.

4.5 Disk Truncation and Binarity

One of the most interesting results of our analysis relates to the physical size of the disk. From our complete result (SED+polarimetry), we obtain that the radius of the disk is $19.89_{-5.7}^{+2.3} R_{eq}$. In the context of the VDD, the disk should be able to expand to hundreds of stellar radii, up until the point where the radial velocity in the outermost region reaches the sound speed. At the sonic point, the disk reaches what is called the transonic regime, where the azimuthal velocity is no longer Keplerian, but angular momentum conserving.

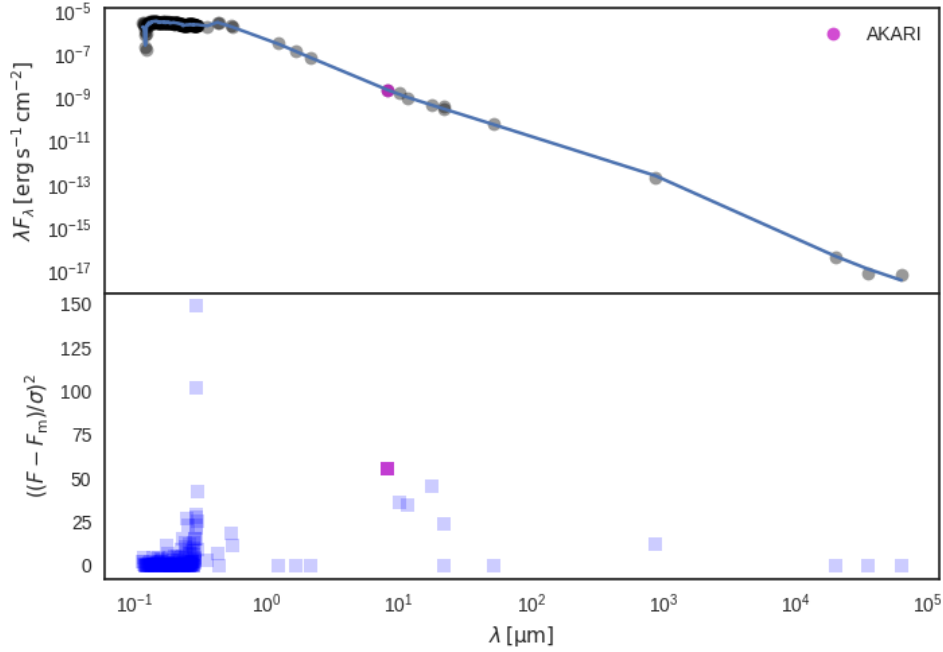


Figure 4.27: Same as Fig. 4.26, now limiting the minimum error for a SED point at 1%

This also leads to a change in the density profile of the disk, making it steeper (Okazaki, 2001).

The sonic point relates to v_{orb} and c_s as (Krtićka et al., 2011)

$$\frac{R_s}{R_{eq}} = \frac{3}{10} \left(\frac{v_{orb}}{c_s} \right)^2, \quad (4.1)$$

meaning that typical values for R_s are about $430 R_{eq}$ for a B9V star and $350 R_{eq}$ for a B0V.

As such, the standard VDD theory we have been relying on so far does not account for disks with such small radii as we found for α Col. One possible solution is that it is caused by thermal effects on the outer disk that we are not considering, such as a strong transition between a partially ionized inner disk, and a fully neutral outer disk. Another is the possibility of the presence of an unseen binary companion affecting the disk and truncating it (Okazaki et al. 2002, Panoglou et al. 2016).

Truncating the disk at a radius smaller than the effective radius of the pseudo-photosphere affects the amount of flux emitted by the outer disk, and therefore leads to a steepening of the SED in the radio/centimetre region. Figure 4.28 compares 3 models, with the same parameters except the truncation radius. The effect of the disk truncation is immediately

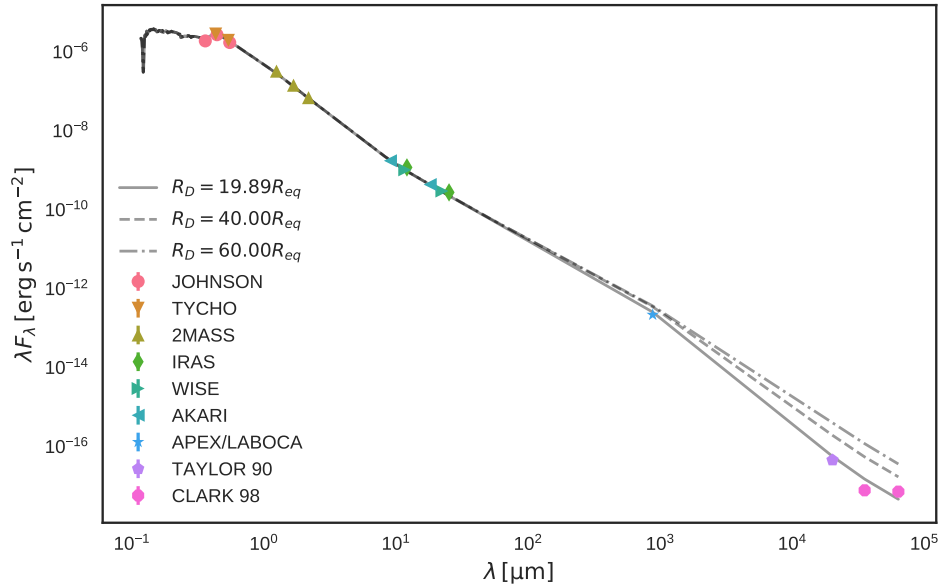


Figure 4.28: Comparison of 3 BeAtlas models with the same parameters except for the truncation radius R_D , plotted with the photometric data of α Col.

visible in the radio region, starting at the APEX data point in $870 \mu\text{m}$.

This feature was first observed by Waters et al. (1991), where they analyse VLA and IRAS data for 6 bright Be stars: γ Cas, β Mon A, η Tau, EW Lac, ψ Per, and β CMi. γ Cas is now famously in a binary system, but at the time none of the stars was believed to have a companion. Waters et al. suggest as a cause for this “turnover” a change in the geometry of the disk, or an additional acceleration of the material in the outer region, but in no great detail.

In Klement et al. (2015)’s multi-technique analysis of β CMi, this effect was once again observed with more radio data. The existence of the feature, now dubbed SED turndown, lead to a density profile that could not be accurately described with only one power-law exponent, as it requires a steeper outer disk. Klement et al. suggested the presence of a binary companion as the cause of the change in slope, as this is the most likely cause in the VDD context. Additionally, β CMi has V/R variations in the $H\alpha$ peaks with a period of about 183 days, usually an indicator of binarity (Panoglou et al., 2018). They explored the possibility of a single companion being the cause of both effects and found them in good agreement. Since there was direct indication of a binary star in any of the available spectra, the companion was thought to be either a late main sequence star or a subdwarf (sdB or sdO). Dulaney et al. (2017) set out to look for the companion in radial velocity and V/R variation analysis, and their results confirm that β CMi’s binarity is very likely.

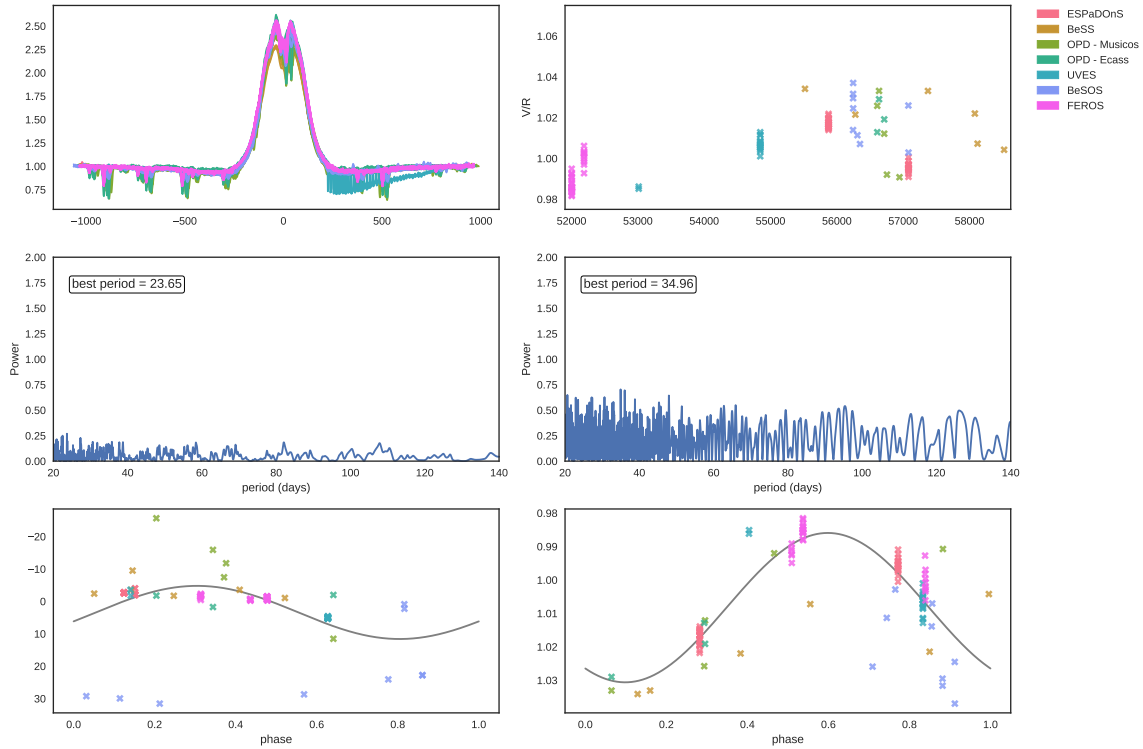


Figure 4.29: Collected $H\alpha$ spectra for the Be star α Col. Our goal was to look for detectable periods in the radial velocity shifts of the line, and on violet/red peaks intensity. The upper left panel is our spectra corrected for the RV shift. The middle left panel is the Lomb Scargle intensity plot; the best period is not, however, significant enough to be actually considered a detection. The bottom left panel is the data folded in phase with the “best” period found on the Lomb Scargle plot. The panels on the right are the same, but for the V/R variation. Again, no clear period was detected. The results are therefore inconclusive, likely due to the inhomogeneity of the data.

As such, we attempted to do the same for α Col, looking for signs of the companion in other observables. According to Panoglou et al. (2016)’s work with SPH simulations of Be stars in binary systems, if we assume a coplanar, circular orbit of the secondary, the truncation radius relates to the orbital separation as $R_{orb} \sim R_D/0.8$. Therefore, we estimate the period of α Col’s companion should be in the range of 70 to 90 days for a low mass companion ($\leq 1 M_\odot$), which is a reasonable assumption given that the companion has never been detected by observations (such as Oudmaijer and Parr 2010, Wang et al. (2018)), but is listed in the Washington Visual Double Star Catalog ². As we had access to many $H\alpha$ spectra, we combed through them in search of any periodic variation, as in radial velocity (RV) shifts and V/R variations that matched this estimate.

We followed Dulaney et al. (2017)’s procedure, using double Gaussian cross-correlation

² VizieR entry for α Col in the WDS catalogue <http://vizier.u-strasbg.fr/viz-bin/VizieR-5?-ref=VIZ5d642e1a532d&-out.add=.-source=B/wds/wds&recno=29387>

method, from Shafter et al. (1986) (see also Grundstrom (2007), appendix A) to find the values of the radial velocity shift of the line. It uses two Gaussians of opposite sign separated by a given range in velocity, Δv , and with FWHM of $\Delta v/3.5$ as a template. This template is then cross-correlated with the H α line profile as the program moves the template around the line, keeping the separation fixed. The value of the radial velocity shift corresponds to the root of the cross-correlation function. Before applying this method, however, we had to correct the data for heliocentric velocity. This correction is necessary when looking for radial velocity signatures in spectra because the motion of the Earth around the Sun leads to Doppler shifts in the lines as well. Putting all spectra in the reference frame of the Sun is therefore necessary to avoid this effect.

This proved to be more uncertain than expected due to lack of information on the corrections already performed in some of the spectrum `.fits` files. Once corrected, the cross-correlation method was applied to derive the shifts in km/s. From this result, we also subtracted the known radial velocity of α Col of 35 km/s (Gontcharov 2006, Duflot et al. 1995), as it is the systemic velocity. After the corrections, we used a Lomb Scargle period calculator to search for possible periods.

As shown in Fig. 4.29, we were unable to detect any period in either the radial velocity shifts of the line or on the V/R variation, although some degree of variation is present. As Dulaney et al. (2017), we attempted to use the `PERIOD04` routine to look for periods in the Fourier transform of the time series in addition to the Lomb Scargle method, but reached the same inconclusive results. This was likely due to the inhomogeneity of our collected spectra (see Sec. 2.1), and their uneven distribution in time. The fact that spectra came from various sources meant different calibration among the spectra, so we could not reliably find signs of RV shifts. V/R variations also proved to be non-periodic as far as our data was concerned. Also, although we had access to 112 spectra (see Table 2.3), many of them were taken on the same or consecutive nights. Since the phase variations we were looking for were of the order of tens of days, their contribution to the time series was very small. For example, our data from ESPaDOnS, while amounting to 41 spectra, only covers two nights. Dulaney et al. (2017) had the advantage of having over a hundred well spaced spectra from the same telescope and instrument (Ritter Observatory) for β CMi, so heliocentric velocity and telluric lines corrections were greatly simplified. We believe more data is needed to reach a definite conclusion on the existence of the secondary and

its period based on V/R and RV variation.

Analysis and Discussion

Our final result, the combination of the SED and polarization determinations of the parameters for α Col, are given in Table 5.1. The stellar mass of $4.68_{-0.09}^{+0.12} M_{\odot}$ agrees with the determination of Chauville et al. (2001) and Zorec et al. (2016) within the uncertainties. The rotation rate of $0.74_{-0.06}^{+0.06}$ indicates a $R_{eq}/R_{pole} = 1.27 \pm 0.2$. Interpolating the values derived for the mass, W , and age with the Geneva evolutionary model grid, we find a log luminosity of ≈ 2.95 , agreeing within 1σ with the determination of Levenhagen and Leister (2006) and Zorec and Royer (2012); an $R_{eq} \approx 6.46 \pm 0.5 R_{\odot}$, which does not quite agree with the determination of Arcos et al. (2018) and Meilland et al. (2012), but is compatible within 3σ , and an $R_{pole} \approx 5.23 \pm 0.3 R_{\odot}$. From these values, we derive a $v_{crit} \approx 341.60 \pm 10.0$ km/s, in accordance to the values derived by Zorec et al. (2005, 2016) from their analysis of α Col's spectral lines in 1σ . From W we can also derive the rotational velocity of the star as $v_{rot} \approx 275.12$ km/s. Combining this result with our determination of the inclination, we find a resulting $v \sin(i)$ of 174.46 km/s, similar to the determinations of Levenhagen and Leister (2006), Zorec and Royer (2012) and Zorec et al. (2016) within 1σ . The value of $t/t_{MS} = 0.95_{-0.02}^{+0.01}$ indicates that the star is evolved, at the very end its main sequence lifetime. Our group is working on the possibility of expanding HDUST's ability to study stars just past MS ($t/t_{MS} > 1$) like α Col. It is interesting to note that most of these literature parameter determinations comes from spectral line analysis, while in our work we only considered photometry, polarimetry and UV spectroscopy, but no line analysis, and still recovered most of the values determined by these studies.

As discussed in Sec. 4.5, α Col's disk has a radius of $19.89_{-5.7}^{+2.3} R_{eq}$. The truncation of the disk seems to indicate the presence of an unseen binary companion to α Col, as theorized in Klement et al. (2015) for the similar case of β CMi. The following studies of

Parameter	Value
Mass [M_{\odot}]	$4.68^{+0.12}_{-0.09}$
Rotation Rate	$0.74^{+0.06}_{-0.06}$
Age	$0.95^{+0.01}_{-0.02}$
Log Disk Base Density [cm^{-3}]	$11.96^{+0.14}_{-0.07}$
Disk Radius [R_{eq}]	$19.89^{+2.3}_{-5.7}$
Disk Density Exponent	$2.50^{+0.29}_{-0.09}$
Inclination [$^{\circ}$]	$41.78^{+5.7}_{-5.1}$
Distance [pc]	$79.84^{+2.2}_{-2.2}$
Extinction	$0.023^{+0.005}_{-0.005}$
R_{eq}/R_{pole}	1.27 ± 0.2
R_{eq} [R_{\odot}]	6.46 ± 0.5
R_{pole} [R_{\odot}]	5.23 ± 0.3
v_{crit} [km/s]	341.60 ± 10.0

Table 5.1 - Parameter results from BEMCEE for the combination of the results for the SED and polarimetry of α Col. Distance and extinction are the same as the SED result, as these parameters are not included in the polarimetry run.

Klement et al. (2017, 2019) searched for signs of SED turndown in a larger sample of Be stars, both known binaries and single stars. Klement et al. (2017) revisited the studied of Waters et al. (1991) IR data for γ Cas, β Mon A, η Tau, EW Lac, ψ Per, and β CMi and confirmed the presence of SED turndown for the targets¹ with new radio data.

In Klement et al. (2019), the authors make a survey of 57 Be stars with IR and radio data in order to search for more SED turndown cases. From their sample of 57 Be stars, 31 stars do not have enough data to conclusively determine whether the turndown is present or not. For the remaining 26 Be stars with sufficient data to accurately interpret the slope of the long-wavelength SED, the turndown has been confirmed for 100% of the cases. Hence, there is reason to believe all Be stars may be binaries, only we were unable to spy their companions until now. α Col joins this statistic as a putative binary.

The disk, as expected from the low polarization signal, is tenuous, with a log base density of $11.96^{+0.14}_{-0.07}$, corresponding to $9.08^{+3.5}_{-1.3} \times 10^{-13} \text{ g cm}^{-3}$, larger than the previous determination of Vieira et al. (2017) of $11.51^{+0.02}_{-0.01}$. The radial density exponent sits at $n = 2.50^{+0.29}_{-0.09}$, in agreement with Vieira et al. (2017) determination of $n = 2.76^{+0.04}_{-0.03}$. This is an interesting result: from the steady state isothermal solution of the VDD, n is expected

¹ β Mon A was inconclusive, but the turndown is now confirmed in Klement et al. (2019)

to be exactly 3.5. Vieira et al. (2017) classified disks with $n \leq 3.0$ as dissipating disks (as shown in Fig. 1.4).

However, α Col has by all means an incredibly stable disk, showing very little variation in line measurements of H α (Fig. A.1) and polarization (Fig. 2.1). The TESS² light curve for α Col, covering a period of 27 days, shows no signs of outbursts or other events connected to disk variability (Fig A.3 - see also Sec. 1.4.1.2). We find no other indication that α Col has undergone a disk build-up or dissipation event since its discovery as a Be star in 1897. Curiously, this result is not unprecedented, as there are records of other apparently stable Be stars (as in active and not undergoing disk dissipation or build-up) with radial exponents lower than 3.5.

In recent years, several in-depth studies of individual Be stars in using our BeAtlas grid have been performed: ι Aqr (de Almeida et al., 2019), 66 Oph (K. Marr 2019, priv. comm.) and α Ara Mota (2019), apart from part from the already mentioned β CMi and of course, α Col itself.

β CMi (HD 58715), a stable Be star, was the focus of a multi-technique study by Klement et al. (2015), using HDUST models. It was later revisited by Mota (2019) and subject to the full BEMCEE analysis of its UV, polarimetric, and photometric data. They found its best result for the disk parameters at $\log n_0 = 11.99^{+0.21}_{-0.10}$ ($\approx \rho_0 = 9.74 \times 10^{-13}$ g cm⁻³) and $n = 2.44^{+0.27}_{-0.16}$.

ι Aqr (HD 209409) is a Shell star, a Be star seen at a close to edge-on inclination. It possesses a fairly stable disk, as attested by the regularity of its H α line measurements (Rivinius et al. 2006, Sigut et al. 2015). de Almeida et al. (2019) used visible and near-infrared CHARA/VEGA and VLTI/AMBER spectro-interferometric data of the H α and Br γ lines to characterize the star, using BeAtlas and MCMC analysis. Their best fit values for the base density of the disk and its radial density exponent are $\rho_0 = 5.0 \times 10^{-12}$ g cm⁻³ and $n = 3.0$. An earlier study of the same star using NPOI H α interferometric visibilities and the BEDISK radiative transfer code (Sigut and Jones, 2007) found $\rho_0 = 6.0 \times 10^{-12}$ g cm⁻³ and $n = 2.7$ (Sigut et al., 2015). Neither study quoted their respective uncertainties in these values.

α Ara (HD 158427) is an early type Be star, and quite close by, at ~ 74.3 pc away. It was meticulously studied by Mota as one of the first tests for BeAtlas and BEMCEE,

² <https://tess.mit.edu/>, courtesy of post-doc J. Labadie-Bartz

Star		Vieira et al. (2017)			Klement et al. (2019)		
HD	HR	n (AKARI)	n (WISE)	Mean n	n (IR)	n (Radio)	Mean n
5394	264	3.29	-	3.29	2.92	2.96	2.94
23630	1165	2.9	3.2	3.05	2.89	3.02	2.95
25940	1273	2.8	2.7	2.75	2.46	-	2.46
32343	1622	2.2	2.0	2.1	2.06	-	2.06
37795	1956	2.5	2.5	2.5	2.69	-	2.69
41335	2142	-	3.0	3.0	2.85	-	2.85
58715	2845	3.0	2.7	2.85	3.13	3.44	3.285
91465	4140	3.1	3.3	3.2	2.65	-	2.65
105435	4621	2.8	3.0	2.9	2.44	-	2.44
109387	4787	2.5	2.6	2.55	2.78	-	2.78
148184	6118	2.9	3.1	3.0	2.58	-	2.58
158427	6510	-	2.9	2.9	3.16	-	3.16

Table 5.2 - Crossmatch of stable Be star radial density exponent derived by Vieira et al. (2017) and Klement et al. (2019). The bold stars are α Col, β CMi and α Ara.

with observational data in photometry and polarimetry used to derive its fundamental parameters. The most likely values for the disk parameters are $\log n_0 = 12.87_{-0.02}^{+0.03}$ ($\approx \rho_0 = 7.38 \times 10^{-12} \text{ g cm}^{-3}$) and $n = 2.85_{-0.10}^{+0.25}$.

66 Oph (HD 164284) is undergoing a similar study to the one presented here, once again with BEMCEE, by our collaborators at the University of Western Ontario. It has undergone disk build up from 1957 to 1995, so it could, during that period, be considered an active Be star. The most recent results from the MCMC analysis with photometry and UV spectroscopy of the star indicate it had a disk with a base density of $\rho_0 = 1 \times 10^{-11} \text{ g cm}^{-3}$ and a n of 2.4 (K. Marr, priv. comm.).

All these individually studied stars show a radial density exponent lower than the canonical 3.5. Looking further into this apparent trend, we turned to the survey of Klement et al. (2019) on SED turndown in Be stars. In their Table 7, the authors compile the found values for n for the Be stars in their sample that can be considered stable, and that show clear signs of SED turndown. We crossmatch their results with the values found for the same stars in Vieira et al. (2017)'s survey, finding 12 stars that were a target in both works, and compare the values of n derived in Table 5.2 and Fig 5.2.

For the stable Be stars sampled in both surveys, all 12 show a $n < 3.5$ consistently in both studies (Fig. 5.2 and histogram in Fig. 5.1). We also did a quick study of the $n \sim 2.5$

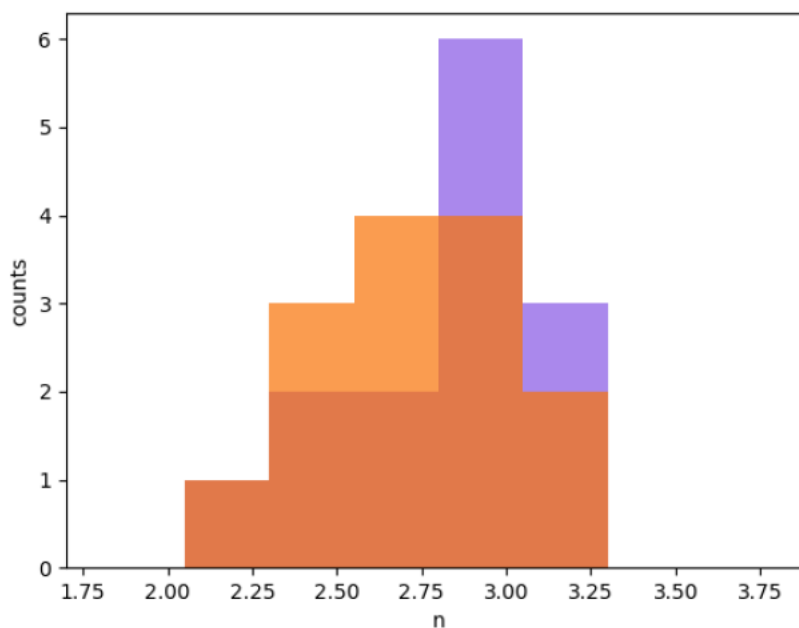


Figure 5.1: Histogram of the values of n from Vieira et al. (2017) (in purple) and Klement et al. (2019) (in orange)

Be stars that are only in Vieira et al. (2017), searching for available $H\alpha$ spectra on the BeSS database to check whether these stars appear to be stable. Out of 13 stars, we found 5 whose spectra do not change significantly over the period covered by the observations, but a more detailed analysis is needed to confirm if they truly fall on this category.

The fact that at least 14 stable Be stars (the 12 from the survey crossmatch plus α Aqr and δ Oph) have a radial density exponent confirmed to be smaller than 3.5 indicates that there is a factor missing in the power-law steady state solution of the VDD.

One possibility is that the disk is subject to thermal effects we are not considering in the steady state formulation when we assume an isothermal disk. This problem was studied by Carciofi and Bjorkman (2008) by solving the non-isothermal viscous diffusion problem in the VDD formalism. The authors find that the effective slope of the disk, in this case, ranges between 2 and 3 for a radius $1 < r < 3 R_{eq}$, and between 3 and 3.5 for $r \leq 3 R_{eq}$. However, these strong effects are only seen for very dense disks. The possibility of a non-isothermal disk was investigated for the case of β CMi, but found to be much too small to cause such changes in the structure of the disk, given its low density (Klement et al., 2015). The denser disks of the other target stars could be affected by non-isothermal effects more strongly, leading to the observed effect on the density slope.

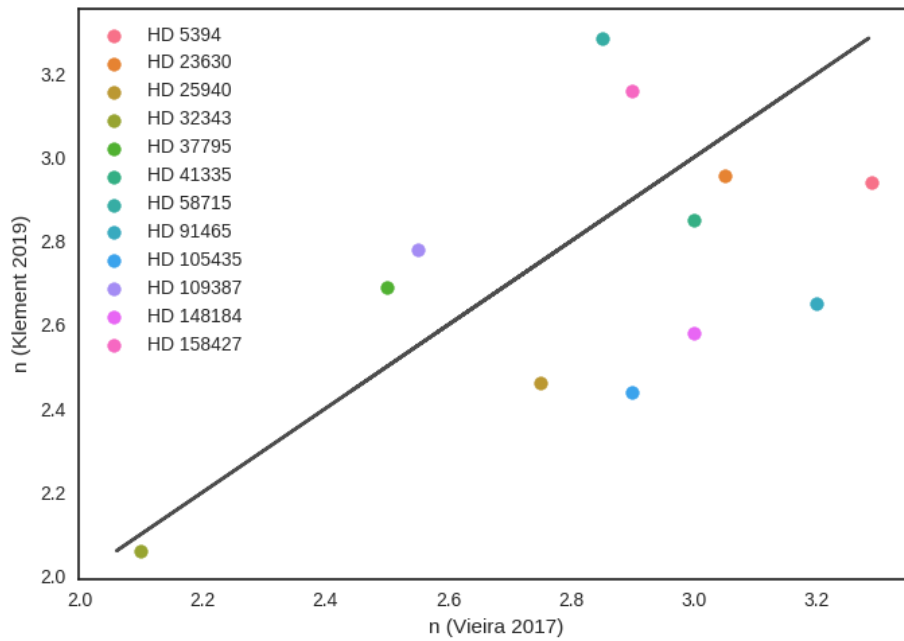


Figure 5.2: Comparing the mean values of n derived by the surveys of Vieira et al. (2017) and Klement et al. (2019).

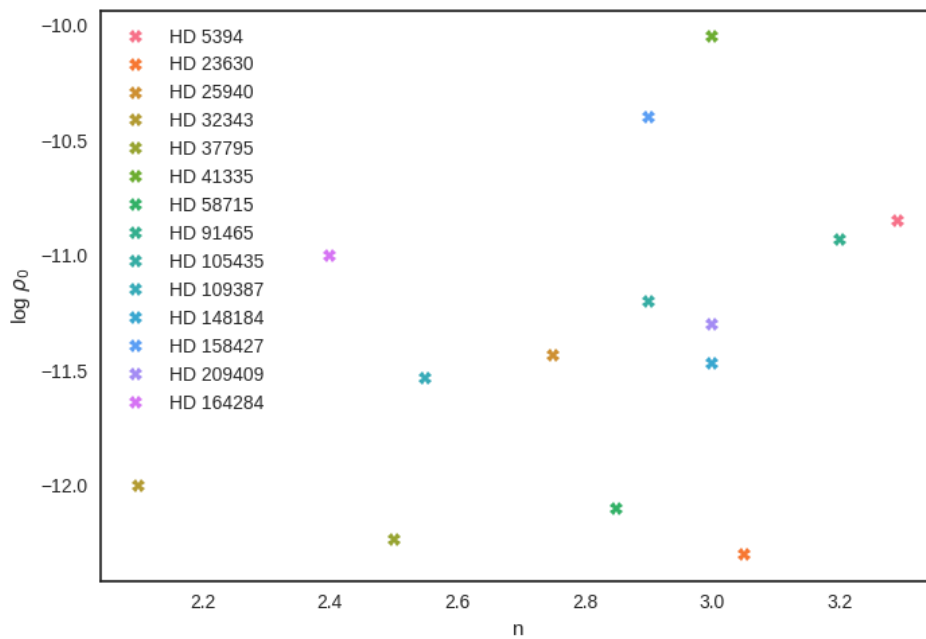


Figure 5.3: Comparison of the values of n and $\log \rho_0$ found by Vieira et al. (2017) for all 14 stars in our sample.

It is also possible that the viscosity parameter of the disk, α , is variable with radius. From Eq. 1.10, we see that α and the temperature of the disk (which is part of c_s) have analogous effect on the density, so much that they can be considered a combined parameter αT . However, when we consider the volume density $\rho \propto \Sigma/H$, the scale height H has an individual dependence on the temperature, so a variable T would influence the density differently. All in all, if either α or the temperature vary with the radius of the disk, their effect on its density structure could lead to an $n \leq 3.5$. However, this needs still to be further verified. Furthermore, to date the only solid evidence of a radially varying α was found in the Be stars: 28 CMa (Ghoreyshi and Carciofi 2019, priv. comm.), but in that case α is *growing* with radius, i.e., the reverse behavior necessary to accommodate the n results seen on our sample. Fig. 5.3 investigates if there is any significant correlation between ρ_0 and n that could indicate non-isothermality in the disk. We find a weak positive correlation with a Pearson index of 0.39, once again the opposite of the behaviour expected if it were to explain the variation of n .

Yet another possibility arises from the high incidence of SED turn-down and therefore binarity recently found among Be stars, strengthened by the conclusion of Klement et al. (2019)'s work that suggests all Be stars are binaries. A consequence of binarity is the accumulation effect: an accumulation of matter in outer region of the disk due to the resonant torque caused by the companion. This pilfers some angular momentum from the disk, leading to a gentler, less steep fall-off of density as the radius increases (Okazaki et al. 2002, Panoglou et al. 2016). As all 14 stars from our sample shown signs of SED turn-down or are confirmed binaries, this hypothesis is worth investigating.

The nature of the companions was not confirmed in Klement et al. (2019) beyond the fact that they are invisible to the observables analysed, which indicates they are faint stars. It is also more likely that they are main sequence or sub dwarf stars, as cool G-, M-, or K- giant would dominate the spectra in the infrared region, what is not observed in the sample (Oudmaijer and Parr, 2010). In Panoglou et al. (2016)'s analysis, for their reference system with a primary with a mass of $11.2 M_\odot$ and radius of $5.5 R_\odot$ and binary mass ratio of $q = 0.08$, the torque of the companion is strong enough to lead to a measurable accumulation effect when the viscosity of the disk $\alpha < 0.6$, the orbital separation is $< 25 R_{eq}$ and the period of the orbit is < 55 days. As the mass ratio increases, the accumulation effect also becomes stronger. As such, in order to answer for the $n \leq 3.0$ trend we see in

our sample, the Be stars would need to have a close companion, in an orbit of less than a hundred days. The companion could be a sdO or sdB star, as their mass range of 0.40 - 0.55 M_{\odot} (Zhang et al., 2010) culminates in mass ratios $0.02 < q < 0.19$ for the range of B stars masses. Perhaps the combined effects of accumulation of matter and non-isothermal viscous diffusion may be enough to explain the slope results. In either case, our findings pave the way for future developments on the VDD theory.

Conclusions and Future Perspectives

Determination of fundamental parameters of stars is not straightforward: it usually depends on a combination of different types of observations and theoretical evolutionary models. The case is even more troublesome for peculiar stars such as Be stars, whose high rotation rates and circumstellar disk lead to intricate effects on the observables and still unclear influence on their evolution along the main sequence (Sec. 1.4). With these issues in mind, our research group calculated a grid of models for Be stars using the radiative transfer code HDUST (Sec. 2.2), specifically designed to account for the effects of their high rotational speeds, all in the Viscous Decretion Disk model framework (Sec. 1.4.1). Using this grid, called BeAtlas (Sec. 3.1), the modern Monte Carlo Markov Chain implementation EMCEE (Sec. 2.3) and the evolutionary models of the Geneva group, Mota (2019) in his PhD thesis (with aid from pos-doc R. Vieira and myself) developed BEMCEE (Sec. 3.2), a complete tool to unveil the essential parameters of Be stars and their disks: mass, rotation rate, age, base density of the disk, radial density exponent, disk radius, inclination, distance and extinction.

Here we present a study of the Be star α Col using BEMCEE and BeAtlas, along with UV spectroscopy, photometry, and polarimetry data. α Col is a stable Be star, showing little variation in its observables since it was classified as a Be star in the 19th century, an indication that it has not undergone any process of disk dissipation or build up in over a hundred years, and, furthermore, has shown an extraordinarily constant disk mass injection rate. The final results for our parameter determinations are in Table 5.1. α Col is a $\sim 4.66 M_{\odot}$ star, very evolved, and rotating at 74% of its critical velocity. The system is seen at an inclination of approximately 40° . The disk is tenuous and has a density exponent of 2.5, less steep than what is expected by VDD theory for a stable Be

star such as α Col. The parameters found using SED data, specially the inclination and base density of the disk, match the ones derived by the polarimetry determination, even though the two observables probe different physical phenomena. Our methodology also allows for the correlations between the parameters to be evaluated, a remarkable boon of a Bayesian-MCMC approach.

We note that the disk of α Col is truncated at $20 R_{eq}$, which indicates the presence of a binary companion, that unfortunately could not be detected in our investigation of radial velocity and V/R variations of the H α spectra. α Col joins an ever growing list of Be stars with detected SED turndown. Klement et al. (2019) tentatively suggests their sample of new found Be stars with SED turndowns to be considered Be+sdOB candidates. Thus, we also submit α Col as a Be+sdOB candidate. This statistic greatly strengthens the old and for a long time discredited scenario that all Be stars may be the end result of binary mass transfer systems.

Our finding that the radial exponent of the disk does not match the expected value for steady state Be stars of $n = 3.5$ is also of interest. For all stable Be stars analysed individually with BEMCEE and BeAtlas so far (*o* Aqr, α Ara, 66 Oph, and β CMi), the values found for n are below or equal to 3.0. Crossmatching the results of the surveys of Vieira et al. (2017) and Klement et al. (2019), we find that all 12 Be stars that were part of both studies show $n \leq 3.5$ consistently. While this trend may be the result of non-isothermal or viscous effects in the outer disk, it is also possible that it is a result of the accumulation effect present in binary Be stars. Once again, the binarity can explain a new tendency found in Be star surveys.

In order to confirm the seemingly expanding role binary companions play in Be physics, our group together with Prof. Carol Jones and her students at the University of Western Ontario (UWO) developed an interface between the smoothed particle hydrodynamics (SPH) code used in Okazaki et al. (2002), Panoglou et al. (2016) and Cyr et al. (2017), and HDUST, so we are now able to calculate the observables using the complex SPH simulated density as input. My FAPESP-BEPE stay at UWO with Prof. Jones and her group had the testing of this interface as the main focus. Future collaborative projects include a high resolution SPH modelling of α Col, which might provide us with further clues as to the nature of the companion and its orbital parameters, as well as allow us to explore the behaviour of n , and whether the accumulation effect can indeed account for this shallow

profile or if non-isothermal effects and/or a variable α are more likely to be the culprit. We will also add the H α line to BEMCEE in the following months.

All in all, our work provides another successful test both for the VDD and for the BEMCEE package and the BeAtlas grid, completely characterizing the Be star α Col, our results providing new insight into the mechanics of Be stars and their circumstellar disks.

Bibliography

- Arcos C., Kanaan S., Chávez J., Vanzi L., Araya I., Curé M., Stellar parameters and H α line profile variability of Be stars in the BeSOS survey, *MNRAS*, 2018, vol. 474, p. 5287
- Baade D., Pigulski A., Rivinius T., Carciofi A. C., Panoglou D., Ghoreyshi M. R., Handler G., Kuschnig R., Moffat A. F. J., Pablo H., Short-term variability and mass loss in Be stars. III. BRITE and SMEI satellite photometry of 28 Cygni, *A&A*, 2018, vol. 610, p. A70
- Baade D., Pigulski A., Rivinius T., Wang L., Martayan C., Handler G., Panoglou D., Carciofi A. C., Kuschnig R., Mehner A., Short-term variability and mass loss in Be stars. IV. Two groups of closely spaced, approximately equidistant frequencies in three decades of space photometry of ν Puppis (B7-8 IIIe), *A&A*, 2018, vol. 620, p. A145
- Baade D., Rivinius T., Pigulski A., Carciofi A. C., Martayan C., Moffat A. F. J., Wade G. A., Weiss W. W., Grunhut J., Handler G., Kuschnig R., Mehner A., Pablo H., Popowicz A., Rucinski S., Whittaker G., Short-term variability and mass loss in Be stars. I. BRITE satellite photometry of η and μ Centauri, *A&A*, 2016, vol. 588, p. A56
- Balbus S. A., Hawley J. F., A powerful local shear instability in weakly magnetized disks. I - Linear analysis. II - Nonlinear evolution, *ApJ*, 1991, vol. 376, p. 214
- Benacquista M. J., Downing J. M. B., Relativistic Binaries in Globular Clusters, *Living Reviews in Relativity*, 2013, vol. 16, p. 4
- Bijaoui A., Doazan V., Analysis of rapid variations in the spectra of alpha Col by cross correlation., *A&A*, 1979, vol. 73, p. 285

- Bjorkman J. E., Circumstellar Disks. In *Stellar Atmospheres: Theory and Observations* , vol. 497 of *Lecture Notes in Physics*, Berlin Springer Verlag, 1997, p. 239
- Bjorkman J. E., Carciofi A. C., Modeling the Structure of Hot Star Disks. In *The Nature and Evolution of Disks Around Hot Stars* , vol. 337 of *Astronomical Society of the Pacific Conference Series*, 2005, p. 75
- Bjorkman J. E., Cassinelli J. P., Equatorial Disk Formation around Rotating Stars Due to Ram Pressure Confinement by the Stellar Wind, *ApJ*, 1993, vol. 409, p. 429
- Bjorkman K. S., Miroshnichenko A. S., McDavid D., Pogrosheva T. M., A Study of π Aquarii during a Quasi-normal Star Phase: Refined Fundamental Parameters and Evidence for Binarity, *ApJ*, 2002, vol. 573, p. 812
- Cannon A. J., Pickering E. C., The Henry Draper catalogue : 4h, 5h and 6h, *Annals of Harvard College Observatory*, 1918, vol. 92, p. 1
- Carciofi A. C., The circumstellar discs of Be stars. In *IAU Symposium* , vol. 272 of *IAU Symposium*, 2011, p. 325
- Carciofi A. C., Bjorkman J. E., Non-LTE Monte Carlo Radiative Transfer. I. The Thermal Properties of Keplerian Disks around Classical Be Stars, *ApJ*, 2006, vol. 639, p. 1081
- Carciofi A. C., Bjorkman J. E., Non-LTE Monte Carlo Radiative Transfer. II. Nonisothermal Solutions for Viscous Keplerian Disks, *ApJ*, 2008, vol. 684, p. 1374
- Carciofi A. C., Bjorkman J. E., Otero S. A., Okazaki A. T., Štefl S., Rivinius T., Baade D., Haubois X., The First Determination of the Viscosity Parameter in the Circumstellar Disk of a Be Star, *ApJ*, 2012, vol. 744, p. L15
- Carciofi A. C., Miroshnichenko A. S., Kusakin A. V., Bjorkman J. E., Bjorkman K. S., Marang F., Kuratov K. S., García-Lario P., Calderón J. V. P., Fabregat J., Magalhães A. M., Properties of the δ Scorpii Circumstellar Disk from Continuum Modeling, *ApJ*, 2006, vol. 652, p. 1617
- Carciofi A. C., Okazaki A. T., Le Bouquin J.-B., Štefl S., Rivinius T., Baade D., Bjorkman J. E., Hummel C. A., Cyclic variability of the circumstellar disk of the Be star ζ Tauri. II. Testing the 2D global disk oscillation model, *A&A*, 2009, vol. 504, p. 915

-
- Casares J., Negueruela I., Ribó M., Ribas I., Paredes J. M., Herrero A., Simón-Díaz S., A Be-type star with a black-hole companion, *Nature*, 2014, vol. 505, p. 378
- Chauville J., Zorec J., Ballereau D., Morrell N., Cidale L., Garcia A., High and intermediate-resolution spectroscopy of Be stars 4481 lines, *A&A*, 2001, vol. 378, p. 861
- Chini R., Hoffmeister V. H., Nasserri A., Stahl O., Zinnecker H., A spectroscopic survey on the multiplicity of high-mass stars, *MNRAS*, 2012, vol. 424, p. 1925
- Clark J. S., Steele I. A., Fender R. P., Radio observations of IRAS-selected Southern hemisphere classical Be stars, *MNRAS*, 1998, vol. 299, p. 1119
- Cannon Smith R., Cataclysmic Variables, arXiv e-prints, 2007, pp astro-ph/0701654
- Cox A. N., Allen's astrophysical quantities, 2000
- Coyne G. V., Polarization in the emission lines of Be stars., *A&A*, 1976, vol. 49, p. 89
- Cranmer S. R., Dynamical Models of Winds from Rotating Hot Stars, Bartol Research Institute, University of Delaware, 1996, Ph.D. Thesis
- Cucchiario A., Macau-Hercot D., Jaschek M., Jaschek C., Spectral classification from the ultraviolet line features of S2/68 spectra. II. Late B-type stars., *Astronomy and Astrophysics Supplement Series*, 1977, vol. 30, p. 71
- Cutri R. M., et al. VizieR Online Data Catalog: AllWISE Data Release (Cutri+ 2013), *VizieR Online Data Catalog*, 2014, vol. 2328
- Cyr I. H., Jones C. E., Panoglou D., Carciofi A. C., Okazaki A. T., Be discs in binary systems - II. Misaligned orbits, *MNRAS*, 2017, vol. 471, p. 596
- Dachs J., Eichendorf W., Schleicher H., Schmidt-Kaler T., Stift M., Tug H., Photoelectric scanner measurements of Balmer emission line profiles for southern Be stars. II - A survey for variations, *A&AS*, 1981, vol. 43, p. 427
- David T. J., Hillenbrand L. A., The Ages of Early-type Stars: Strömgren Photometric Methods Calibrated, Validated, Tested, and Applied to Hosts and Prospective Hosts of Directly Imaged Exoplanets, *ApJ*, 2015, vol. 804, p. 146

- de Almeida E. S. G., Meilland A., Domiciano de Souza A., Stee P., Mourard D., Nrdetto N., Ligi R., Tallon-Bosc I., Faes D. M., Mota B. C., Carciofi A. C., Visible and near-infrared spectro-interferometric analysis of the edge-on Be star α Aquarii, 2019
- de Freitas Pacheco J. A., Steiner J. E., The spectrum of Cyg X-1 — A theoretical model, *Ap&SS*, 1976, vol. 39, p. 487
- Doi Y., Takita S., Ootsubo T., Arimatsu K., Tanaka M., Kitamura Y., Kawada M., Matsuura S., Nakagawa T., Morishima T., Hattori M., Komugi S., White G. J., Ikeda N., Kato D., Chinone Y., Etxaluze M., Cypriano E. F., The AKARI far-infrared all-sky survey maps, *PASJ*, 2015, vol. 67, p. 50
- Domiciano de Souza A., Hadjara M., Vakili F., Bendjoya P., Millour F., Abe L., Carciofi A. C., Faes D. M., Kervella P., Lagarde S., Marconi A., Monin J.-L., Niccolini G., Petrov R. G., Weigelt G., Beyond the diffraction limit of optical/IR interferometers. I. Angular diameter and rotation parameters of Achernar from differential phases, *A&A*, 2012, vol. 545, p. A130
- Dougherty S. M., Waters L. B. F. M., Burki G., Cote J., Cramer N., van Kerkwijk M. H., Taylor A. R., Near-IR excess of Be stars., *A&A*, 1994, vol. 290, p. 609
- Duflot M., Figon P., Meyssonier N., Vitesses radiales. Catalogue WEB: Wilson Evans Batten. Subtitle: Radial velocities: The Wilson-Evans-Batten catalogue., *Astronomy and Astrophysics Supplement Series*, 1995, vol. 114, p. 269
- Dulaney N. A., Richardson N. D., Gerhartz C. J., Bjorkman J. E., Bjorkman K. S., Carciofi A. C., Klement R., Wang L., Morrison N. D., Bratcher A. D., Greco J. J., Hardegree-Ullman K. K., Lembryk L., Oswald W. L., Trucks J. L., A Spectroscopic Orbit for the Late-type Be Star β CMi, *ApJ*, 2017, vol. 836, p. 112
- Ekström S., Meynet G., Maeder A., Barblan F., Evolution towards the critical limit and the origin of Be stars, *A&A*, 2008, vol. 478, p. 467
- ESA ed., 1997 The HIPPARCOS and TYCHO catalogues. Astrometric and photometric star catalogues derived from the ESA HIPPARCOS Space Astrometry Mission vol. 1200 of ESA Special Publication

-
- Espinosa Lara F., Rieutord M., Gravity darkening in rotating stars, *A&A*, 2011, vol. 533, p. A43
- Fitzpatrick E. L., Massa D., Determining the Physical Properties of the B Stars. I. Methodology and First Results, *ApJ*, 1999, vol. 525, p. 1011
- Foreman-Mackey D., Hogg D. W., Lang D., Goodman J., emcee: The MCMC Hammer, *PASP*, 2013, vol. 125, p. 306
- Frémat Y., Zorec J., Hubert A.-M., Floquet M., Effects of gravitational darkening on the determination of fundamental parameters in fast-rotating B-type stars, *A&A*, 2005, vol. 440, p. 305
- Gaia Collaboration Clementini G., Eyer L., Ripepi V., Marconi M., Muraveva T., Garofalo A., Sarro L. M., Palmer M., Luri X., et al. Gaia Data Release 1. Testing parallaxes with local Cepheids and RR Lyrae stars, *A&A*, 2017, vol. 605, p. A79
- Gelman A., Roberts G. O., Gilks W. R., Efficient Metropolis jumping rules, 1996, pp 599–607
- Georgy C., Ekström S., Granada A., Meynet G., Mowlavi N., Eggenberger P., Maeder A., Populations of rotating stars. I. Models from 1.7 to 15 M_{\odot} at $Z = 0.014$, 0.006, and 0.002 with Ω/Ω_{crit} between 0 and 1, *A&A*, 2013, vol. 553, p. A24
- Ghoreyshi M. R., Carciofi A. C., Rímulo L. R., Vieira R. G., Faes D. M., Baade D., Bjorkman J. E., Otero S., Rivinius T., The life cycles of Be viscous decretion discs: The case of ω CMa, *MNRAS*, 2018, vol. 479, p. 2214
- Gontcharov G. A., Pulkovo Compilation of Radial Velocities for 35 495 Hipparcos stars in a common system, *Astronomy Letters*, 2006, vol. 32, p. 759
- Goodman J., Weare J., Ensemble samplers with affine invariance, *Communications in Applied Mathematics and Computational Science*, 2010, vol. 5, p. 65
- Granada A., Ekström S., Georgy C., Kr̄t̄icka J., Owocki S., Meynet G., Maeder A., Populations of rotating stars. II. Rapid rotators and their link to Be-type stars, *A&A*, 2013, vol. 553, p. A25

- Grundstrom E., Hot Stars With Disks. In American Astronomical Society Meeting Abstracts , vol. 39 of Bulletin of the American Astronomical Society, 2007, p. 871
- Halonen R. J., Jones C. E., On the Intrinsic Continuum Linear Polarization of Classical Be Stars: The Effects of Metallicity and One-armed Density Perturbations, *ApJS*, 2013, vol. 208, p. 3
- Hanuschik R. W., On the structure of Be star disks., *A&A*, 1996, vol. 308, p. 170
- Hastings W. K., Monte Carlo Sampling Methods Using Markov Chains and Their Applications, *Biometrika*, 1970, vol. 57, p. 97
- Haubois X., Carciofi A. C., Rivinius T., Okazaki A. T., Bjorkman J. E., Dynamical Evolution of Viscous Disks around Be Stars. I. Photometry, *ApJ*, 2012, vol. 756, p. 156
- Hiltner W. A., Garrison R. F., Schild R. E., MK Spectral Types for Bright Southern OB Stars, *ApJ*, 1969, vol. 157, p. 313
- Høg E., Fabricius C., Makarov V. V., Urban S., Corbin T., Wycoff G., Bastian U., Schwekendiek P., Wicenec A., The Tycho-2 catalogue of the 2.5 million brightest stars, *A&A*, 2000, vol. 355, p. L27
- Hogg D. W., Foreman-Mackey D., Data Analysis Recipes: Using Markov Chain Monte Carlo, *ApJS*, 2018, vol. 236, p. 11
- Houk N., Michigan Catalogue of Two-dimensional Spectral Types for the HD stars. Volume 3. Declinations -40.0 to -26.0., 1982
- Huang W., Gies D. R., McSwain M. V., A Stellar Rotation Census of B Stars: From ZAMS to TAMS, *ApJ*, 2010, vol. 722, p. 605
- Hummel W., Dachs J., Non-coherent scattering in vertically extended Be star disks - Winebottle-type emission-line profiles, *A&A*, 1992, vol. 262, p. L17
- Jaschek C., Jaschek M., Kucwicz B., A Survey of Southern Be Stars, *Zeitschrift für Astrophysik*, 1964, vol. 59, p. 108
- Jaschek M., Jaschek C., Malaroda S., The spectra of some Be stars., *A&A*, 1969, vol. 3, p. 485

-
- Jaschek M., Slettebak A., Jaschek C., Be star terminology., Be Star Newsletter, 1981, vol. 4, p. 9
- Jones C. E., Sigut T. A. A., Porter J. M., The circumstellar envelopes of Be stars: viscous disc dynamics, MNRAS, 2008, vol. 386, p. 1922
- Jones C. E., Tycner C., Sigut T. A. A., Benson J. A., Hutter D. J., A Parameter Study of Classical Be Star Disk Models Constrained by Optical Interferometry, ApJ, 2008, vol. 687, p. 598
- King A. R., Pringle J. E., Livio M., Accretion disc viscosity: how big is alpha?, MNRAS, 2007, vol. 376, p. 1740
- Klement R., Carciofi A. C., Rivinius T., Ignace R., Matthews L. D., Torstensson K., Gies D., Vieira R. G., Richardson N. D., Domiciano de Souza A., Bjorkman J. E., Hallinan G., Faes D. M., Mota B., Gullingsrud A. D., de Breuck C., Prevalence of SED turndown among classical Be stars: Are all Be star close binaries?, 2019
- Klement R., Carciofi A. C., Rivinius T., Matthews L. D., Vieira R. G., Ignace R., Bjorkman J. E., Mota B. C., Faes D. M., Bratcher A. D., Curé M., Štefl S., Revealing the structure of the outer disks of Be stars, ArXiv e-prints, 2017
- Klement R., Carciofi A. C., Rivinius T., Panoglou D., Vieira R. G., Bjorkman J. E., Štefl S., Tycner C., Faes D. M., Korčáková D., Müller A., Zavala R. T., Curé M., Multitechnique testing of the viscous accretion disk model. I. The stable and tenuous disk of the late-type Be star β CMi, A&A, 2015, vol. 584, p. A85
- Krtićka J., Owocki S. P., Meynet G., Mass and angular momentum loss via accretion disks, A&A, 2011, vol. 527, p. A84
- Kurtz D. W., Shibahashi H., Murphy S. J., Bedding T. R., Bowman D. M., A unifying explanation of complex frequency spectra of γ Dor, SPB and Be stars: combination frequencies and highly non-sinusoidal light curves, MNRAS, 2015, vol. 450, p. 3015
- Lee U., Osaki Y., Saio H., Viscous accretion discs around Be stars, MNRAS, 1991, vol. 250, p. 432

- Levenhagen R. S., Leister N. V., Spectroscopic analysis of southern B and Be stars, *MNRAS*, 2006, vol. 371, p. 252
- Lynden-Bell D., Galactic Nuclei as Collapsed Old Quasars, *Nature*, 1969, vol. 223, p. 690
- Lynden-Bell D., Pringle J. E., The evolution of viscous discs and the origin of the nebular variables., *MNRAS*, 1974, vol. 168, p. 603
- Magalhães A. M., Rodrigues C. V., Margoniner V. E., Pereyra A., Heathcote S., High Precision CCD Imaging Polarimetry. In *Polarimetry of the Interstellar Medium* , vol. 97 of *Astronomical Society of the Pacific Conference Series*, 1996, p. 118
- Meilland A., Millour F., Kanaan S., Stee P., Petrov R., Hofmann K.-H., Natta A., Perraut K., First spectro-interferometric survey of Be stars. I. Observations and constraints on the disk geometry and kinematics, *A&A*, 2012, vol. 538, p. A110
- Mermilliod J. C., *VizieR Online Data Catalog: Homogeneous Means in the UBV System (Mermilliod 1991)*, *VizieR Online Data Catalog*, 1997, vol. 2168
- Merrill P. W., Burwell C. G., *Catalogue and Bibliography of Stars of Classes B and A whose Spectra have Bright Hydrogen Lines*, *ApJ*, 1933, vol. 78, p. 87
- Metropolis N., Rosenbluth A., Rosenbluth M., Teller A., Teller E., Equations of state calculations by fast computing machines, *Journal of Chemical Physics*, 1953, vol. 21, p. 1087
- Meynet G., Maeder A., *Stellar evolution with rotation. V. Changes in all the outputs of massive star models*, *A&A*, 2000, vol. 361, p. 101
- Miroshnichenko A. S., Fabregat J., Bjorkman K. S., Knauth D. C., Morrison N. D., Tarasov A. E., Reig P., Negueruela I., Blay P., Spectroscopic observations of the δ Scorpii binary during its recent periastron passage, *A&A*, 2001, vol. 377, p. 485
- Molnar M. R., *The Helium-Weak Stars*, *ApJ*, 1972, vol. 175, p. 453
- Montesinos M., *Review: Accretion Disk Theory*, arXiv e-prints, 2012, p. arXiv:1203.6851
- Mota B. C., *BeAtlas: A grid of synthetic spectra for Be stars*, IAG-USP <ORCID>0000-0002-7851-4242</ORCID>, 2019, Ph.D. Thesis

-
- Mota B. C., Carciofi A. C., Faes D. M., Vieira R. G., Ghoreyshi M. R., Rímulo L. R., Figueiredo A. L., Seriacopi D. B., C. R. A., , 2019
- Okazaki A. T., Long-Term V/R Variations of Be Stars Due to Global One-Armed Oscillations of Equatorial Disks, PASJ, 1991, vol. 43, p. 75
- Okazaki A. T., Viscous Transonic Accretion in Disks of Be Stars, PASJ, 2001, vol. 53, p. 119
- Okazaki A. T., Theory vs. Observation of Circumstellar Disks and Their Formation. In Active OB-Stars: Laboratories for Stellar and Circumstellar Physics , vol. 361 of Astronomical Society of the Pacific Conference Series, 2007, p. 230
- Okazaki A. T., Bate M. R., Ogilvie G. I., Pringle J. E., Viscous effects on the interaction between the coplanar accretion disc and the neutron star in Be/X-ray binaries, MNRAS, 2002, vol. 337, p. 967
- Oudmaijer R. D., Parr A. M., The binary fraction and mass ratio of Be and B stars: a comparative Very Large Telescope/NACO study, MNRAS, 2010, vol. 405, p. 2439
- Pablo H., Whittaker G. N., Popowicz A., Mochnacki S. M., Kuschnig R., Grant C. C., Moffat A. F. J., Rucinski S. M., Matthews J. M., Schwarzenberg-Czerny A., The BRITe Constellation Nanosatellite Mission: Testing, Commissioning, and Operations, PASP, 2016, vol. 128, p. 125001
- Panoglou D., Carciofi A. C., Vieira R. G., Cyr I. H., Jones C. E., Okazaki A. T., Rivinius T., Be discs in binary systems - I. Coplanar orbits, MNRAS, 2016, vol. 461, p. 2616
- Panoglou D., Faes D. M., Carciofi A. C., Okazaki A. T., Baade D., Rivinius T., Borges Fernandes M., Be discs in coplanar circular binaries: Phase-locked variations of emission lines, MNRAS, 2018, vol. 473, p. 3039
- Pols O. R., Cote J., Waters L. B. F. M., Heise J., The formation of Be stars through close binary evolution, A&A, 1991, vol. 241, p. 419
- Porter J. M., Continuum IR emission of Be star wind-compressed discs., A&A, 1997, vol. 324, p. 597

- Pringle J. E., Accretion discs in astrophysics, *ARA&A*, 1981, vol. 19, p. 137
- Pringle J. E., Rees M. J., Accretion Disc Models for Compact X-Ray Sources, *A&A*, 1972, vol. 21, p. 1
- Quirrenbach A., Bjorkman K. S., Bjorkman J. E., Hummel C. A., Buscher D. F., Armstrong J. T., Mozurkewich D., Elias II N. M., Babler B. L., Constraints on the Geometry of Circumstellar Envelopes: Optical Interferometric and Spectropolarimetric Observations of Seven Be Stars, *ApJ*, 1997, vol. 479, p. 477
- Quirrenbach A., Buscher D. F., Mozurkewich D., Hummel C. A., Armstrong J. T., Maximum-entropy maps of the Be shell star dzeta Tauri from optical long-baseline interferometry., *A&A*, 1994, vol. 283, p. L13
- Raguzova N. V., Popov S. B., Be X-ray binaries and candidates, *Astronomical and Astrophysical Transactions*, 2005, vol. 24, p. 151
- Reig P., Be/X-ray binaries, *Ap&SS*, 2011, vol. 332, p. 1
- Rimmer W. B., The luminosities and parallaxes of 350 stars of spectral type B, *Memoires of the Mount Stromlo Observervatory*, 1930, vol. 2, p. 1
- Rímulo L. R., Carciofi A. C., Vieira R. G., Rivinius T., Faes D. M., Figueiredo A. L., Bjorkman J. E., Georgy C., Ghoreyshi M. R., Soszyński I., The life cycles of Be viscous decretion discs: fundamental disc parameters of 54 SMC Be stars, *MNRAS*, 2018, vol. 476, p. 3555
- Rivinius T., Baade D., Carciofi A. C., Short-term variability and mass loss in Be stars. II. Physical taxonomy of photometric variability observed by the Kepler spacecraft, *A&A*, 2016, vol. 593, p. A106
- Rivinius T., Baade D., Stefl S., Stahl O., Wolf B., Kaufer A., Stellar and circumstellar activity of the Be star MU Centauri. I. Line emission outbursts, *A&A*, 1998, vol. 333, p. 125
- Rivinius T., Baade D., Štefl S., Non-radially pulsating Be stars, *A&A*, 2003, vol. 411, p. 229

-
- Rivinius T., Carciofi A. C., Martayan C., Classical Be stars. Rapidly rotating B stars with viscous Keplerian decretion disks, *A&A Rev.*, 2013, vol. 21, p. 69
- Rivinius T., Štefl S., Baade D., Bright Be-shell stars, *A&A*, 2006, vol. 459, p. 137
- Sana H., de Mink S. E., de Koter A., Langer N., Evans C. J., Gieles M., Gosset E., Izzard R. G., Le Bouquin J.-B., Schneider F. R. N., Binary Interaction Dominates the Evolution of Massive Stars, *Science*, 2012, vol. 337, p. 444
- Secchi A., Schreiben des Herrn Prof. Secchi, Directors der Sternwarte des Collegio Romano, an den Herausgeber, *Astronomische Nachrichten*, 1866, vol. 68, p. 63
- Shafter A. W., Szkody P., Thorstensen J. R., X-ray and optical observations of the ultrashort period dwarf nova SW Ursae Majoris - A likely new DQ Herculis star, *ApJ*, 1986, vol. 308, p. 765
- Shakura N. I., Sunyaev R. A., Black holes in binary systems. Observational appearance., *A&A*, 1973, vol. 24, p. 337
- Sharma S., Markov Chain Monte Carlo Methods for Bayesian Data Analysis in Astronomy, *ARA&A*, 2017, vol. 55, p. 213
- Shklovsky I. S., On the Nature of the Source of X-Ray Emission of Sco XR-1., *ApJ*, 1967, vol. 148, p. L1
- Sigut T. A. A., Jones C. E., The Thermal Structure of the Circumstellar Disk Surrounding the Classical Be Star γ Cassiopeiae, *ApJ*, 2007, vol. 668, p. 481
- Sigut T. A. A., Tycner C., Jansen B., Zavala R. T., The Circumstellar Disk of the Be Star α Aquarii as Constrained by Simultaneous Spectroscopy and Optical Interferometry, *The Astrophysical Journal*, 2015, vol. 814, p. 159
- Silaj J., Jones C. E., Carciofi A. C., Escolano C., Okazaki A. T., Tycner C., Rivinius T., Klement R., Bednarski D., Investigating the Circumstellar Disk of the Be Shell Star δ Librae, *ApJ*, 2016, vol. 826, p. 81
- Skiff B. A., VizieR Online Data Catalog: Catalogue of Stellar Spectral Classifications (Skiff, 2009-2016), *VizieR Online Data Catalog*, 2014, p. B/mk

- Skrutskie M. F., Cutri R. M., Stiening R., Weinberg M. D., Schneider S., Carpenter J. M., Beichman C., Capps R., Chester T., Elias J., Huchra J., Liebert J., Lonsdale C., Monet D. G. e. a., The Two Micron All Sky Survey (2MASS), *AJ*, 2006, vol. 131, p. 1163
- Slettebak A., Spectral types and rotational velocities of the brighter Be stars and A-F type shell stars, *ApJS*, 1982, vol. 50, p. 55
- Sokolov N. A., The determination of T_{eff} of B, A and F main sequence stars from the continuum between 3200 Å and 3600 Å, *A&AS*, 1995, vol. 110, p. 553
- Struve O., On the Origin of Bright Lines in Spectra of Stars of Class B, *ApJ*, 1931, vol. 73, p. 94
- Taylor A. R., Dougherty S. M., Waters L. B. F. M., Bjorkman K. S., A radio survey of IRAS-selected Be stars, *A&A*, 1990, vol. 231, p. 453
- Townsend R. H. D., Owocki S. P., Howarth I. D., Be-star rotation: how close to critical?, *MNRAS*, 2004, vol. 350, p. 189
- Tycner C., Jones C. E., Sigut T. A. A., Schmitt H. R., Benson J. A., Hutter D. J., Zavala R. T., Constraining the Physical Parameters of the Circumstellar Disk of χ Ophiuchi, *ApJ*, 2008, vol. 689, p. 461
- van Bever J., Vanbeveren D., The number of B-type binary mass gainers in general, binary Be stars in particular, predicted by close binary evolution., *A&A*, 1997, vol. 322, p. 116
- van Leeuwen F., Validation of the new Hipparcos reduction, *A&A*, 2007, vol. 474, p. 653
- Vieira R. G., Carciofi A. C., Bjorkman J. E., The pseudo-photosphere model for the continuum emission of gaseous discs, *MNRAS*, 2015, vol. 454, p. 2107
- Vieira R. G., Carciofi A. C., Bjorkman J. E., Rivinius T., Baade D., Rímulo L. R., The life cycles of Be viscous decretion discs: time-dependent modelling of infrared continuum observations, *MNRAS*, 2017, vol. 464, p. 3071
- von Zeipel H., The radiative equilibrium of a slightly oblate rotating star, *MNRAS*, 1924, vol. 84, p. 684

-
- Wang L., Gies D. R., Peters G. J., Detection of Additional Be+sdO Systems from IUE Spectroscopy, *ApJ*, 2018, vol. 853, p. 156
- Waters L. B. F. M., Cote J., Lamers H. J. G. L. M., IRAS observations of Be stars. II - Far-IR characteristics and mass loss rates, *A&A*, 1987, vol. 185, p. 206
- Waters L. B. F. M., van der Veen W. E. C. J., Taylor A. R., Marlborough J. M., Dougherty S. M., The structure of circumstellar discs of Be stars : millimeter observations., *A&A*, 1991, vol. 244, p. 120
- Williams J. P., Cieza L. A., Protoplanetary Disks and Their Evolution, *ARA&A*, 2011, vol. 49, p. 67
- Wood K., Bjorkman K. S., Bjorkman J. E., Deriving the Geometry of Be Star Circumstellar Envelopes from Continuum Spectropolarimetry. I. The Case of ζ Tauri, *ApJ*, 1997, vol. 477, p. 926
- Woods M. L., Spectral types of bright southern stars, *Memoires of the Mount Stromlo Observervatory*, 1955, vol. 12, p. 1
- Zhang X., Chen X., Han Z., The masses of sdB and sdO stars, *Astrophysics and Space Science*, 2010, vol. 329, p. 11
- Zorec J., Briot D., Critical study of the frequency of Be stars taking into account their outstanding characteristics., *A&A*, 1997, vol. 318, p. 443
- Zorec J., Frémat Y., Cidale L., On the evolutionary status of Be stars. I. Field Be stars near the Sun, *A&A*, 2005, vol. 441, p. 235
- Zorec J., Frémat Y., Domiciano de Souza A., Royer F., Cidale L., Hubert A.-M., Semaan T., Martayan C., Cochetti Y. R., Arias M. L., Aidelman Y., Stee P., Critical study of the distribution of rotational velocities of Be stars. I. Deconvolution methods, effects due to gravity darkening, macroturbulence, and binarity, *A&A*, 2016, vol. 595, p. A132
- Zorec J., Royer F., Rotational velocities of A-type stars. IV. Evolution of rotational velocities, *A&A*, 2012, vol. 537, p. A120

Appendix

Appendix A

Additional Data and Plots

Mass	v_{crit}	$v \sin(i)$	i°	T_{eff}	$\log(g)$	$\log(L)$	R_{eq}	$E(B - V)$	Ref
			35 ± 5	12200 ± 122	3.50 ± 0.04		7.00 ± 0.14	0.010	Arcos et al. (2018)
	310	180 ± 2	51	13489.6	3.20		5.8		Meilland et al. (2012)
5 ± 0.5		180 ± 15		14200 ± 400	3.5 ± 0.1	3.07 ± 0.20			Chauville et al. (2001)
				13870 ± 630					Levenhagen and Leister (2006)
4.39 ± 0.07				11830 ± 137		2.9470 ± 0.0290			Sokolov (1995)
5.6 ± 1.1	347 ± 18	199 ± 17	55 ± 13	15540 ± 500	3.71 ± 0.23	3.118 ± 0.06			Zorec and Royer (2012)
	355 ± 23	192 ± 12	44.9 ± 2.1	13695 ± 437	3.559 ± 0.069			0.019 ± 0.017	Zorec et al. (2016)
		186		13146 ± 447	2.97 ± 0.14				Zorec et al. (2005)
									David and Hillenbrand (2015)

Table A.1 - Literature determinations of the stellar parameters of the Be star α Col.

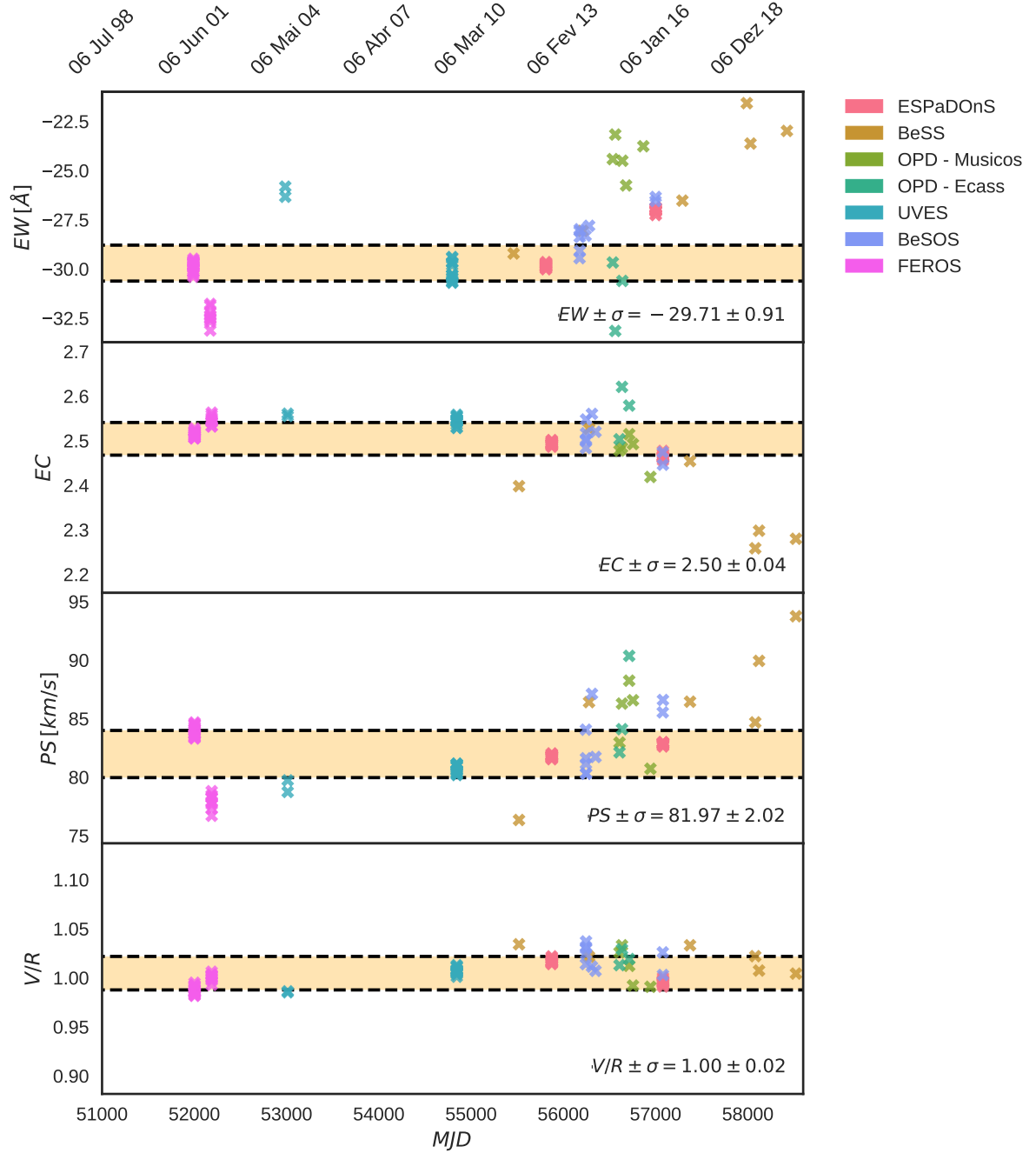


Figure A.1: Measurements for the equivalent width (EW - panel 1), emission over continuum (EC - panel 2), separation between the two emission peaks (PS - panel 3), and violet on red emission (V/R) for our collection of H α spectra summarised in Table 2.3.

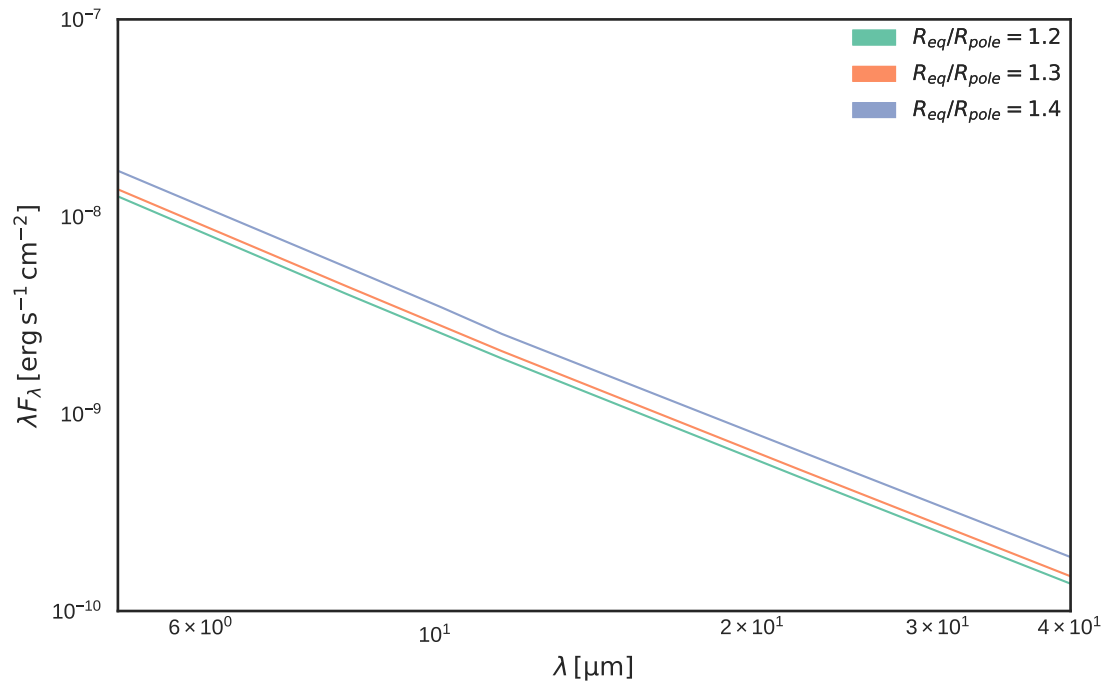


Figure A.2: Effects on the flux caused by changing the rotation rate parameter while maintaining the same central star and disk, on the mid-infrared 5 to 40 μm .

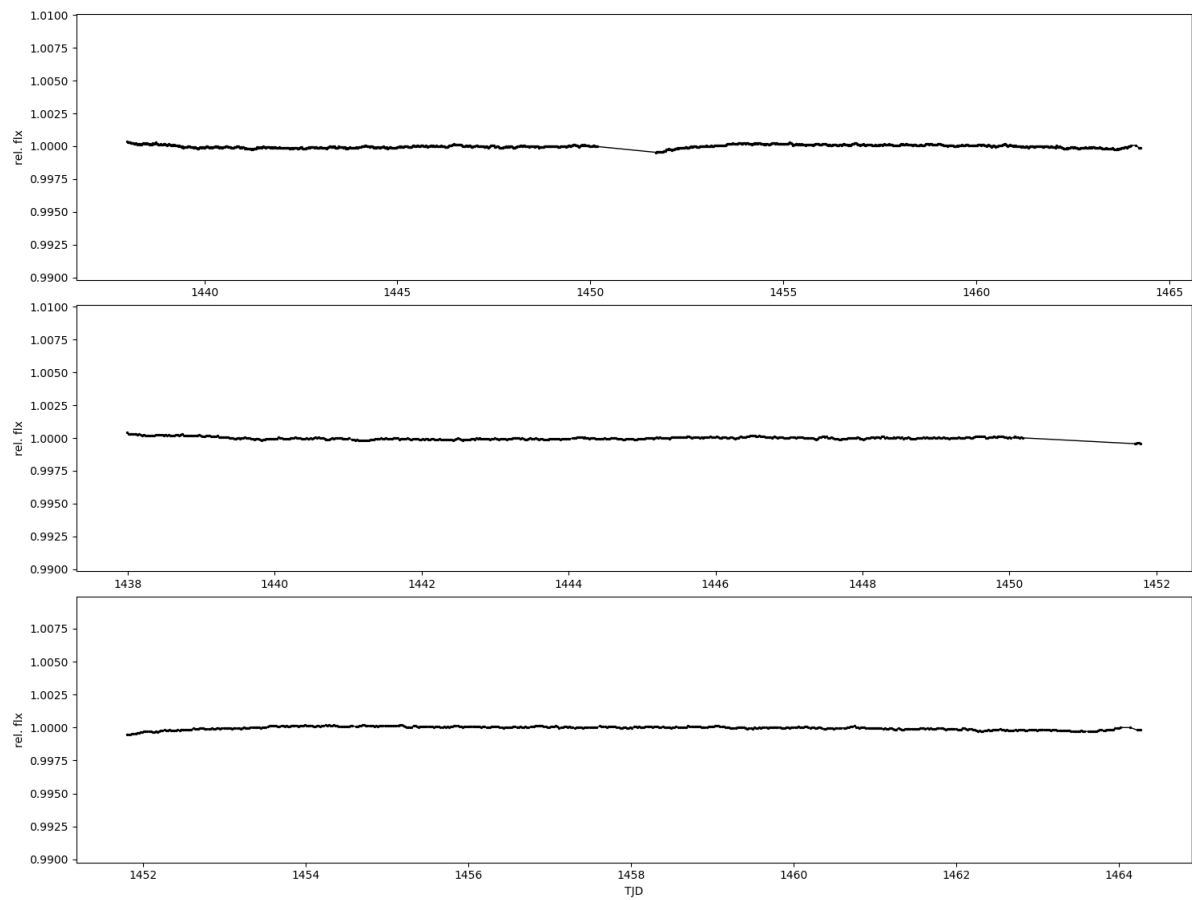


Figure A.3: 1st panel: the 27 days TESS lightcurve for α Col. 2nd and 3rd panels: the first half and second half of the data. A zoom-in from the 1st panel. Courtesy of J. Labadie-Bartz.

Appendix B ---

Trace Plots and Chord Diagrams

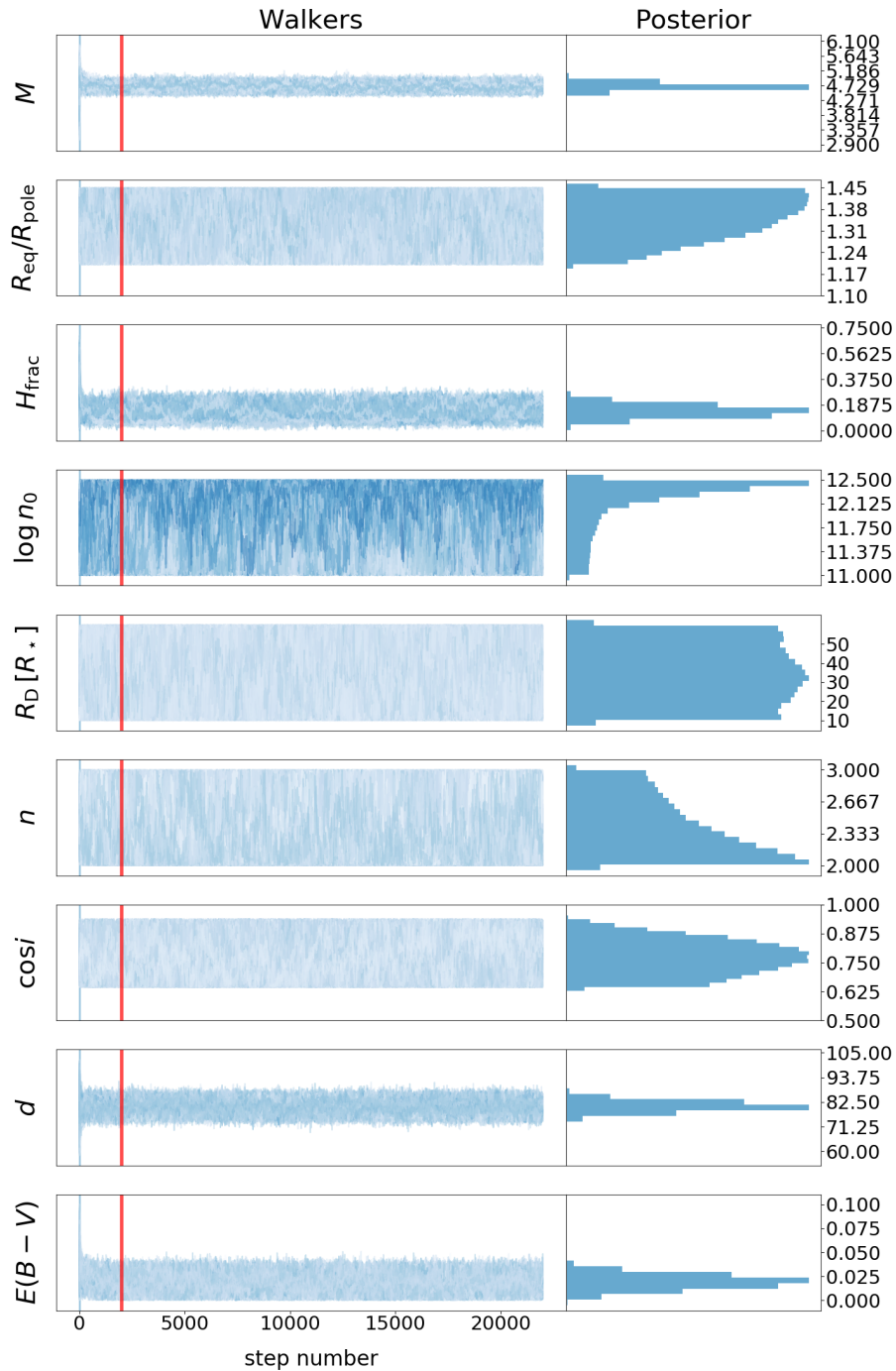


Figure B.1: Trace plot for the BEMCEE result in Fig. 4.1, the red line represents the burn-in phase.

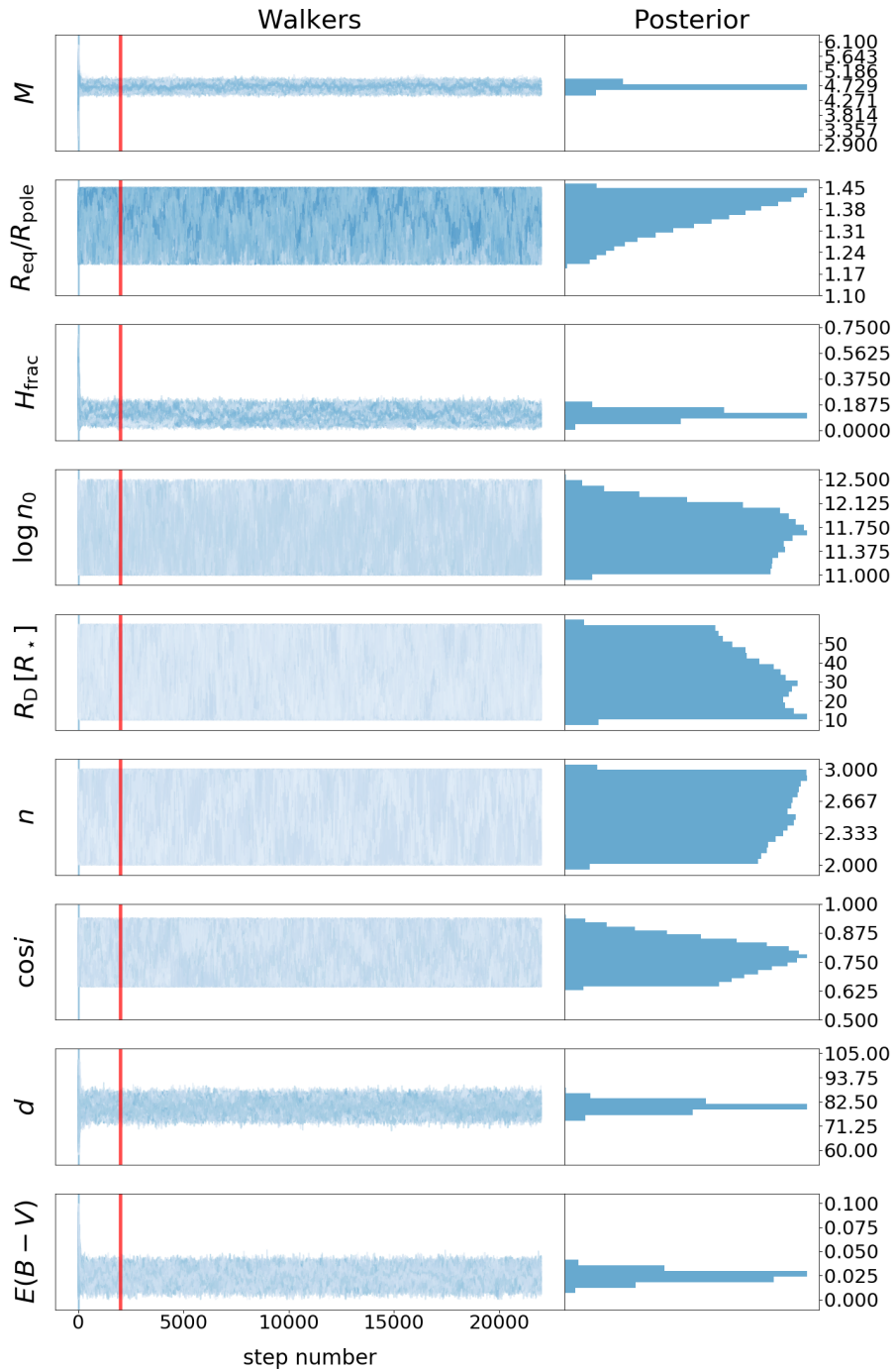


Figure B.2: Trace plot for the BEMCEE result in Fig. 4.2, the red line represents the burn-in phase.

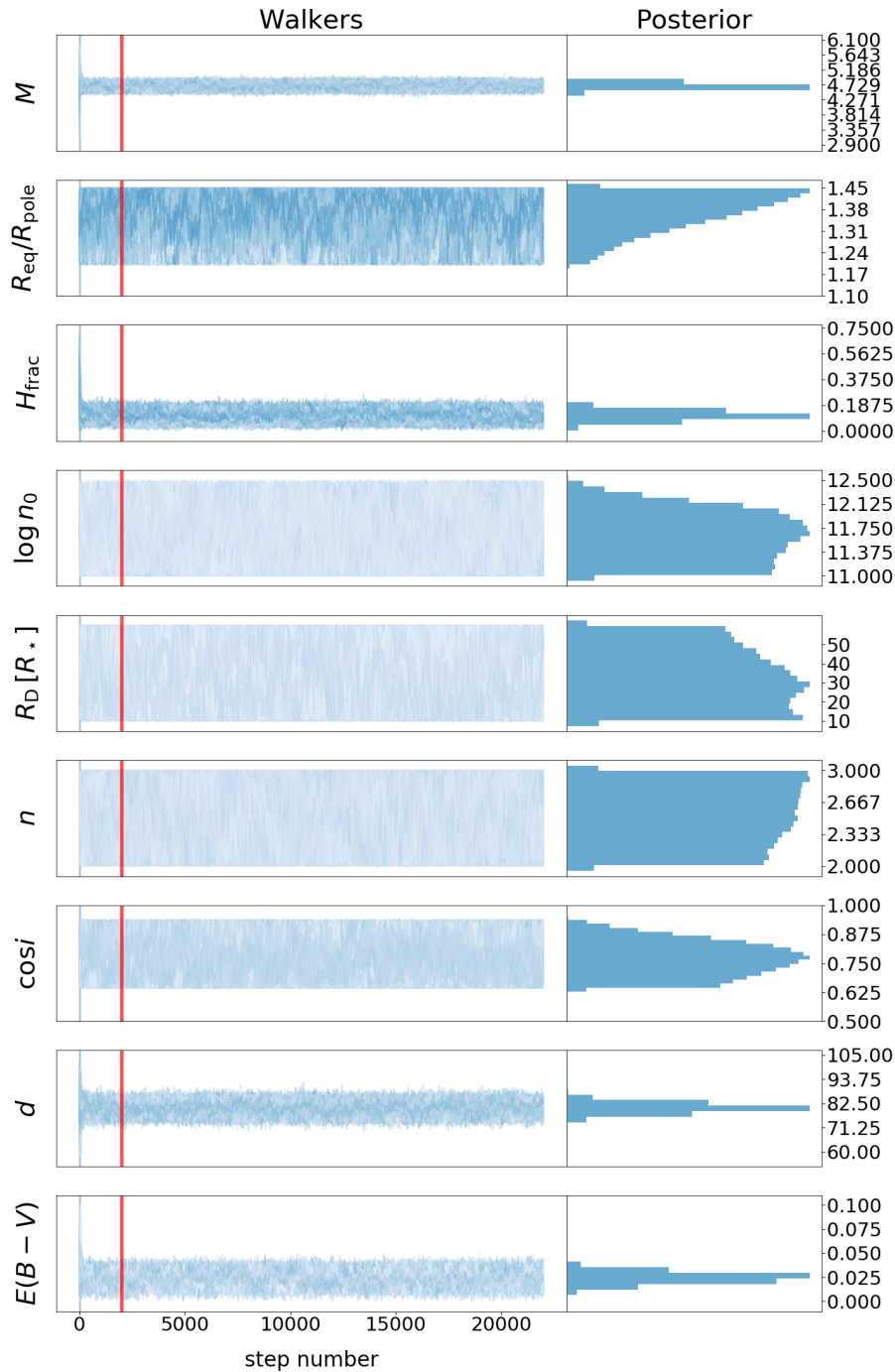


Figure B.3: Trace plot for the BEMCEE result in Fig. 4.3, the red line represents the burn-in phase.

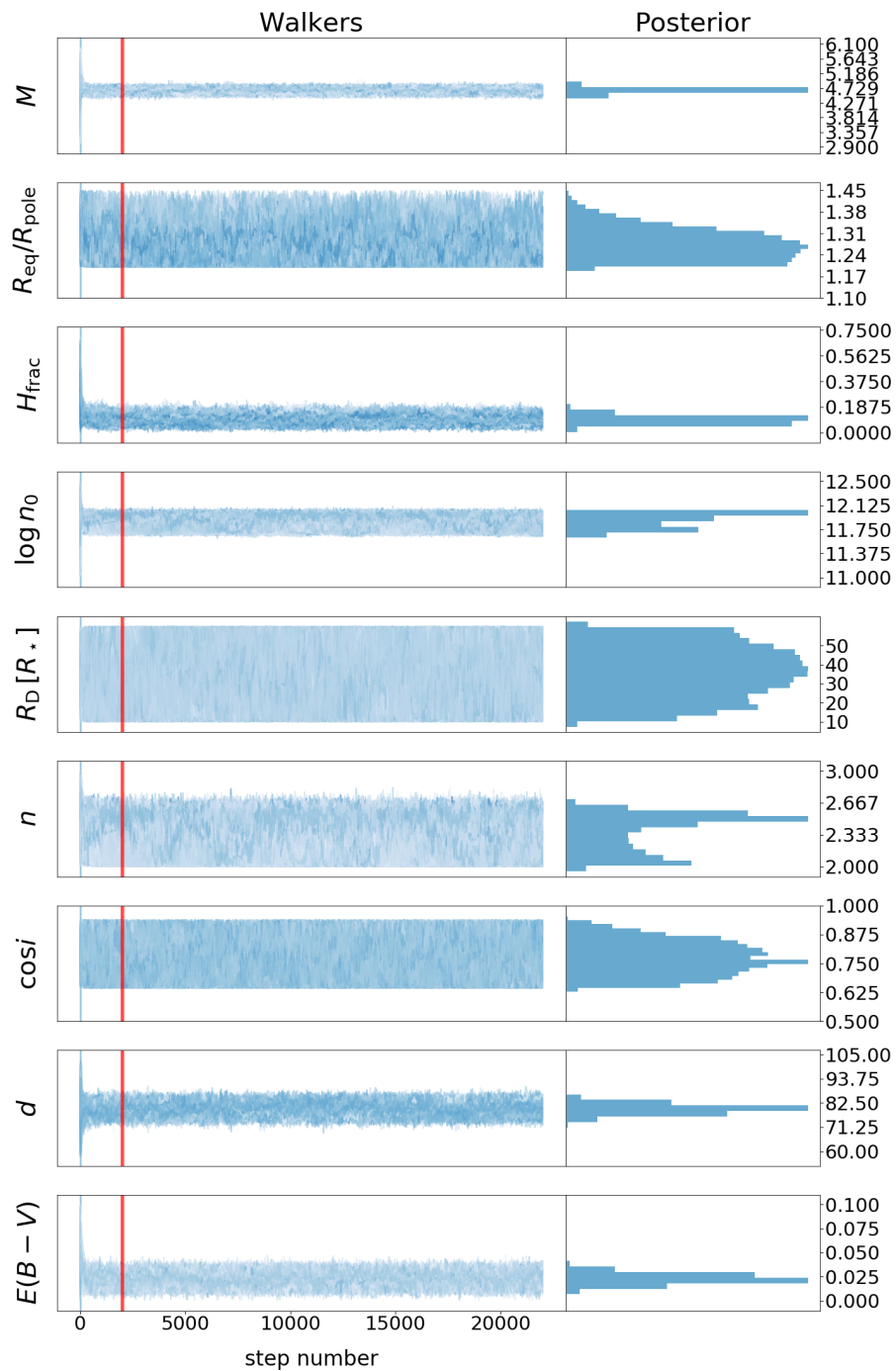


Figure B.4: Trace plot for the BEMCEE result in Fig. 4.4, the red line represents the burn-in phase.

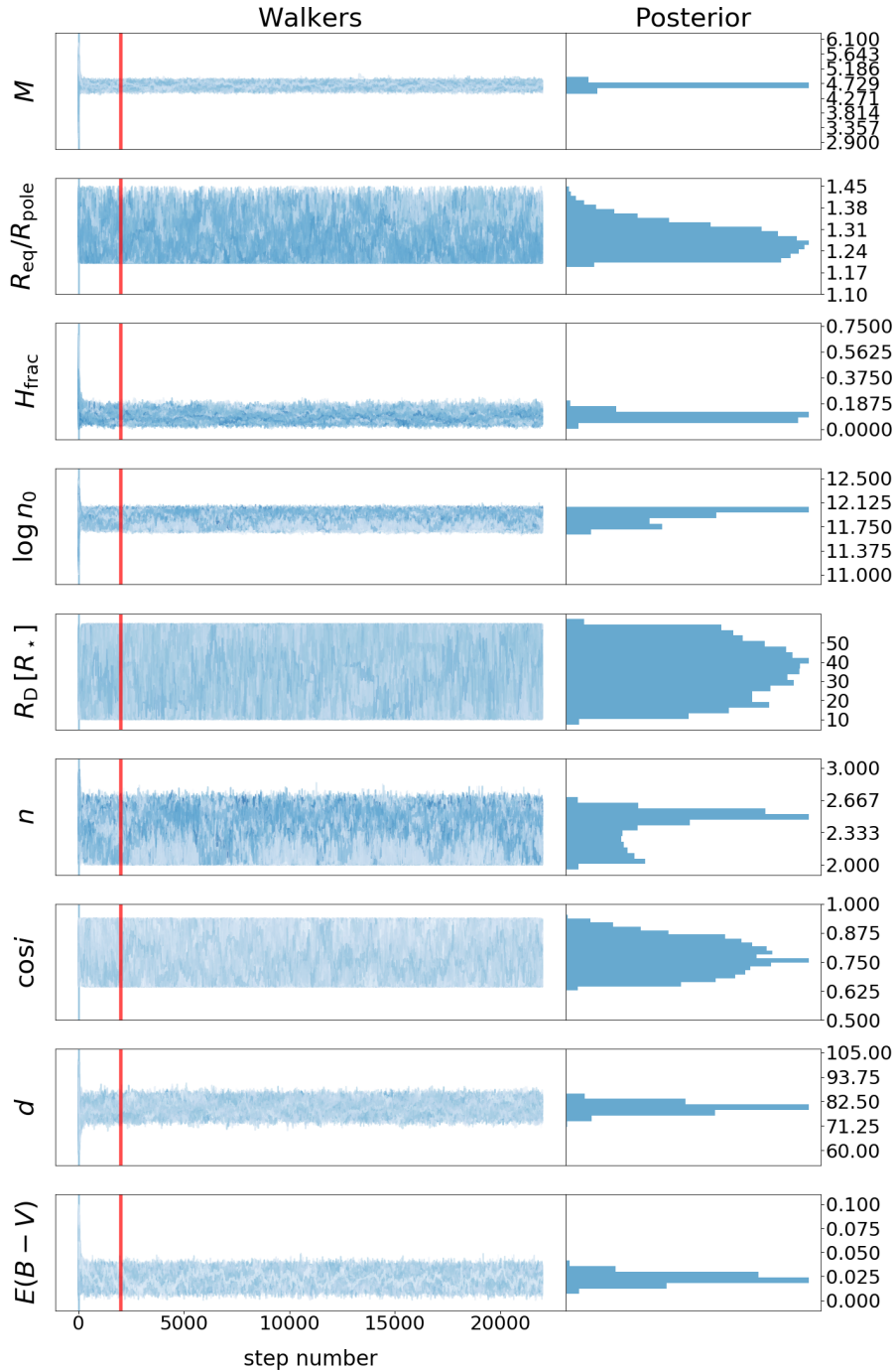


Figure B.5: Trace plot for the BEMCEE result in Fig. 4.5, the red line represents the burn-in phase.

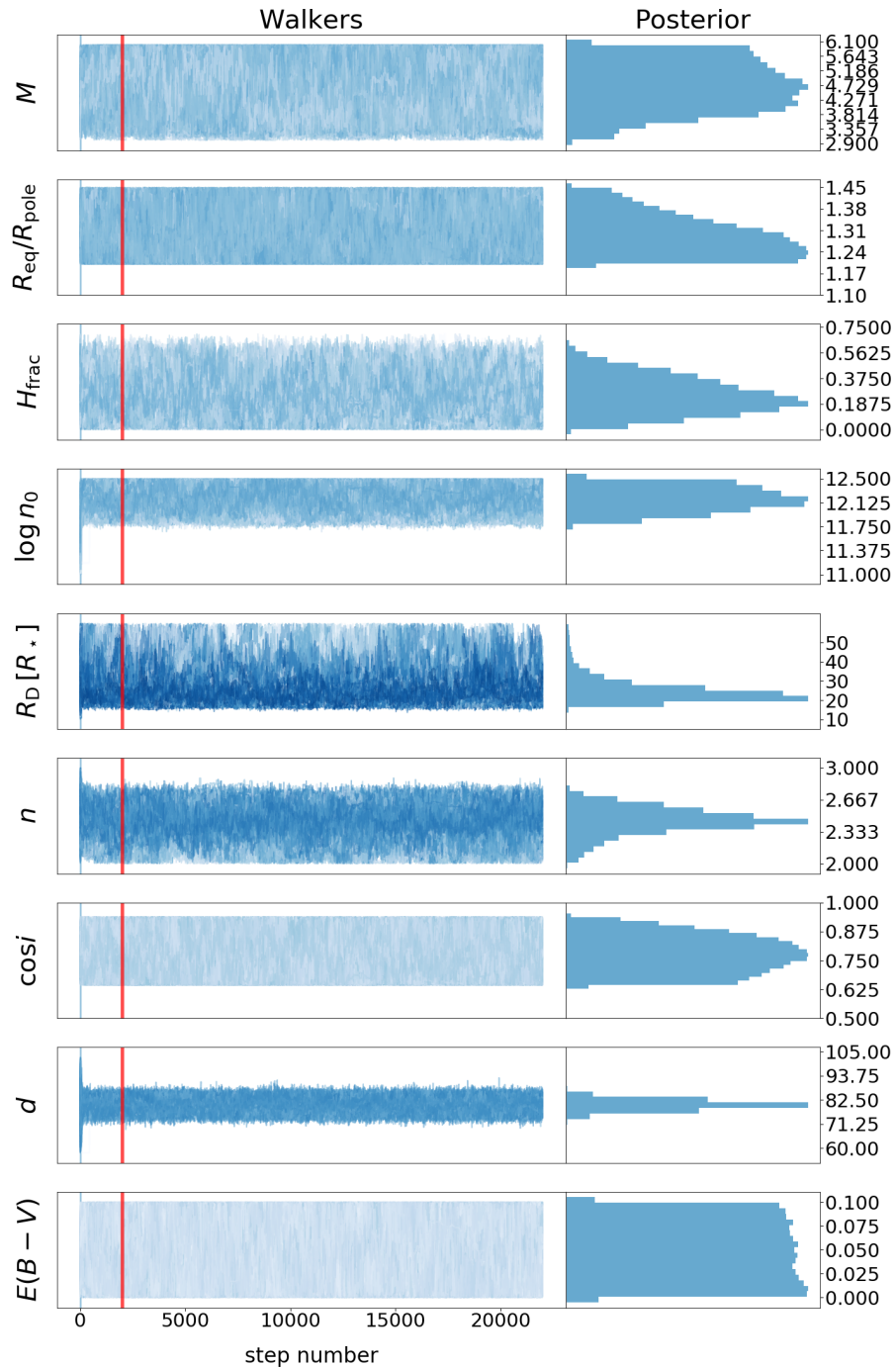


Figure B.6: Trace plot for the BEMCEE result in Fig. 4.7, the red line represents the burn-in phase.

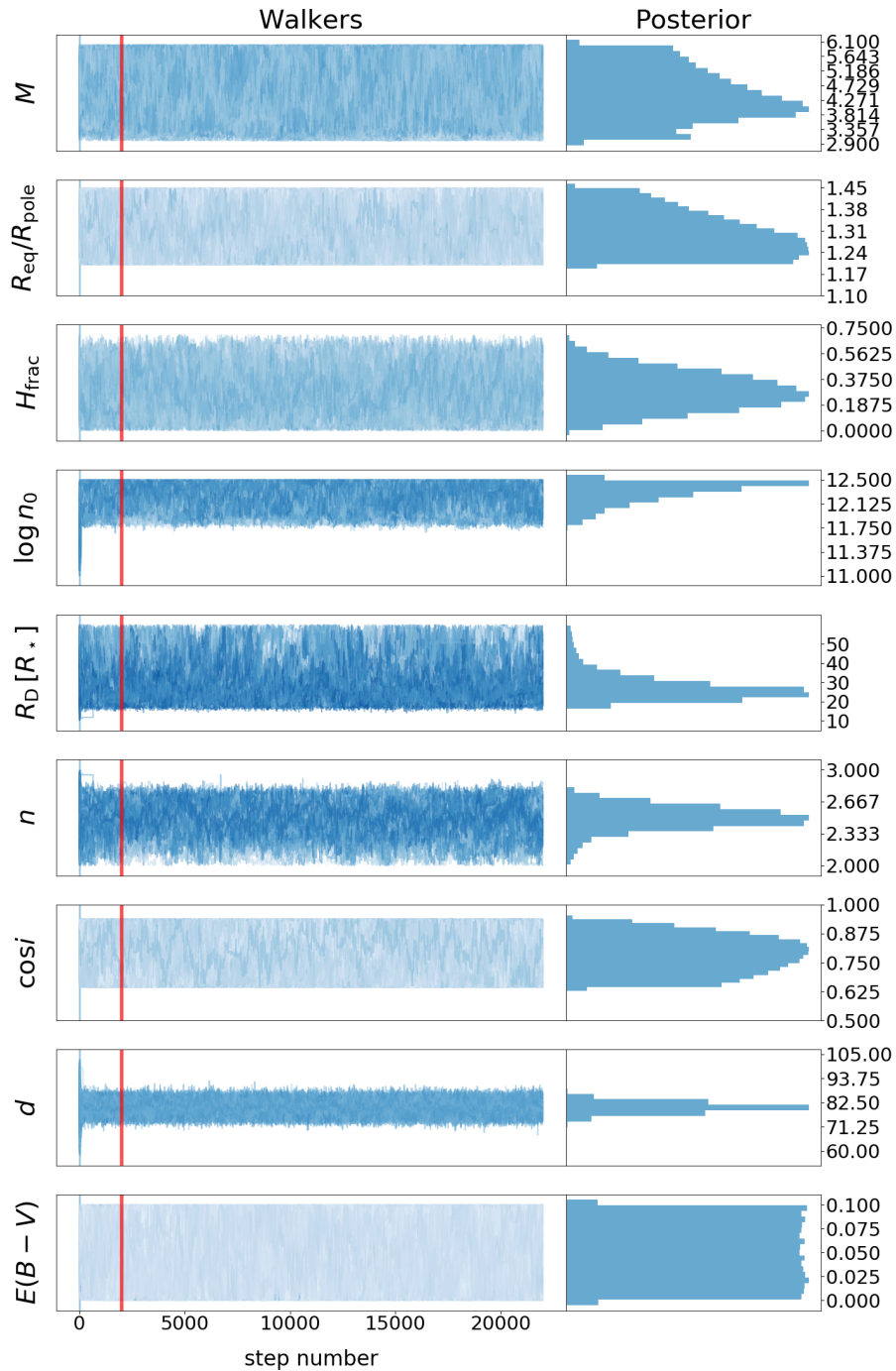


Figure B.7: Trace plot for the BEMCEE result in Fig. 4.8, the red line represents the burn-in phase.

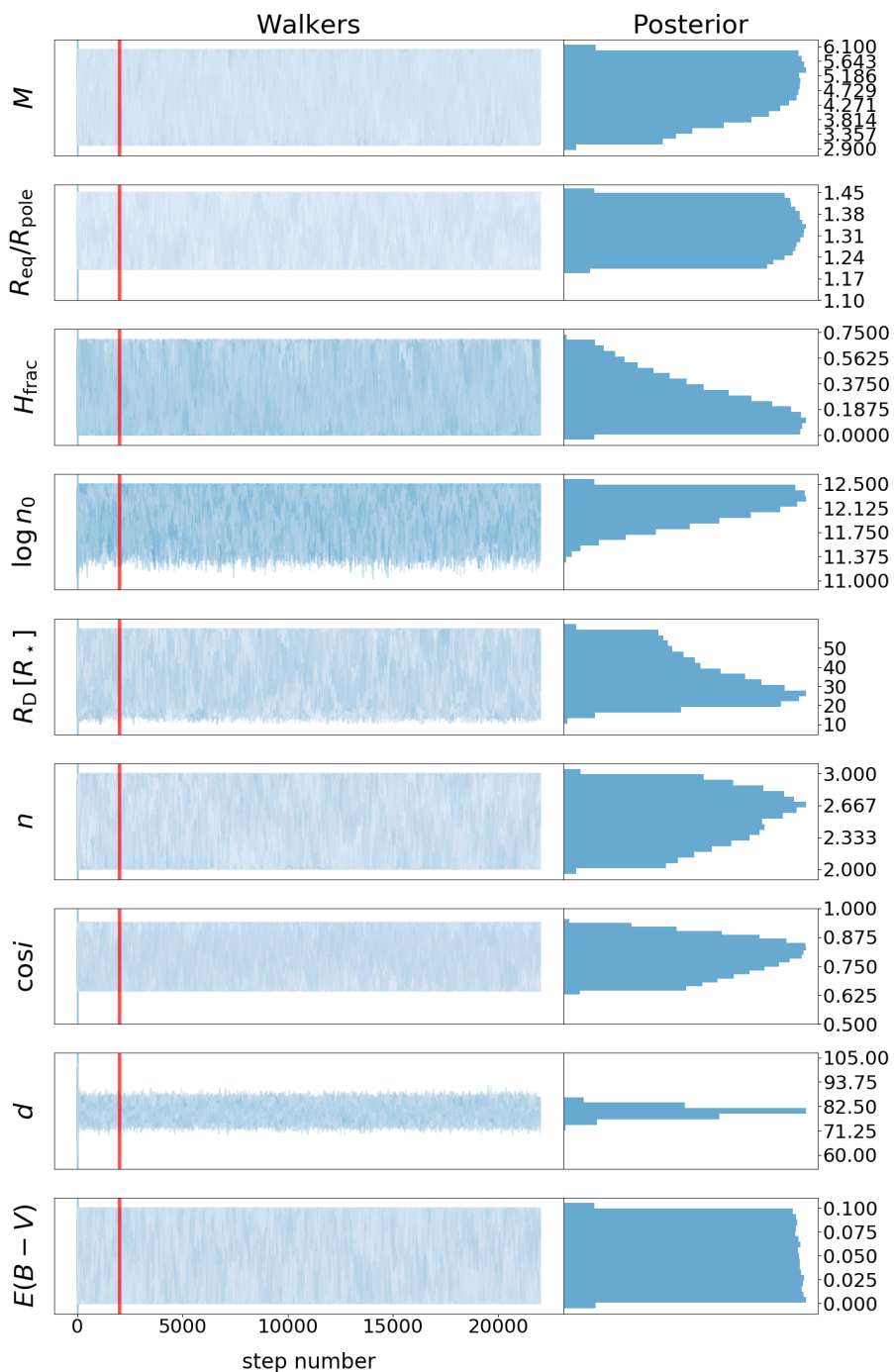


Figure B.8: Trace plot for the BEMCEE result in Fig. 4.9, the red line represents the burn-in phase.

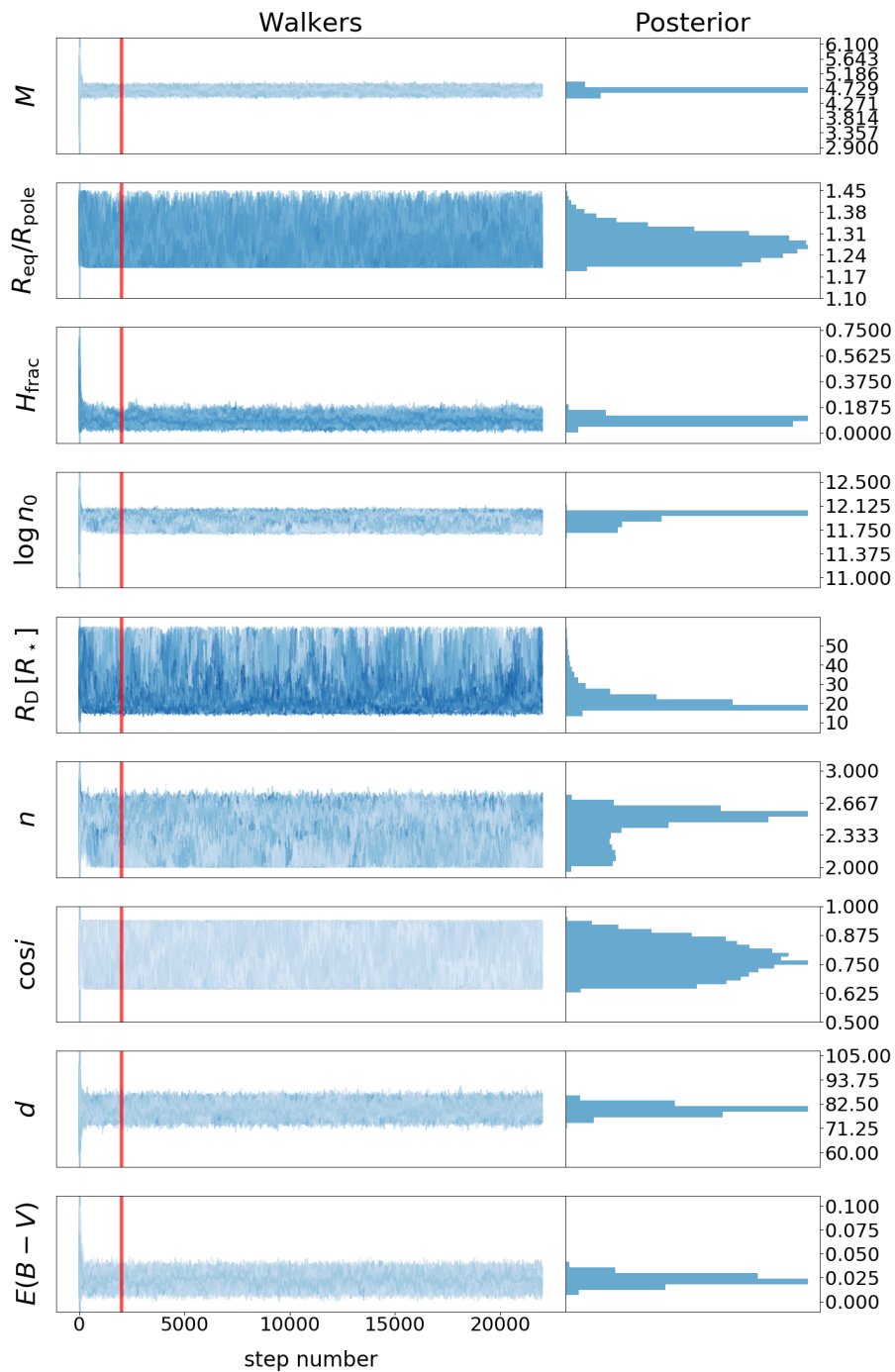


Figure B.9: Trace plot for the BEMCEE result in Fig. 4.10, the red line represents the burn-in phase.

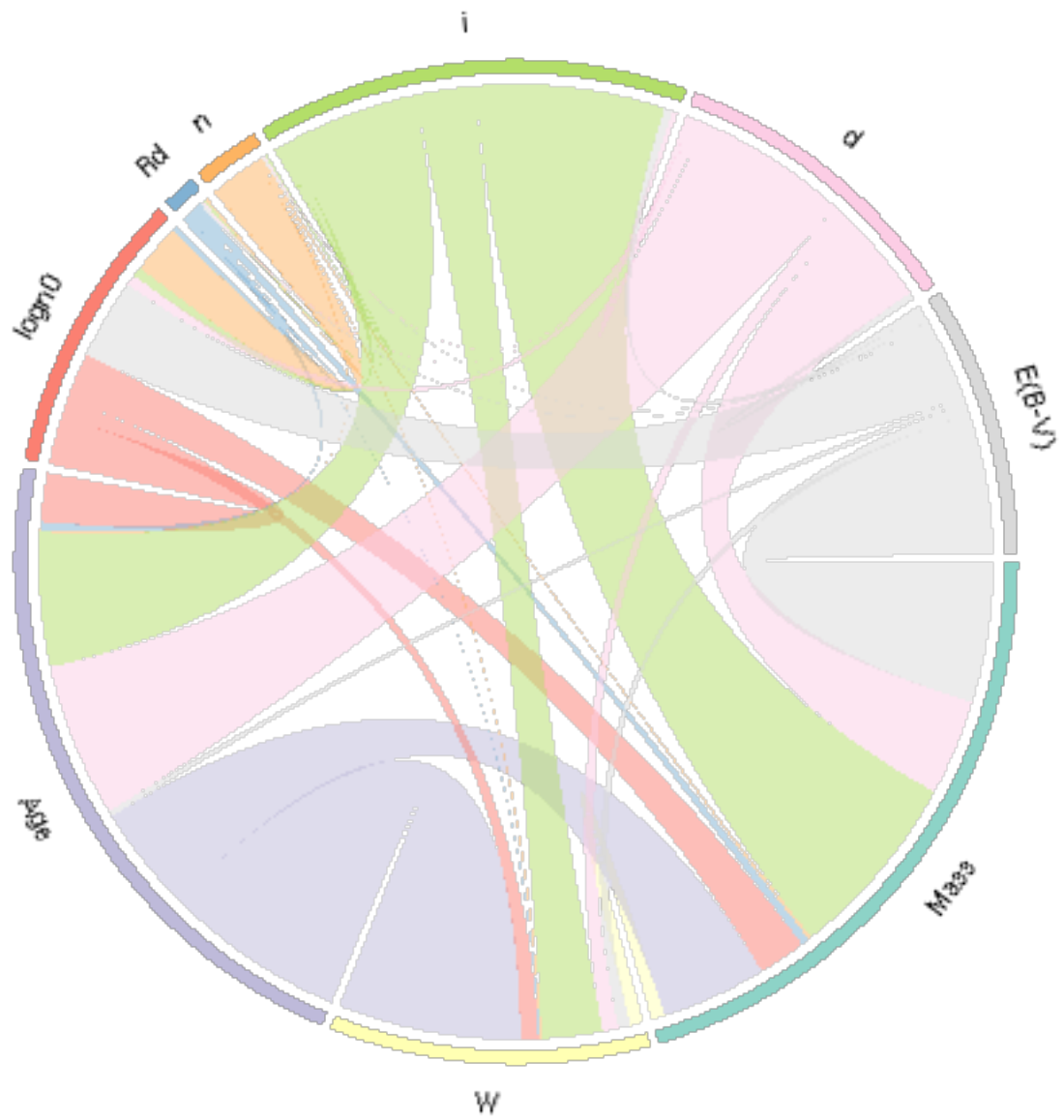


Figure B.10: Chord diagram for the correlations seen in Fig. 4.2

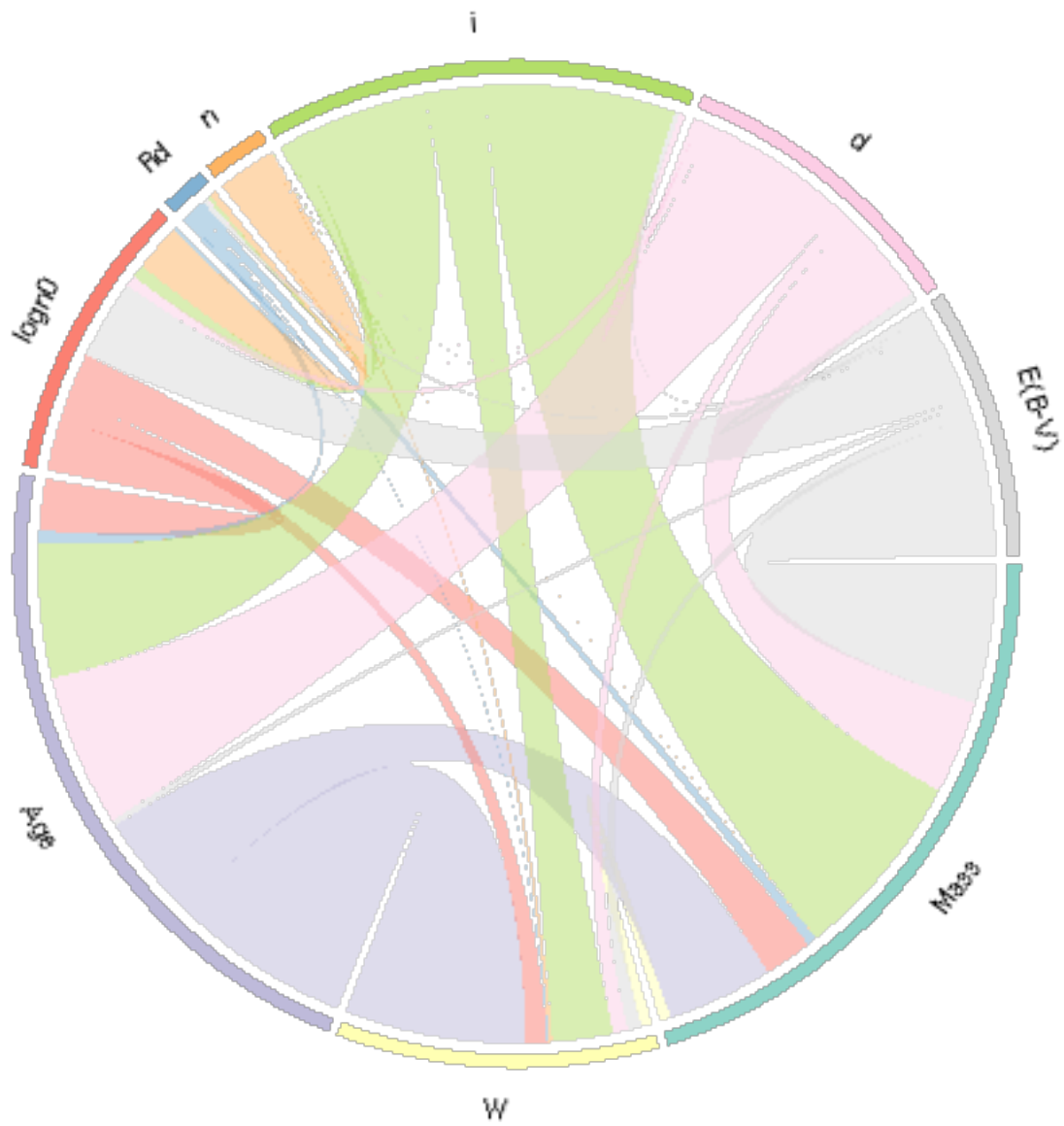


Figure B.11: Chord diagram for the correlations seen in Fig. 4.3

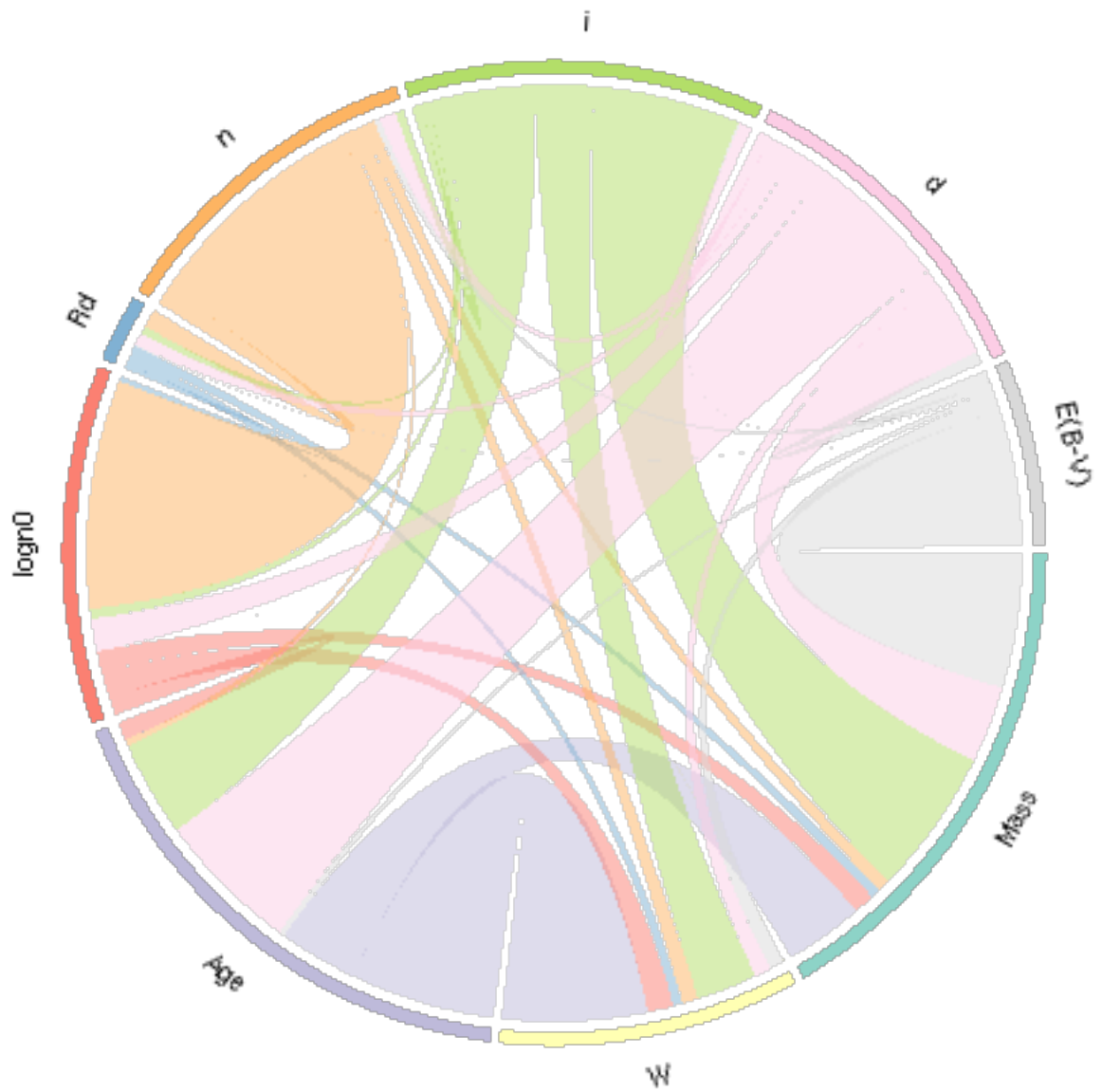


Figure B.12: Chord diagram for the correlations seen in Fig. 4.4

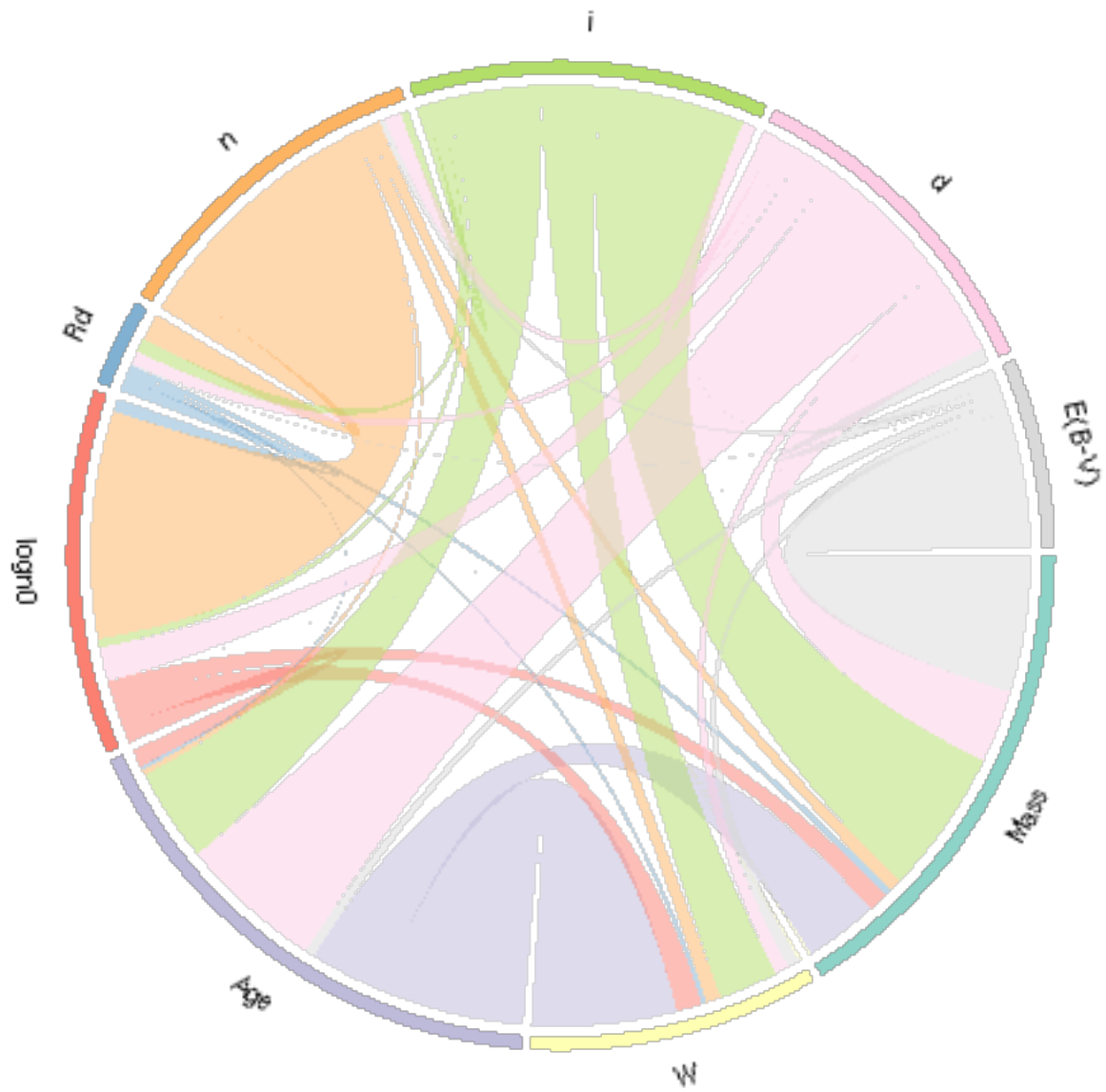


Figure B.13: Chord diagram for the correlations seen in Fig. 4.5

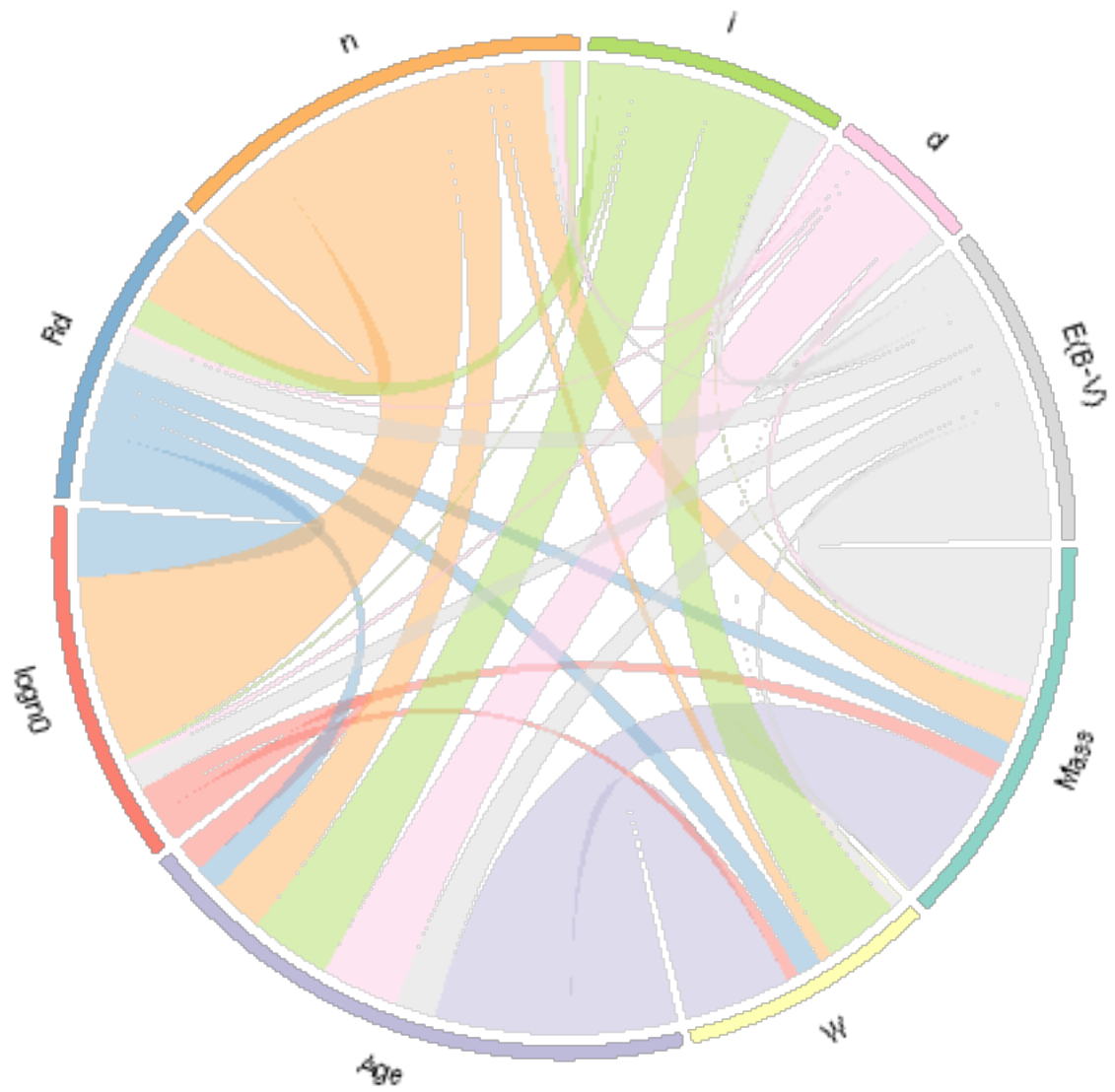


Figure B.14: Chord diagram for the correlations seen in Fig. 4.6

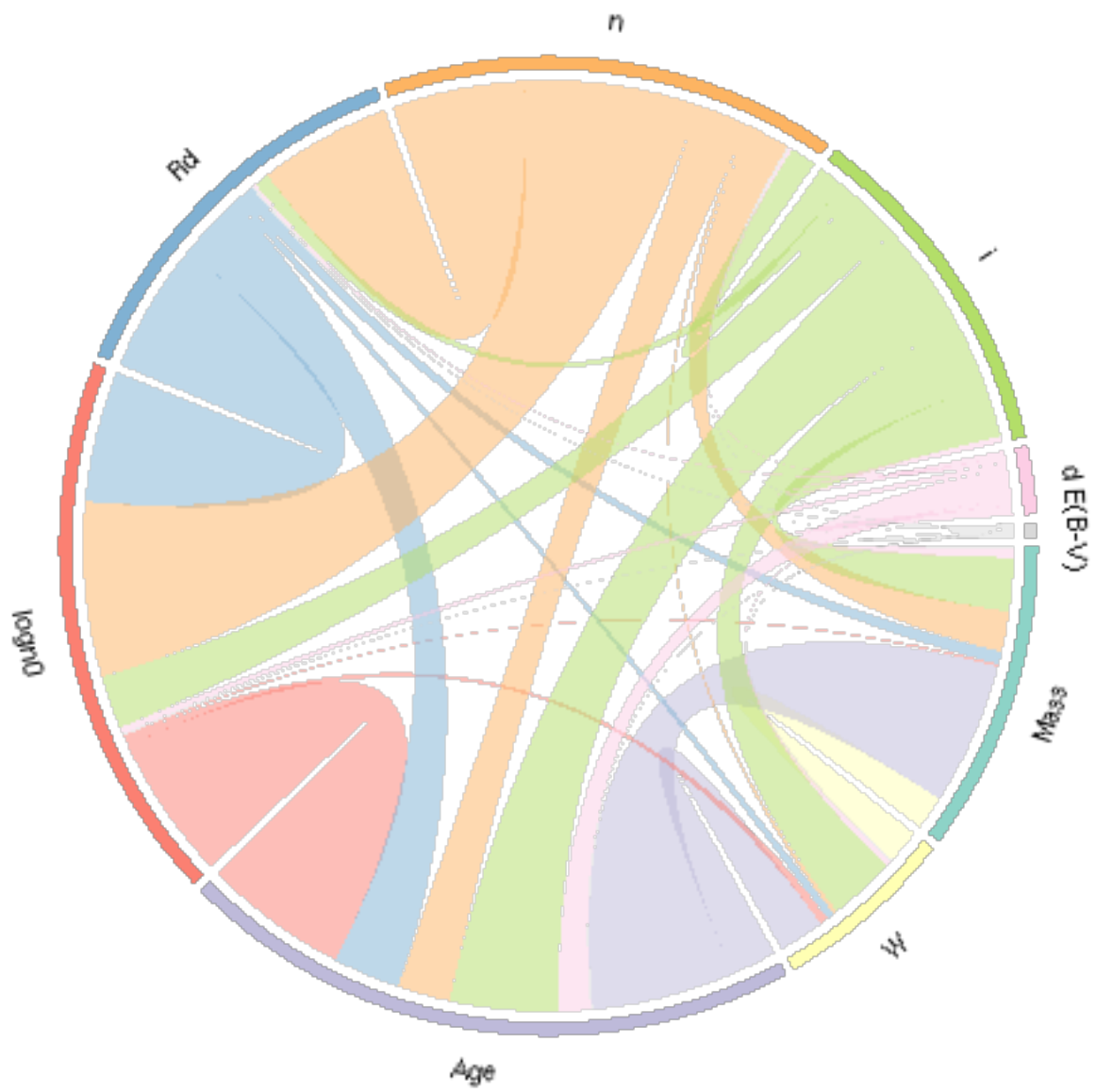


Figure B.15: Chord diagram for the correlations seen in Fig. 4.7

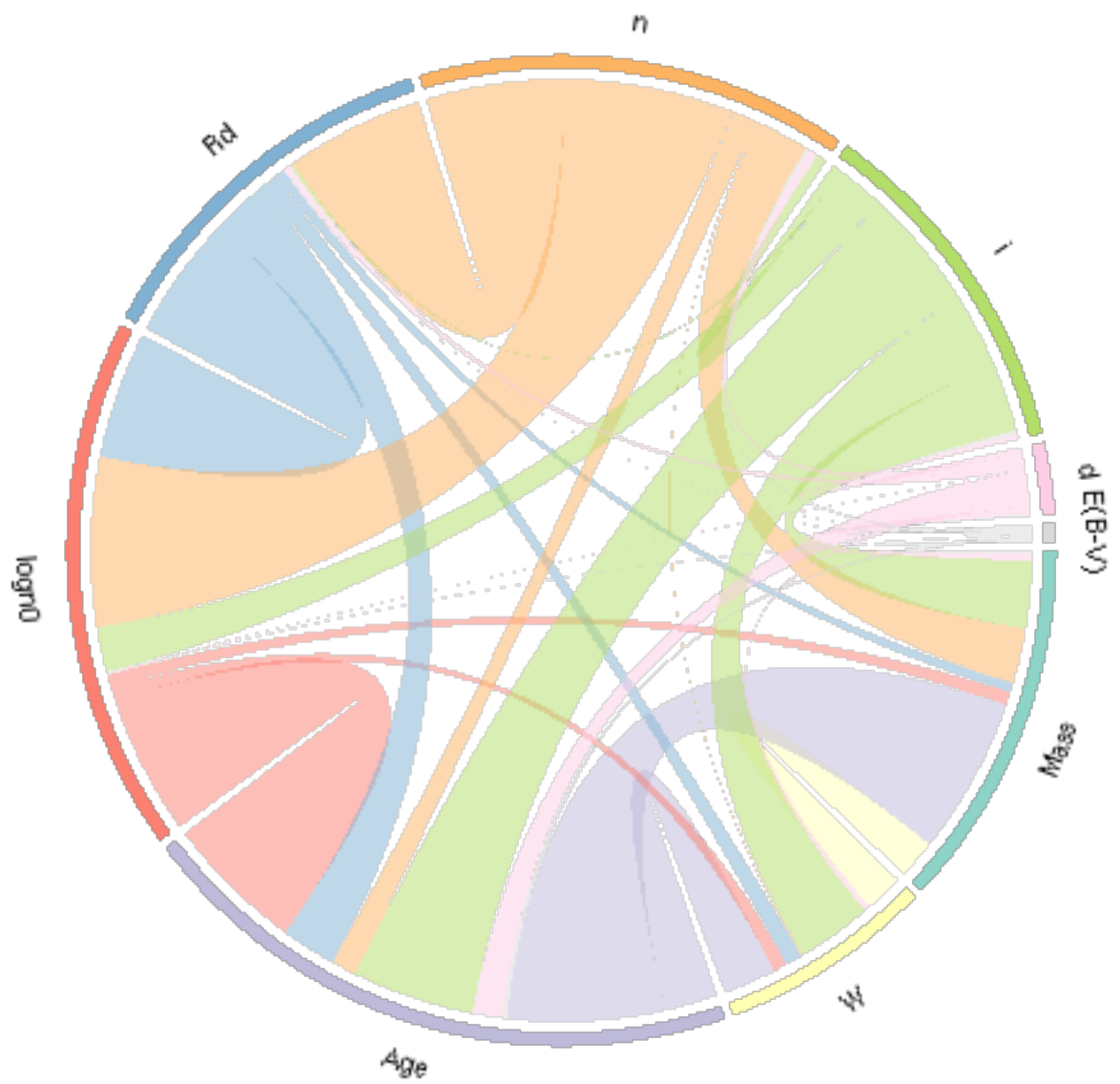


Figure B.16: Chord diagram for the correlations seen in Fig. 4.8

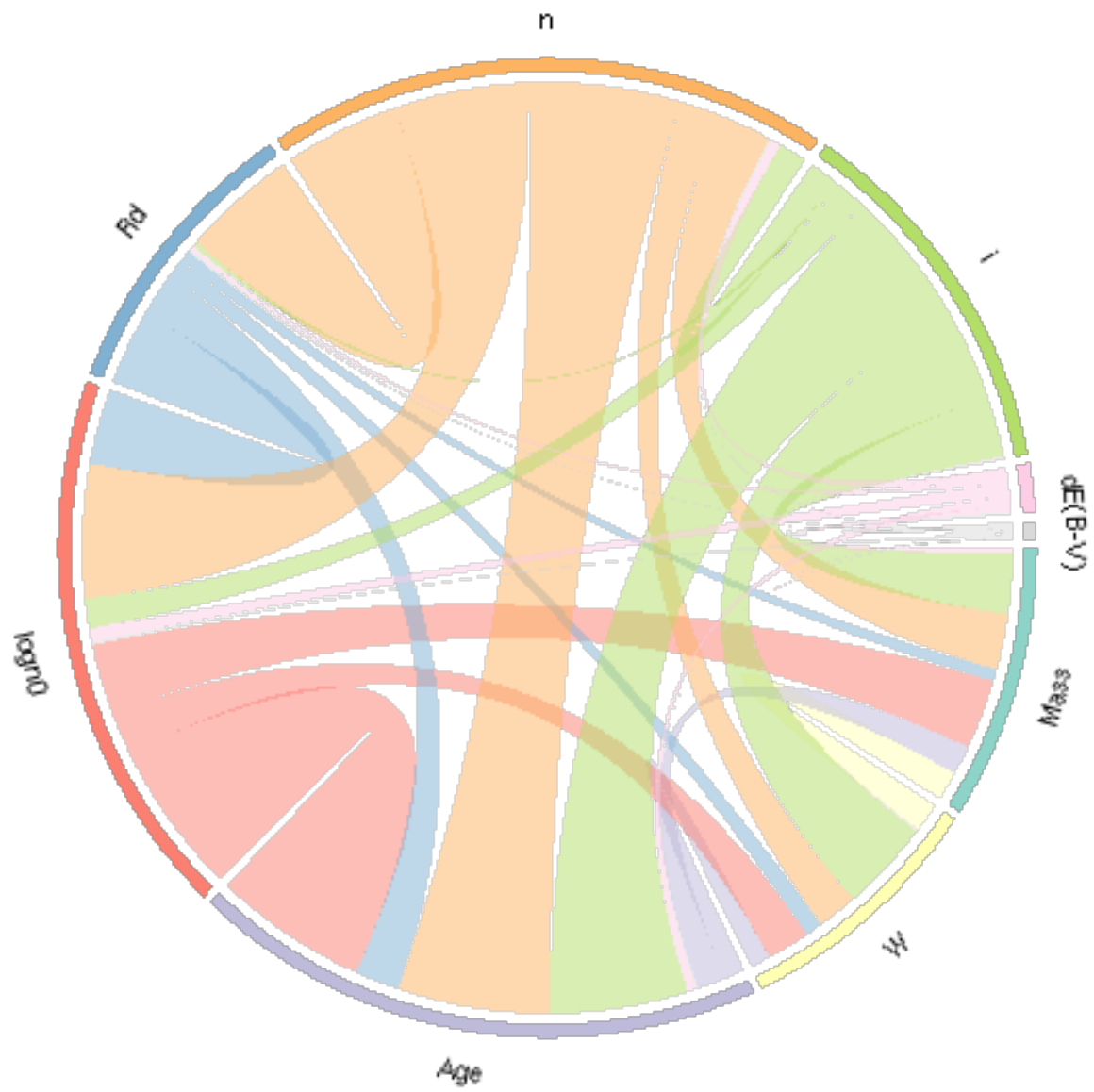


Figure B.17: Chord diagram for the correlations seen in Fig. 4.9